ISSN 1028-8546

Volume XVIII, Number 4
Section: En
December, 2012

Azerbaijan Journal of Physics

Fizika

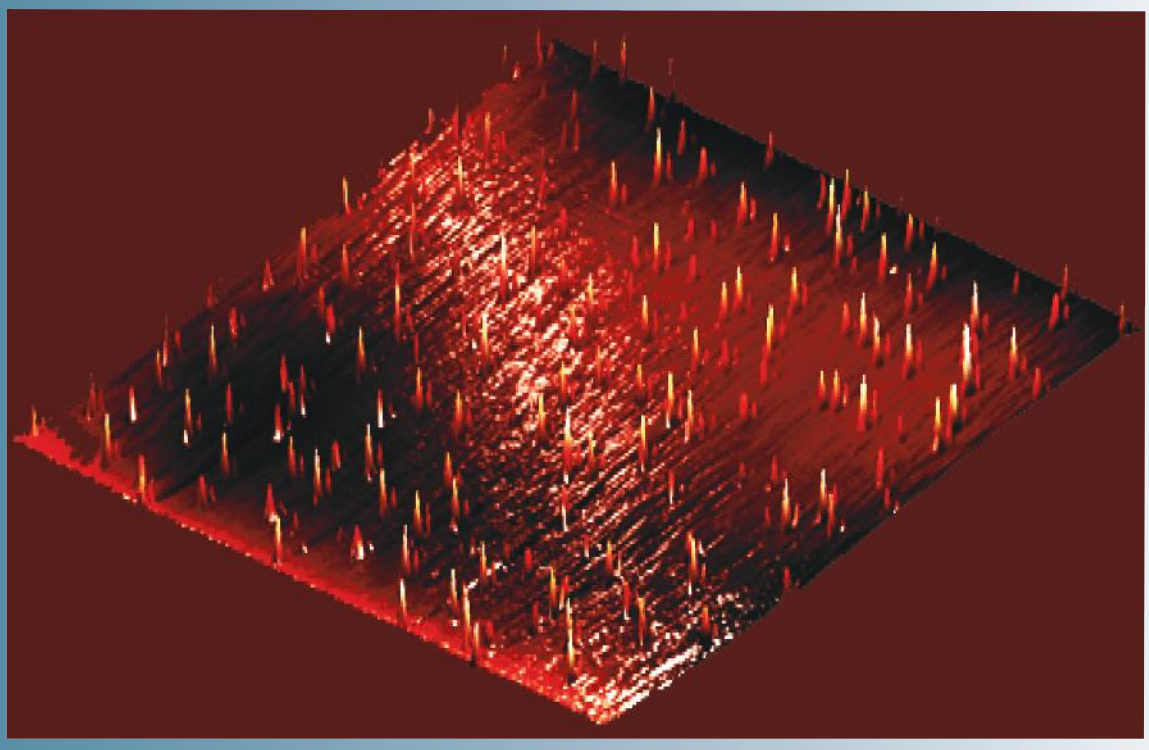

www.physics.gov.az

G.M. Abdullayev Institute of Physics
Azerbaijan National Academy of Sciences
Department of Physical, Mathematical and Technical Sciences

Published from 1995

ISSN 1028-8546
vol. XVIII, Number 4, 2012
Section: En

Azerbaijan Journal of Physics

Fizika

G.M.Abdullayev Institute of Physics
Azerbaijan National Academy of Sciences
Department of Physical, Mathematical and Technical Sciences

HONORARY EDITORS

Arif PASHAYEV **Mahmud KERIMOV**

EDITORS-IN-CHIEF

Arif HASHIMOV
Chingiz QAJAR

SENIOR EDITOR

Talat MEHDIYEV

INTERNATIONAL REVIEW BOARD

Ivan Scherbakov, Russia
Kerim Allahverdiyev, Turkey
Mehmet Öndr Yetiş, Turkey
Gennadii Jablonskii, Buelorussia
Rafael Imamov, Russia
Vladimir Man'ko, Russia
Eldar Salayev, Azerbaijan
Dieter Hochheimer, USA
Victor L'vov, Israel
Vyacheslav Tuzlukov, South Korea
Majid Ebrahim-Zadeh, Spain
Firudin Hashimzadeh, Azerbaijan
Anatoly Boreysho, Russia
Mikhail Khalin, Russia
Hasan Bidadi, Tebriz, East Azerbaijan, Iran
Natiq Atakishiyev, Mexico
Maksud Aliyev, Azerbaijan
Bahram Askerov, Azerbaijan
Vali Huseynov, Azerbaijan
Javad Abdinov, Azerbaijan
Bagadur Tagiyev, Azerbaijan
Tayar Djafarov, Azerbaijan
Talat Mehdiyev, Azerbaijan
Nazim Mamedov, Azerbaijan
Emil Guseynov, Azerbaijan
Ayaz Bayramov, Azerbaijan
Tofiq Mammadov, Azerbaijan
Salima Mehdiyeva, Azerbaijan
Shakir Naqiyev, Azerbaijan
Rauf Guseynov, Azerbaijan
Almuk Abbasov, Azerbaijan
Yusif Asadov, Azerbaijan

TECHNICAL EDITORIAL BOARD

senior secretary Elmira Akhundova, Nazli Huseynova, Sakina Aliyeva, Nigar Akhundova, Elshana Aleskerova

PUBLISHING OFFICE

33 H.Javid ave, AZ-1143, Baku
ANAS, G.M.Abdullayev Institute of Physics

Tel.: (99412) 439-51-63, 439-32-23
Fax: (99412) 447-04-56
E-mail: jophphysics@gmail.com
Internet: www.physics.gov.az/index1.html

It is authorized for printing: 30.12.2012

Published at: **"ŞƏRQ-QƏRB "**
17 Ashug Alesger str., Baku
Typographer :Aziz Gulaliyev

Sent for printing on: __ .2012
Printing approved on: __ .2012
Physical binding:_____
Number of copies:_____200
Order:_____

EFFECTS OF RANDOMNESS ON THE CRITICAL TEMPERATURE IN QUASI-TWO-DIMENSIONAL ORGANIC SUPERCONDUCTORS

E. NAKHMEDOV[1,2], O. ALEKPEROV[2] AND S. MAMMADOVA[2]

Institut für Theoretische Physik, Universität Würzburg, Am Hubland, D-97074 Würzburg, Germany

[2] Institute of Physics, Azerbaijan National Academy of Sciences, H. Cavid ave. 33, AZ1143 Baku, Azerbaijan

(Dated: November 8, 2012)

Effects of non-magnetic disorder on the critical temperature T_c of organic weak-linked layered superconductors with singlet in-plane pairing are considered. The randomness in the interlayer Josephson coupling is shown to destroy phase coherence between the layers and T_c suppresses smoothly in a large extent of the disorder strength. Nevertheless the disorder of arbitrary high strength can not destroy completely the superconducting phase. The obtained quasi-linear decrease of the critical temperature with increasing the disorder strength is in good agreement with experimental measurements.

Keywords: organic semiconductors, effects of non-magnetic disorder
PACS: 74.78.-w, 74.62.-c, 74.70.Kn, 74.50.+r

Organic molecular crystals $\kappa-(BEDT-TTF)_2X$ [abbreviated as $\kappa-(ET)_2X$] are in the center of attention due to their unusual normal metallic and superconducting properties [1]. The flat ET molecules in $\kappa-(ET)_2X$ organic metals dimerize to form molecular units that stack in planes on a triangular lattice [2]. The anions X, which modify from $X = Cu[N(CN)_2]Cl$ through $X = Cu[N(CN)_2]Br$ to $X = Cu(NCS)_2$, separate the planes and accept one electron from each $BEDT-TTF$ dimer. Most of the ET-based superconductors (SCs) are strongly anisotropic quasi-two-dimensional (quasi-2D) conductors because the conductivity is approximately isotropic within the layers of the ET donor molecules but smaller by a factor of$\sim 10^3$ in the perpendicular direction. Measurements of the superconducting coherence lengths [3] within-$\xi_{\|}$ and perpendicular $\xi_{\perp}$ to the superconducting planes in e.g. $\kappa-(ET)_2Cu[N(CN)_2]Br$ yield $\xi_{//} \approx 37$˚4A and $\xi_{\perp} \approx 4$A˚, the latter of which is much smaller than the interlayer distance $\sim$ 15Å.This fact suggests that superconductivity in the direction perpendicular to the plane may involve Josephson tunneling.

Low temperature properties of organic SCs are known to be very sensitive to disorder [4]. .Alloying with anions, *x*-ray irradiation, or cooling rate controlled anion reorientation introduces non-magnetic randomness into the system, however leaving unchanged, to a large extent, in-plane molecular structures. Recently, effects of non-magnetic disorder on superconductivity in organic $\kappa-(ET)_2Cu(SCN)_2$ have been studied experimentally in Refs [5,6]. The non-magnetic disorder was introduced in these experiments via irradiation by either *x*-rays or photons [5,6] and via partial substitution of $BEDT-TTF$ molecules with deuterated $BEDT-TTF$ or $BMDT-TTF$ molecules [6]. All disorder seems to affect the terminal ethylene group and anion bound structures. The measurements for samples with molecular substitutions show [6] that the mean free path l is longer than the in-plane coherent length $\xi_{\|}$, indicating that the superconducting planes can be considered to be in clean limit. *Tc* was found [5] to fall quasi-linearly with defect density, and the dependence exhibits a sharp change in slope from 0.31 to 0.15 around a threshold value of the interlayer residual resistivity $\rho_o^* \approx 2\Omega$cm. The main feature of the experiments is that the samples exhibit a superconducting ground state even at the highest defect densities, and there is not a SC-normal metal phase transition in difference from quasi-1D organic SC_s [7] where the randomness transforms the system into a normal metallic state. In the light of the experimental data, the Abrikosov-Gor'kov's theory [8] for non-magnetic defects in non-s-wave *SCs* seems to fail to explain the experimental data.

We study, in this article, effects of randomness in the Josephson coupling energy on the critical temperature of weak-linked quasi-2D *SCs*. Therefore, an influence of a possible in-plane molecular disorder on the superconducting properties of the system is ignored. Suppression of superconductivity in the presence of non-magnetic impurities can in general be realized by destroying either the modulus or the phase coherence of the order parameter [9, 10]. Although strong fluctuations of the order parameter phase destroy off-diagonal long-range order (ODLRO) in an isolated superconducting plane [11], the point-like topological defects of a "phase field" such as "vortex" and "antivortex" of Kosterlitz and Thouless [12] sets up a quasi-long range order in the system.

The strongly anisotropic organic SCs with in-plane singlet pairings are modeled as the regularly placed superconducting layers with Josephson-coupling between nearest-neighboring layers with classical free energy functional

$$F_{st}\{\varphi\} = N_s^{(2)}(T)\sum_j \int d^2r \left\{\frac{\hbar^2}{8m_{\|}}\left[\left(\frac{\partial\varphi_j}{\partial x}\right)^2 + \left(\frac{\partial\varphi j}{\partial y}\right)^2\right] + \sum_{g=\pm1} E_{jj+g}\left[1-\cos\left(\varphi_{j-}\varphi_{j+g}\right)\right]\right\}, \quad (1)$$

where $\varphi_j(\boldsymbol{r})$ denotes the phase of the order parameter $\Delta_j(r)=[\Delta_j]$ exp $(i\varphi_{j(\boldsymbol{r})})$, and $N_s^{(2)}$ (T) is the surface density of superconducting electrons; $N_s^{(2)}(T)= N_N^{(2)}(0)= N_N^{(2)}=\frac{P_F^2}{2_{\pi}\hbar^2}$ at $T \geq T_s^{(2)}$,and $N_s^{(2)}(T) = N_N^{(2)}(0)$ τ(T) with

$\tau(T)=\frac{T_c^{(2)}-T}{T_c^{(2)}}$ at $T\leq T_c^{(2)}$.The last term in Eq.(1) describes the Josephson coupling with the energy E_{jj+g}.

Fluctuations of the order parameter modulus can be neglected for pure *SCs* far from $T_c^{(2)}$, the mean-field critical temperature calculated for an isolated. Therefore, the contributions to $F_{st}\{\varphi\}$ in Eq. (1), coming from the modulus of the order parameter $|\Delta_j|$, are omitted.

We assume the Josephson energy $E_{j,j+g}$ to be a random parameter with Gaussian distribution, centered at the mean value E_g given by

$$P\{E_{j,j+g}\} = (2\pi W^2)^{-1/2}\exp\{-(E_{j,j+g}-E_g)^2/(2W^2)\} \quad (2)$$

W^2 *i*s taken as a measure of disorder strength.

Employing the replica trick one can calculate the average value of the order parameter *cos(φj(z))*

$$\langle\langle cos(\varphi_j(\boldsymbol{r}))\rangle\rangle_{dis} = -T\frac{\delta}{\delta\eta_j(\boldsymbol{r})}\langle InZ\rangle|_{nj(z)=0} =$$
$$-T\frac{\delta}{\delta\eta_{j(\boldsymbol{r})}}\lim_{n\to 0}\frac{\partial(Z^n)}{\partial_n}\Big|\eta_{j=0} \quad (3)$$

where $Z = \int D_\varphi\ exp\ \left(-\frac{1}{T}F_{st}\{\varphi,\eta\}\right)$ is the partition function with respect to the free energy functional $F_{st}\{\varphi,\eta\}$ which contains in addition to Eq.(1), the generating field term $\Sigma_j\eta_j\cos(\varphi_j(r))$. The double bracket, $\langle\langle\ldots\rangle\rangle_{dis}$ is a shorthand notation for the double average over thermodynamic fluctuations and over disorder.

Integration out the Gaussian random variables yields

$$\langle\langle cos\left(\varphi_j(\boldsymbol{r})\right)\rangle\rangle = \int\frac{d\zeta_{,j,g}}{\sqrt{2\pi}}e^{-\frac{c_{j,g}^2}{2}}\frac{D\varphi cos(\varphi_j)e^{-F/T}}{\int D_{\varphi e^{-F/T}}} \quad (4)$$

with

$$F=N_s^{(2)}\Sigma\int d^2r\left\{\frac{h^2}{8m_{//}}\left[\left(\frac{\partial\varphi_j}{\partial x}\right)^2+\left(\frac{\partial\varphi_j}{\partial y}\right)^2\right]+\Sigma\big(E_g - W\zeta_{j,g}\big)\left[1-cos\left(\varphi_j(\boldsymbol{r})-\varphi_{j+g}(\boldsymbol{r})\right)\right]\right\} \quad (5)$$

where $\zeta_{j,g}(r)$ denotes a Hubbard-Stratonovich auxiliary decoupling field. In order to clarify a character of the saddle-point for the variable $\zeta_{j,g}(r)$, one writes the expression(4) for $\langle\langle cos\left[\varphi_j(\boldsymbol{r})-\varphi_{j+g}(\boldsymbol{r})\right]\rangle\rangle_{dis}$ and find the saddle-point ζ_{j_0,g_0} as

$$\zeta_{j_0,g_0} = \frac{WN_s^{(2)}}{T}\cdot\frac{\langle cos[\varphi_{jo}-\varphi_{jo+go}]\rangle^2-(cos^2[\varphi_{jo}-\varphi_{jo+go}])}{\langle\cos[\varphi_{jo}-\varphi_{jo+go}]\rangle} \quad (6)$$

The expression for the effective free-energy functional at the saddle-point ζ_{j_0,g_0}, given by Eq. (6), becomes similar to that for a regular quasi-2D SC with renormalized inter-layer Josephson energy,

$$E_g \to E_g - \frac{W^2N_s^{(2)}}{T}\frac{\langle\cos[\varphi_{jo+go}]\rangle^2-\langle\cos^2[\varphi_{jo}-\varphi_{jo+go}]\rangle}{\langle\cos[\varphi_{jo}-\varphi_{jo+go}]\rangle}$$

Equation for T_c in quasi-2DSCsis derived from Eq.(4) by using the self-consistent mean-field method [13], which consists in replacing the cosine term of Eq. (5) as

$$\sum_g E_g\ cos(\varphi_j-\varphi_{j+g}) \to \eta E_\perp\langle\langle cos(\varphi)\rangle\rangle_c\cos\varphi(z) \quad (7)$$

where η is the coordination number, and $E_\perp \approx t_\perp^2/\epsilon_F$ with $t_\perp$ and ϵ_F being the interlayer tunneling integral and the Fermi energy. The phase correlations on the nearest-neighboring layers in this approximation is simplified by describing it as a motion of phason in the average field of phases with most probable value, which coincides with the average value for a clean system $\langle\langle\cos(\varphi)\rangle\rangle_c \equiv \langle\langle cos(\phi)\rangle\rangle_{dis}$ [13] . For dirty system the most probable value strongly differs from the average value. Indeed, we assume that a distribution function of the order parameter in the presence of randomness is broad and asymmetric. This broadness and asymmetry becomes stronger around the critical temperature due to huge thermal fluctuations. Therefore, the knowledge of the arithmetic average is insufficient, and infinitely many moments give a contribution to the distribution function of the order parameter at the tail. We identify $\langle\langle cos(\varphi)\rangle\rangle$c with the most probable or typical value of the order parameter. For the disordered SC we choose $\langle\langle\cos\varphi\rangle\rangle_c = \langle\langle\cos\varphi\rangle\rangle_{dis} - \frac{\langle\langle\cos\varphi\rangle^2\rangle_{dis}-\langle\langle\cos\varphi\rangle\rangle_{dis}^2}{\langle\langle\cos\varphi\rangle\rangle_{dis}}$ resembles a change made by the saddle-point (6) in the free-energy functional. The functional integral over the phases in Eq. (4) can not yet be evaluated, even after this simplification. Taking however advantage of the smallness of $E_\perp\langle\langle cos(\varphi)\rangle\rangle_c$ near T_c, an expansion of the integrand of Eq. (4) in this quantity allows to obtain the following equations for $\langle\langle cos(\varphi)\rangle\rangle_{dis}$ and $\langle\langle cos(\varphi)\rangle^2\rangle_{dis}$

$$\langle\langle cos(\varphi)\rangle\rangle_{dis} = \frac{\eta N_s^{(2)}E_\perp}{k_BT}\int d^2r\,\langle\cos\varphi(0)\cos\varphi\,(r)\rangle_0\,\langle\cos\varphi\rangle_c \quad (8)$$

$$\langle\langle\cos\varphi\rangle^2\rangle_{dis} = (1+W^2/E_\perp^2)\langle\langle\cos\varphi\rangle\rangle_{dis} \quad (9)$$

Final equation for T_c, obtained from the above written expressions, reads

$$1=\frac{\eta E_\perp N_s^{(2)}}{T_c}\left(1-\frac{W^2}{E_\perp^2}\right)\int\langle cos\left(\varphi\,(r)\right)\cos\big(\varphi(0)\big)\rangle_0\,dr \quad (10)$$

The phase-phase correlator in Eq. (10) is calculated in the clean limit of the *2D* free energy functional, obtained from Eq. (1)by setting $E_{j,j+g}=0$, which returns, [9,11]

$$\langle\cos[\varphi(r)-\varphi(0)]\rangle_o = \begin{cases}\left(\frac{\varepsilon_{//}}{r}\right)^{\frac{4k_BT}{\varepsilon_F\left(1-T/T_c^{(2)}\right)}}, & r>\xi_\parallel\\ exp\left[-\frac{k_BT}{2\varepsilon_F\left(1-T/T_c^{(2)}\right)}\left(\frac{r}{\xi_\parallel}\right)^2\right], & r<\xi_\parallel\end{cases} \quad (11)$$

Where $\xi_\parallel = \frac{h\gamma v_F}{\pi^2k_BT_c^{(2)}}$ with $\ln\gamma = c = 0.577$ is the in-plane coherence length. Real-space integration of the correlator (11) in Eq. (10) for the critical temperature imposes the following restriction on the critical temperature

$-\frac{4k_BT_c}{\varepsilon_F\left(1-T_c/T_c^{(2)}\right)}+2<0$ yielding $T_c > T^*$, where

$$\frac{1}{T^*}=\frac{1}{T_c^{(2)}}+k_{B/\varepsilon_F} \quad (12)$$

T^* may be identified to the Kosterlitz-Thouless transition temperature. The order parameter's phases correlation between nearest-neighbor layers disappears as T_c approaches T^*, and system reveals effectively 2D superconducting behavior at $T = T^*$. So, the critical temperature in quasi-2D *SC* varies in the interval of $T^*<T_c<T_c^{(2)}$. One can estimate T^* for $\kappa-(ET)_2Cu(SCN)_2$ SC with $T_c^{(2)}\approx 10.5K$ for which the Fermi velocity and the effective mass of electrons are measured [5,6] to be respectively $v_F \approx 4\times10^4 m/s$ and $m^* \approx 3\ m_0$, where m_0 is a free electron mass. These data yield $T^* \approx 8.8K$, which consists well with maximally dropped critical temperature with disorder in Refs. [5,6]. The randomness in the Josephson energy in the presence of the order parameter phase fluctuations destroys the transverse stiffness the system. Equations (10) and (11) yield

$$1=qt^2\left\{4\left(1-e^{-1/4t}\right)+1/(1-t)\right\}, \quad (13)$$

where t is a dimensionless T_c-shift, $0<t<1$, introduced by

$$t=(\varepsilon_F/2k_B)\left(1/T_c-1/T_c^{(2)}\right), \quad (14)$$

and q is a dimensionless parameter

$$q=\frac{4\eta\gamma^2}{\pi^4}\left(\frac{t_\perp}{k_BT_c^{(2)}}\right)^2\left(1-\frac{W^2}{E_\perp^2}\right)=q_0(1-x), \quad (15)$$

with $\ln\gamma = c = 0.577$. q decreases from its maximal value $q=q_0=\frac{4\eta\gamma^2}{\pi^4}\left(\frac{t_\perp}{k_BT_c^{(2)}}\right)$ to zero as the disorder parameter $x = W^2/E_\perp^2$ increases from zero up to the maximal value $x = 1$ for strong randomness $W \sim E_\perp$. The numeric solution of Eqs. (13) and (14) for the dependence of T_c on x is depicted in Fig. 1.

Equation (13) is solved in two asymptotic limits. For $0 < t < 1/4$, which corresponds to a weak disorder limit when T_c varies around $T_c^{(2)}$, the exponential term is neglected, yielding

$$\frac{1}{T_c}=\frac{1}{T^*}-\frac{40\eta\gamma^2E_\perp}{\pi^4k_B\left(T_c^{(2)}\right)^2}\left(1-\frac{W^2}{E_\perp^2}\right) \quad (16)$$

In the limit $1/4 < t < 1$, which corresponds to relatively strong disorder limit when T_c varies around T^*, the exponential term in Eq. (13) is expanded yielding

$$\frac{1}{T_c}=\frac{1}{T_c^{(2)}}+\frac{2k_B}{\epsilon_F(1+q)}\approx\frac{1}{T^*}-\frac{8\eta\gamma^2E_\perp}{\pi^4k_B\left(T_c^{(2)}\right)^2}\left(1=\frac{W^2}{E_\perp^2}\right) \quad (17)$$

The results, obtained above for the classical fluctuations are valid for weak randomness, when T_c and $E_\perp$ have relatively high values. Quantum fluctuations have to be taken into account for strong disorder (small T_c and $E_\perp$) limit.

Effects of randomness in the presence of quantum phase fluctuations can be studied by starting from Hamiltonian of weak-linked metallic layers with in-layer attractive electron-electron interactions. Integration out the electronic degrees of freedom in the partition function, by following Ambegaokar et.al.[14] method, yields the following expression for the dynamical free energy functional

$$F_{qu}\{\varphi\}=\frac{h}{8V}\sum_{i,j}\iint dr dr'\ d_T K_{i,j}\varphi_i(r,T)\varphi_i(r',T)+ +Fstqu\varphi \quad (18)$$

where the phases depend now on the imaginary "time" T too, the dot on the phase means a "time"- derivative, $K_{i,j}$ is the susceptibility [9,14]. $F_{st}^{qu}\{\varphi\}$ is the stationary part of the dynamical free energy functional, which differs from the classical functional (1) by additional intergration over the imaginary "time" τ .

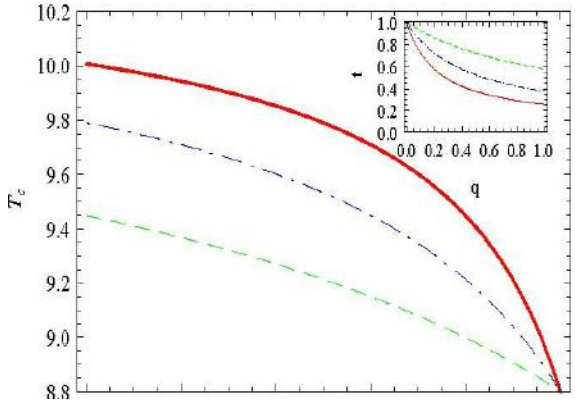

Fig.1 Dependence of T_c on $x = W^2/E_\perp^2$ for $q_0 = 0.8$, *2.0* and 4.0 is depicted by dashed (green), dot-dashed (blue) and solid (red) curves, correspondingly. Insert high lights the *t(q)*dependence according to Eq. (13). T_c(q) increases with q_0 (or $E_\perp$), and saturates to T^* at highest value of the randomness $W = E_\perp$ when $x = 1$.

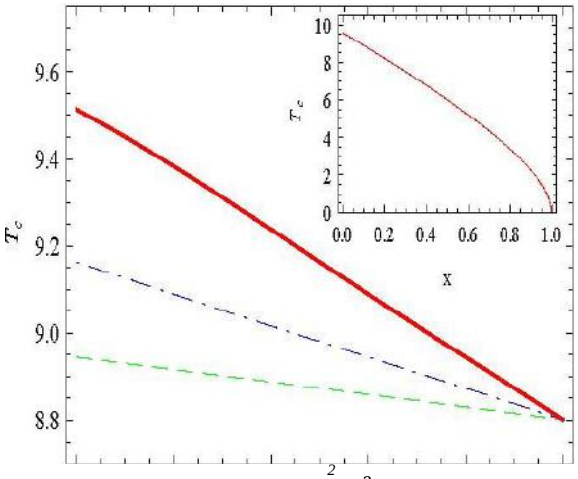

Fig. 2 Dependence of *Tc* on $x = W^2/E_\perp^2$, according to Eq. (22), for a =1.5 and three different values of q_0 : q_0 = 0.8 dashed (green) curve, q_0 =2.0 dot-dashed (blue) curve and q_0 =4.0 solid (red) curve. Insert shows *Tc* (*x*) dependence according to the Abrikosov-Gor'kov's digamma function, which vanishes for higher values of *x*, instead of saturation in our case, and has a concave curvature.

Repeating the procedure of derivation of Eq. (10) for the critical temperature in the case of the classical fluctuations, one reaches to

$$t=\eta E_{\perp} N_s^{(2)}(T)\left(1-\frac{W^2}{E_{\perp}^2}\right)\times \int_0^{1/k_BT} dT \int d^2r \langle cos\big(\varphi(0,0)\big)cos\big(\varphi(r,T)\big)\rangle_0 \qquad (19)$$

The phase-phase quantum correlator for pure 2*D* SC is calculated to yield

$$\langle cos[\varphi(r,\tau)-\varphi(0,0)]\rangle = exp\left\{-\frac{k_BT}{V}\Sigma_{\omega_n}\Sigma_{k>0}\frac{2[1-\cos(k\cdot r-\omega_n\tau)]}{\frac{\hbar^2 N_s^{(2)} k^2}{4\tau n^*}+\frac{\hbar^2}{4}\omega_n^2 K(k)}\right\} \qquad (20)$$

A straightforward calculations result in

$$\langle cos[\varphi(r,\tau)-\varphi(0,0)]\rangle_0 = \begin{cases} exp\left[-\alpha+\frac{\alpha}{\sqrt{\left(\frac{2T_\tau}{\beta}+1\right)^2+\left(\frac{r}{\xi_\parallel}\right)^2}}\right] & \beta>1,\beta_r<\xi_\parallel \\ \left(\frac{\beta\tau}{\xi_\parallel}\right)^{-\alpha\beta_e-\alpha,} & \beta<1,\beta r>\xi_\parallel \\ exp\left[-\alpha\left(\frac{\beta r^2}{8\xi_\parallel^2}+\frac{T_\tau}{\beta}\right)\right], & \beta>1,\beta r>\xi_\parallel \\ (r/\xi_\parallel)^{-\alpha\beta}, & \beta>1, r>\xi_\parallel \end{cases} \qquad (21)$$

where $\alpha = \frac{2}{\pi\xi_\parallel\hbar}\sqrt{\frac{m*}{KN_s^{(2)}}}$ and $\beta = \frac{2k_BT}{\hbar}\xi_\parallel\sqrt{\frac{m^*K}{N_s^{(2)}}}$ are the dimensionless quantum parameters. Although $\alpha = \frac{4\pi k_B T_c^{(2)}}{\varepsilon_F T^{1/2}}\alpha_0$ proportional to the dynamical parameter $\alpha_0 = \frac{1}{2\gamma}\left[\frac{\pi}{(2\hbar^2/m^*)K}\right]^{1/2}$ which characterizes a quantum charging effect in the system, the other parameter $\beta = \frac{T}{\pi T_c^{(2)}\alpha_0\tau^{1/2}}$ depends inversely on α_0, nevertheless the product $\alpha\beta$ does not depend on α_0. Equations (19) and (21) yield a dependence of T_c on $E_\perp$ and W for two limiting cases $\beta > 1$ and $\beta < 1$. In both cases the integration of the correlator (21) over coordinates imposes the restriction $T^* < T_c < T_c^{\langle 2\rangle}$ (or $\alpha\beta > 2$), where T^* is defined by expression (12). For $\beta < 1$, which corresponds to strong charging regime, Eq. (19) after integration over r and τ results in non-linear equation for t

$$q\left\{\frac{t}{2\alpha}+\alpha\left(1+\frac{t^3}{1-t}\right)exp\left(2\sqrt{\alpha/t}\right)\right\}=1, \qquad (22)$$

where, $\alpha = \frac{2\pi^2 k_B T_c^{(2)}\alpha_0^2}{\varepsilon_F}$ characterizes the dynamic effects too, since $a \propto \alpha_0^2$. The numeric solution of Eq. (22) is given in Fig. 2 for $a = 1.2$ and different values of q_0. The quantum fluctuations reduce T_c considerably and alter the results of the classical fluctuations regime at low temperatures and small $E_{\perp,}$ which corresponds to strong randomness or high resistivity in the $T_c(x)$ dependence. The slope of, e.g. the dashed (green) curve with $q_0 = 0.8$ changes from *0.54* in the interval $0 < x < 0.5$ of Fig. 1 for the classic fluctuations regime to the value of *0.30* in the interval $0.5 < x < 1$ of Fig. 2 for the quantum fluctuations regime, the ratio of which *1.8* is comparable with that (~ 2) estimated for the experimental curve.[5]

For $\beta > 1$ Eqs.(19) and (21) are solved in the limit of $2 < \alpha\beta < 8$ yielding

$$T_c = T'(1+q)/\{1+T'q/T_c^{(2)}\}. \qquad (23)$$

The case of $\beta > 1$ and $\alpha\beta > 8$ results in

$$1 = qt^2\{4+1/(1-t)\}, \qquad (24)$$

an approximate solution of which is given by Eq. (16). The case of $\beta > 1$ or $\alpha < 1$ corresponds to weak quantum fluctuations limit, and, therefore, the results do not depend on the dynamical parameter α_0.

In this paper we report disorder effects on T_c of quasi 2D *SCs* with random Josephson coupling. Interplay of non-magnetic disorder with quantum phase fluctuations becomes a central factor in suppression of the superconducting phase in organic quasi-2D *SCs*. A randomness in the interlayer coupling energy is shown to decrease T_c quasi-linearly, nevertheless the superconducting phase does not completely vanish even at arbitrary high strength of the disorder. The present theory explains very well the recent experimental measurements given in Refs.[5,6]. We neglect in this article effects of in-plane disorder on T_c inorganic *SCs*. Such kind randomness results in suppression of T_c due to the Anderson localization for non-s-wave pairings, and it seems to destroy homogeneity of the order parameter modulus leading to formation of a cluster-like "superconducting island" inside the metallic phase. On the other hand the in-plane disorder may "pin" the Kosterlitz-Thouless topological defects and destroy the quasi-long range order in the system. All these effects deserve further investigation.

This research was supported by the DFG under Grant No. Op28/8-1 and by the government of the Azerbaijan Republic under Grant No. EIF-2010-1(1)-40/01-22.

[1] *J.M. Williams* et al., Science 252, 1501(1991).
[2] *T. Ishiguro, K. Yamaji, and G. Saito*. Organic Supercon ductors (2nd Edn., Springer-Verlag, Heidelberg, 2006).
[3] *W.K. Kwok* et al., Phys. Rev. B 42, 8686(1990).
[4] *B.J. Powell and R.H. McKenzie*. Phys.Rev.B 69, 024519 (2004).
[5] *J.G. Analytis* et al., Phys. Rev. Lett. 96, 177002(2006).
[6] *T. Sasaki* et al., J. Phys. Soc. Jpn. 80, 104703(2011).

[7] *E. Nakhmedov and R. Oppermann*, Phys. Rev. B 81, 134511(2010)
[8] *A.A. Abrikosov and L.P. Gor'kov*. Zh.Eksp.Teor.Fiz. 35, 1558(1958) [Sov.Phys.JETP 8, 1090(1959)].
[9] *E.P. Nakhmedov and Yu.A. Firsov*, Physica C 295, 150, (1998)
[10] *V.J. Emery and S.A. Kivelson*, Nature 374, 434(1995); Phys. Rev. Lett. 74, 3253(1995).
[11] *T.M. Rice*, Phys. Rev. A 140, 1889(1965).
[12] *J.M. Kosterlitz and D.J. Thouless*, J. Phys. C 6, 1181 (1973);P. Minnhagen, Rev. Mod. Phys. 59, 1001(1987).
[13] *K.B. Efetov and A.I. Larkin*, Zh.Eksp.Teor.Fiz. 66, 2290 (1974)[Sov.Phys.JETP39, 1129(1975)].
[14] *V.Ambegaokar,U.Eckern,andG.Sch*¨on,Phys.Rev.Lett. 48, 1745(1982); Phys.Rev. B 30, 6419(1984).

Received: 02.11.2012

NONEQUILIBRIUM ELECTRONIC PROCESSES IN SINGLE CRYSTALS GaS ACTIVATED BY RARE-EARTH ELEMENTS

B.G. TAGIYEV[1,2], O.B. TAGIYEV[1,3], S.A. ABUSHOV[1], G.U. EYUBOV[1]

[1]Institute of Physics named after G.B.Abdullayev of Azerbaijan National Academy of Sciences

[2]Azerbaijan National Air Academy

[3]Baku branch of MSU named after M.V.Lomonosov

The present paper is the result of complex experimental investigations of injection currents, photoconductivity, luminescent properties (Stocks and anti-Stocks luminescence), thermoluminescence in GaS layered crystals doped by rare-earth elements: Er, Yb, Tm. The mechanisms are established by analysis of obtained results on the base of theories and models: charge transition, photoconductivity, Stocks and anti-Stocks luminescence, thermoluminescence. The parameters of photosensitive and luminescence centers; Stark structures of radiative levels of REE Er^{3+}, Yb^{3+}, Tm^{3+}; trap parameters are defined.

Keywords: injection points, photoconductivity, luminescence, thermoluminescence.
PACS: SQ 621.315.592.

INTRODUCTION

Last time the influence of rare-earth elements **(**REE) impurities on electric, photoelectric and optic properties of different semiconductor compounds is widely investigated. These impurities increase the photosensitivity, create the photoluminescent centers in materials, that makes them perspective ones from the photoresistor and luminophor formation point of view.

The complex current investigations limited by space charge (CLSC), photoconductivity (PhC) and photoluminescence (PhL) allows us to judge by such important trap parameters: depth of occurrence, capture factor and concentration and also to obtain the information about distribution character of local levels, to reveal the mechanism of current passing and charge accumulation in weak and strong electric fields.

The nonequilibrium electronic process problem takes especial place in general investigation complex of semiconductor properties. The investigation of these processes are very important at studying of new materials from deepening and expansion of information point of view both fundamental and applied character. Such nonequilibrium phenomena as photosensitivity, photoluminescence, photo-e.m.f. and others are in the work foundation of modern semiconductor devices. The study of such nonequilibrium phenomena in GaS from $A^{III}B^{VI}$ group activated by REE presents the scientific and practice interest.

The development of semiconductor electronics stimulates the search of semiconductor materials with wide application possibilities. The favorable combination of series of electric, photoelectric, luminescent and optic properties of wide-band semiconductors of GaS type makes them perspective materials for formation of different semiconductor devices on their base, for them the single crystal obtaining technology is well developed, they have transparency in wide spectral interval. This position stimulates the intensive structure investigation of luminescent centers and physicochemical conditions of their formation in crystals of GaS type.

The interest to semiconductors with wide forbidden band (2,5÷4,0 eV) is caused by whole series of tasks appeared before semiconductor technology. The formation of semiconductor devices working at high temperatures and big work voltages, and also are able to register and generate both visible and infrared radiation, can be related to such tasks.

The investigation results of current passing, photoconductivity, Stocks and anti-Stocks radiations and thermoluminescence of GaS single crystal, activated by REE: Er, Yb,Tm are given in the present work.

EXPERIMENT TECHNIQUE

The synthesis technology of GaS compound activated by REE (Er, Yb, Tm) and single crystal growing of this material with the given REE and also device for investigation of electric and luminescent properties (photo- and thermoluminescence) of obtained single crystals are described.

GaS compound is the solid substance of light-yellow color, melts without decomposition at 1015°C [1]. This compound is the phase of constant composition, is more stable on air in comparison with other gallium sulfides (for example, Ga_2S) [2].

GaS compound doped by REE (Er, Yb, Tm) is synthesized by alloying of corresponding components taken in stoichiometric relations. The gallium by B-4 (99.999%) type and sulfur by B-4 (99.999%) are used as original materials.

The impurities of erbium, ytterbium and thulium are introduced in blend before synthesis. All single crystals obtained by us are grown at slow ingot cooling at constant temperature gradient by modified Bridgman method and they have p-type conductivity with specific resistance 10^9–10^{11} Ohm·cm at room temperature. The gallium sulfide is the layered semiconductor that allows us to obtain very thin monocrystalline samples with native mirror faces by cleavage method not requiring the special treatment.

The samples are prepared by the cleavage from big ingots for measurements of electric properties. The ohmic contacts are prepared by alloying or evaporation in indium vacuum on opposite, perpendicular *c* axis, mirror surfaces.

The photoluminescence is investigated on SDL-1 and HR-460 (Jobin-Ivon Spectrometer HR 460) devices. The helium-cadmium laser (λ_{exc}= 441.6 nm) and impulse nitrogen laser (Laser Photonics LN 1000, impulse energy

is 1.4 mJ, impulse duration is 0.6 ns) are the sources of excitation. The radiation of reconstructed continuous titanium-sapphire laser of power up to 1000 mW is used for excitation on wave length λ=980 nm.

At photoluminescence investigation the photoelectronic multipliers FEM - 39 and FEM -62 are used on SDL-1. At impulse excitation the signal from FEM is given on integrator PAR-160, and then the signal is given from integrator to automatic recorder CSP-4.

RESULTS AND THEIR DISCUSSION

The ohmic, quadratic law sections and current strong increase region are observed on VAC of many investigated GAS crystals of activated REE (Er, Yb, Tm) (fig.1).

Besides these regions in GaS:Er crystals(fig.1a) between quadratic region and strong current increase one the cubic section is observed on VAC and in GaS:Tm the section of three-two ($J \sim U^{3/2}$) (fig.1d) is observed.

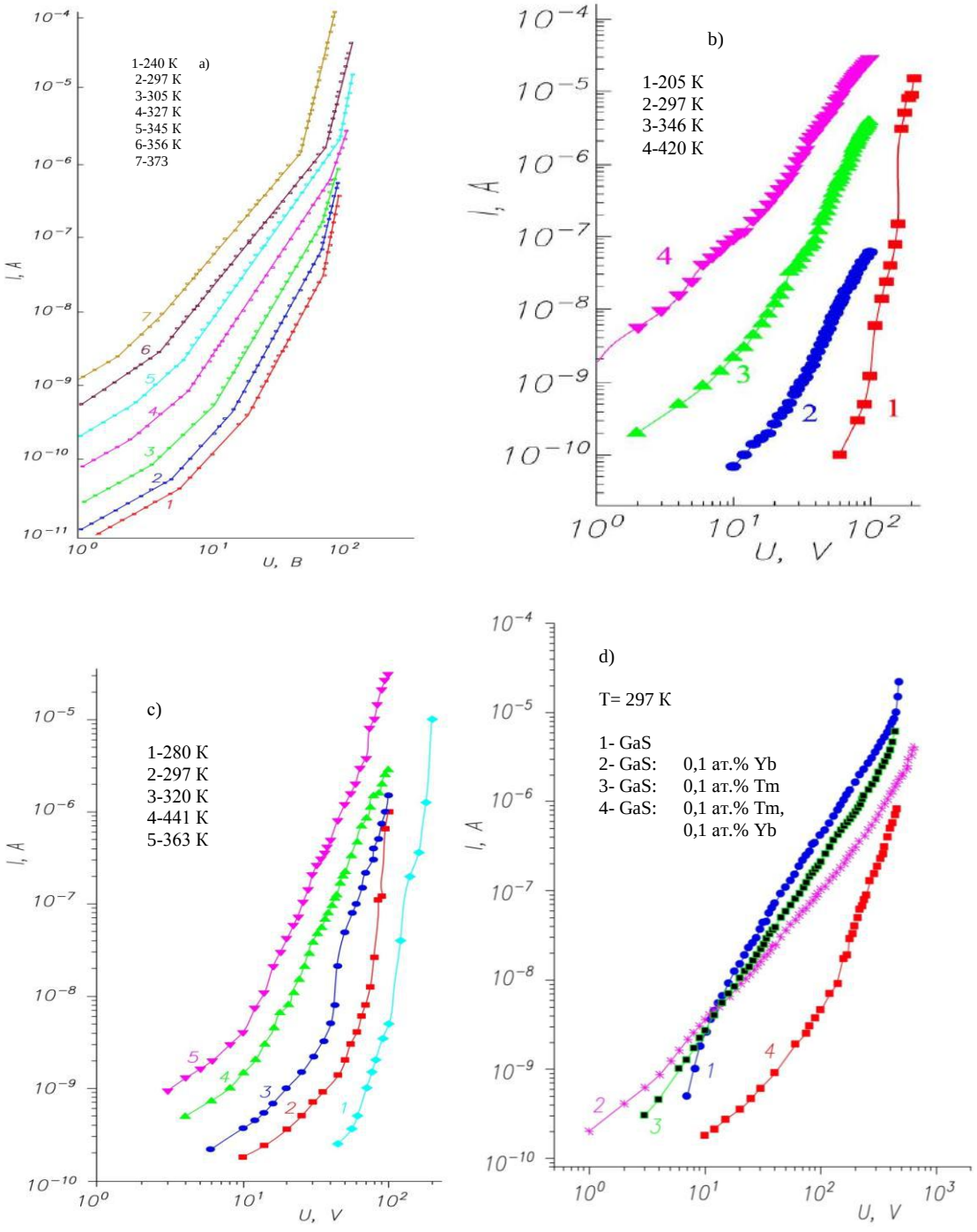

Fig. 1. VAC of GaS single crystals: Er (fig.1a), GaS: Er, Yb (fig.1b), GaS: 0,1 at.% Tm, 0,1 at.% Yb (fig.1c) at different temperature and GaS (1), GaS: 0,1 at.% Yb (2), GaS: 0,1 at.% Tm (3) at 297 K (fig.1d).

The presence the quadratic law section on VAC and condition $J \sim L^{-3}$, $U_{LTF} \sim L^2$, $\theta = \frac{n_0}{n_t} << 1$(where J is current density in quadratic law region VAC, L is distance between electrodes, U_{LTF} is voltage value corresponding to trap filling, θ is capture factor, n_0 is concentration of free charge carriers, n_t is concentration of captured charge carriers), and also the presence of residual charge after electric field influence from non-linear VAC region show that charge carrier transfer in strong electric field region for single crystals GaS doped by Yb, Er, Tm is caused by monopolar injection (in GaS crystals: Er up to definite values of electric fields ($j \sim L^{-3}$)).

The presence of cubic section in GaS single crystals doped by Er shows on the fact that current passing mechanism at high excitation levels is caused by double injection and current density for this region is expressed by following formula (current dielectric mode) [3]:

$$j = \frac{125}{18} \varepsilon \varepsilon_0 \mu_n \mu_p \tau \frac{V^3}{L^5}, \qquad (1)$$

where ε is dielectric constant, ε_0 is electric constant, μ_n and μ_p are motilities of electrons and holes correspondingly, τ is life time of free charge carriers. At conclusion (1) it is predicted that τ doesn't depend on injection level.

The life time of charge carriers calculated by formula (1) is 1,1μsec.

The cubic section is revealed in fields ~$5 \cdot 10^3$ V/cm and beginning from fields $2 \cdot 10^4$ V/cm and higher, the cubic law is destroyed and the rapid current increase region begins. The presence of cubic section between quadratic law and rapid current increase shows that at definite injection levels the charge carrier transfer isn't limited by monopolar injection and the charge carrier capture process changes with injection level increase. This change influences on charge carrier life-time that changes the recombination kinetics. The space charge on recombination levels changes with capture change. If concentration of deep levels is small in the comparison with charge carrier concentration then at above mentioned conditions and without existence of negative resistance the double injection can take place. The temperature dependence results of capture factor and electric conduction are presented on fig.2.a,b.

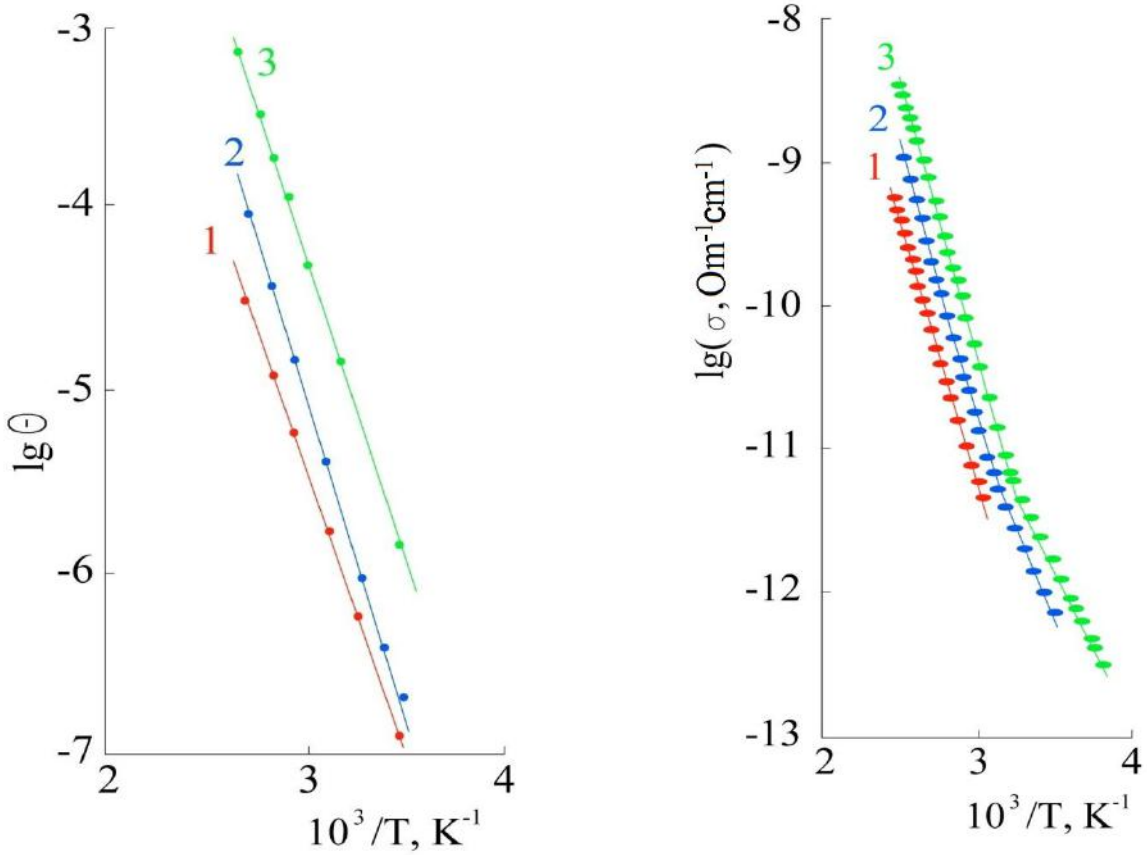

Fig.2. a is the capture factor calculated from quadratic law region VAC for GaS single crystals doped by different erbium concentrations (at.%). 1-0,01; 2-0,5; 3-0,1;
b is temperature dependence of electric conduction for GaS single crystals doped by different erbium concentrations (at.%) 1-0,01; 2-0,1; 3-0,5.

The capture parameters in GaS single crystals defined on the base of experimental data obtained from measurements of electric conduction temperature dependence, injection currents, are presented in the table 1.

Table 1.

Trap parameters / Materials	Trap occurrence depth, eV			Trap concentration, cm^{-3}	Capture factor, θ
	VAC	σ(T)	θ(T)		
GaS	0.61			$2.40 \cdot 10^{13}$	$9.29 \cdot 10^{-4}$
GaS: 0.1ат. % Tm	0.66			$2.47 \cdot 10^{13}$	$2.95 \cdot 10^{-4}$
GaS: 0.1 ат. % Yb	0.64			$9.23 \cdot 10^{12}$	$3.06 \cdot 10^{-4}$
GaS: 0.01 ат.% Er	0.78	0.73	0.62	$3.97 \cdot 10^{12}$	$5.19 \cdot 10^{-6}$
GaS: 0.1 ат. % Er	0.76	0.80 0.52	0.68	$2.1 \cdot 10^{12}$	$2.04 \cdot 10^{-5}$
GaS: 0.5 ат. % Er	0.79	0.80 0.43	0.72	$5.1 \cdot 10^{12}$	$2.13 \cdot 10^{-6}$
GaS: 0.01 ат. % Yb, 0.03 ат. % Er	0.61 0.79 0.82	0.66		$5.8 \cdot 10^{12}$	$2.63 \cdot 10^{-3}$
GaS: 0.1ат. % Tm, 0.1 ат. % Yb	0.80	0.62	0.58	$3.25 \cdot 10^{13}$	$6.36 \cdot 10^{-7}$

The maximum at 470 nm and weak maximums in impurity absorption region at 550, 630 and 800 nm are revealed in spectra of PhC single crystals GaS doped by ytterbium (fig.3).

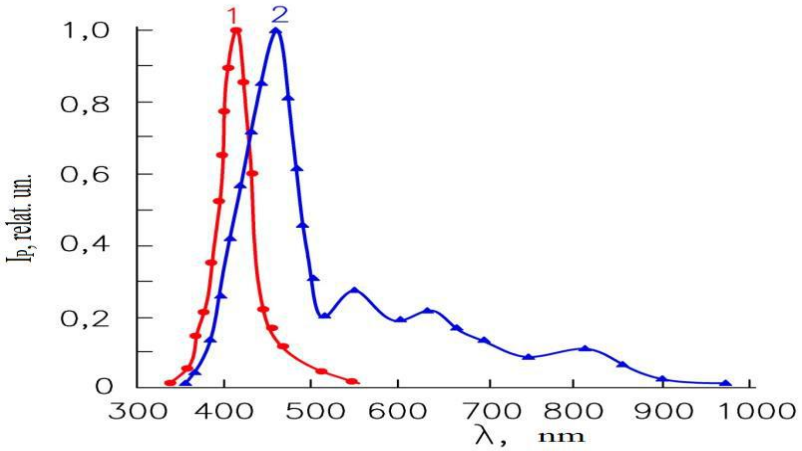

Fig.3. The spectral distribution of photoconductivity of GaS single crystals: Yb at 77K (curve1) and 293 K (curve 2).

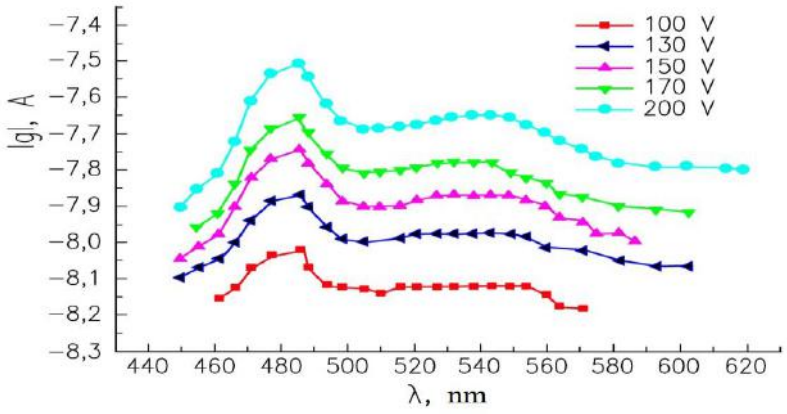

Fig. 4. The spectral distribution of photoconductivity GaS: 0,01 at. % Yb, 0,03 at . % Er at 95 K and at different voltages.

The peaks of photoconductivity are observed at relative high temperatures (250-300K). The temperature dependence of impurity photoconductivity in single crystals GaS doped by ytterbium, has the activation character, i.e. the impurity conduction at high temperatures is caused by thermo-optical electron transitions on acceptor levels and further their transfer in conduction band.

In GaS single crystals: Yb, Er at 95K PhC spectrum the one branch at 463nm is observed, one intensive maximum at wave length 486nm and relative weak maximum at 543nm are observed (fig.4). The photo-current increase with voltage increase applied to samples. The photo-current increases with temperature increase up to 200K and further temperature increase leads to its decrease. The spectrum maximums shift to long-wave region with temperature increase (fig.5).

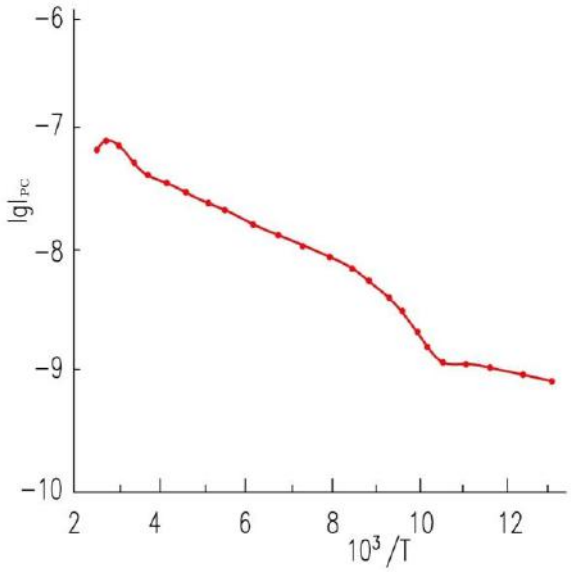

Fig.5. Temperature dependence of photoconductivity in GaS single crystal:0,15 at.% Yb.

The short-wave –branch observable on curve of photo-current spectral distribution at 463nm is connected with band-to-band transfers and exciton photo-active decay, i.e. with eigen photoconductivity. The second intensive maximum with wave length 503nm at 300K is possibly connected with photo-active decay of indirect excitons [4,5].

The photo-current in photosensitivity wide band region with maximum at 543nm strongly depends on impurity content Yb, Er in GaS: the photo-current in this spectrum region increase with increase of component percent composition of REE couple from 0.01 up to 0.1at%, and further impurity increase leads to photro-sensitivity decrease. Such impurity maximum in PhC spectra is observed in work [6-8] where it is established that sulfur vacancies in GaS crystals form the acceptor level with ionization energy 0,25eV and are the reason of p-type conduction. Unlike GaS crystals activated by Yb photo-current temperature dependence $lgI_{ph}\sim10^3/T$ GaS: Yb, Er has the peculiarity which is that eigen photoconductivity with temperature increase increases and photo-current firstly increases up to definite temperature (95÷200 K) and further decreases in interval 200÷300 K in GaS single crystals activated by RRE couple Yb and Er. Probably, this is connected with formation of new s-centers of rapid recombination in forbidden band which activate after definite temperature that leads to photo-current damping. From temperature photo-current dependence constructed in $lgI_{ph}\sim10^3/T$ coordinates the activation energies of r- and s-centers of recombination are defined: 0.2 eV and 0.8 eV, correspondingly (fig.7).

The bands caused by edge emissions, narrow emission bands overlapping the wave length region 500÷1650 nm caused by ion intra-central transitions Er^{3+}, Yb^{3+} and Tm^{3+} are observed in GaS single crystals activated REE (Er, Yb, Tm) on PhL spectrum. The positions of Stark components of REE levels for radiation centers giving the most contribution in luminescence intensity in GaS single crystal are defined on the base of experimental investigations of luminescence spectra, luminescence kinetics.

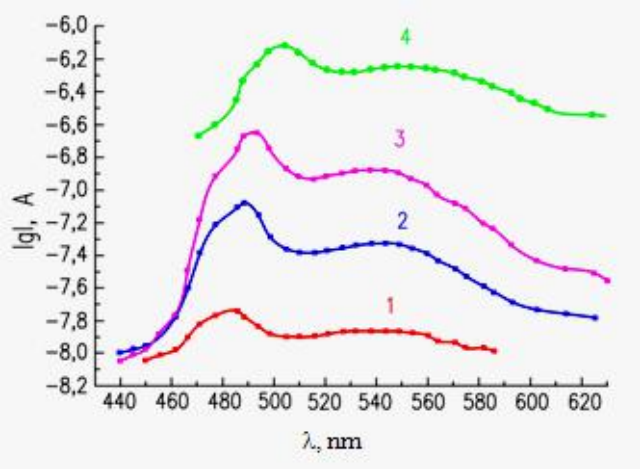

Fig.6. The spectral distribution of photoconductivity GaS: 0,01 at. % Yb, 0,03 at. % Er at 150 V and different temperatures (K): 1– 95, 2– 160, 3– 200, 4– 300.

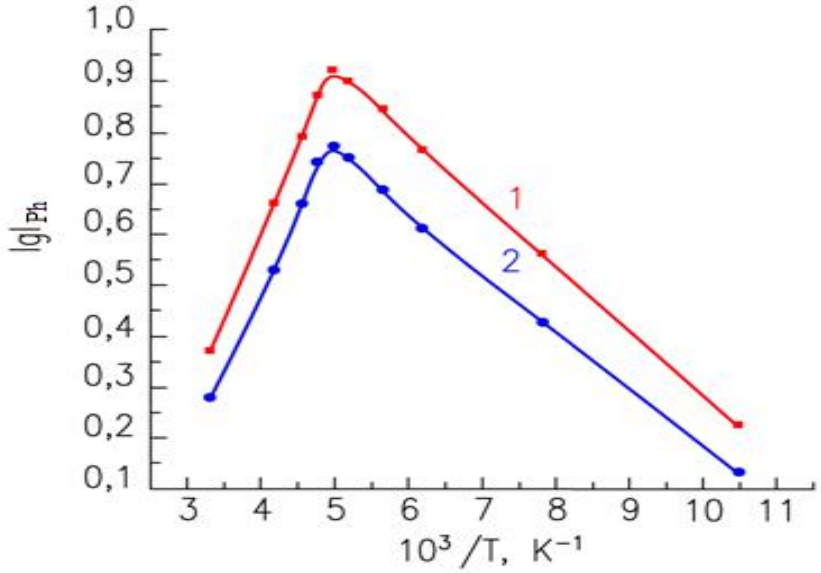

Fig. 7. The photo-current on temperature for GaS: 0,01 ат. % Yb, 0,03 at. % Er: 1 is eigen and 2 is impurity maximums.

In GaS single crystals: Tm in PhL spectra besides edge emission in temperature interval 77÷300 K in wave length region 685÷1550 nm, the series of narrow bands caused by intra-central *f–f* transitions of Tm^{3+} ($^3F_2 \rightarrow {}^3H_6$, $^3F_3 \rightarrow {}^3H_6$, $^3F_4 \rightarrow {}^3H_6$, $^3H_5 \rightarrow {}^3H_6$ $^3H_4 \rightarrow {}^3F_4$) ion is observed (fig.8); in GaS single crystals: narrow bands caused by intra-central transfers of Er^{3+} ($^4S_{3/2} \rightarrow {}^4I_{15/2}$, $^4F_{9/2} \rightarrow {}^4I_{15/2}$, $^4I_{9/2} \rightarrow {}^4I_{15/2}$, $^2H_{11/2} \rightarrow {}^4I_{13/2}$ and $^4S_{3/2} \rightarrow {}^4I_{13/2}$) ion are observed in wave length region Er (fig.9) and in GaS single crystals: Yb in wave length region 980÷1050 nm the narrow bands caused by intra-central transfers of Yb $^{3+}$ ($^2F_{5/2} \rightarrow {}^2F_{7/2}$) ion are observed (fig.10).

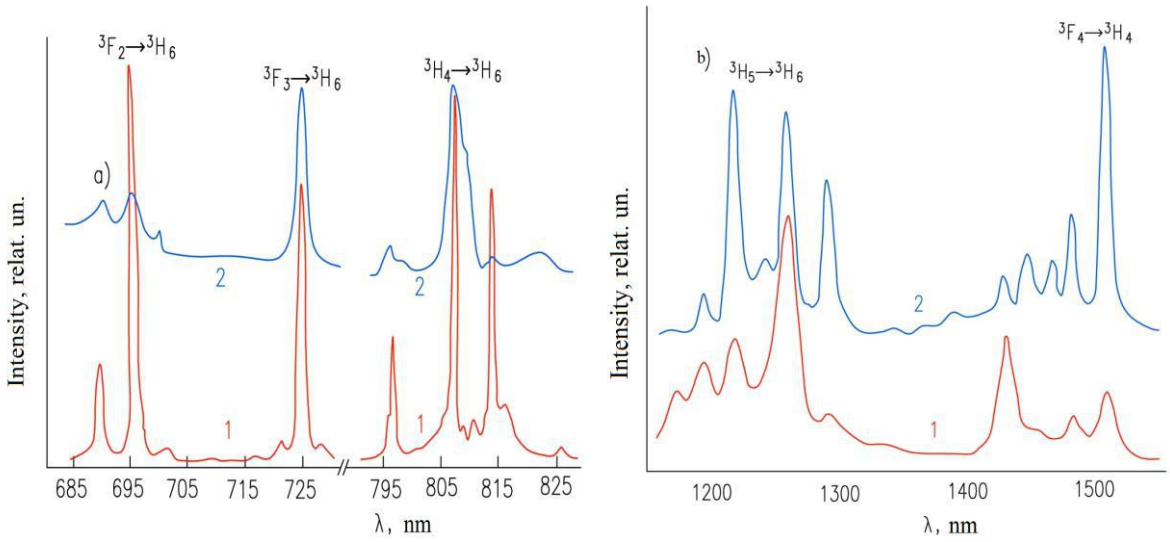

Fig. 8. PhL spectra Tm^{3+} in GaS at λ_{exc}=441.6 nm:a) curve 1 at 77 K, curve 2 at 300 K; b) curve 2 at 77 K, curve 1 at 300 K.

The analysis of luminescence spectra Tm in GaS (fig.8) shows that emission takes place simultaneously from several Stark components of the one and the same level. This fact is used at definition of Stark structure of Tm^{3+} ion levels in GaS. The total disappearance of line 1240nm in $^3H_5 \rightarrow {}^3H_6$ transition with temperature increase from 77 up to 300K says about the fact that this line is caused by the lowest Stark component of $^3H_5$ level. The spectra on which the intensity decrease of line 1500nm is observed and increase of one of 1413nm transition $^3H_4 \rightarrow {}^3F_4$ with temperature increase from 77 up to 300K, allows us to define two low Stark components of $^3F_4$ level in GaS.

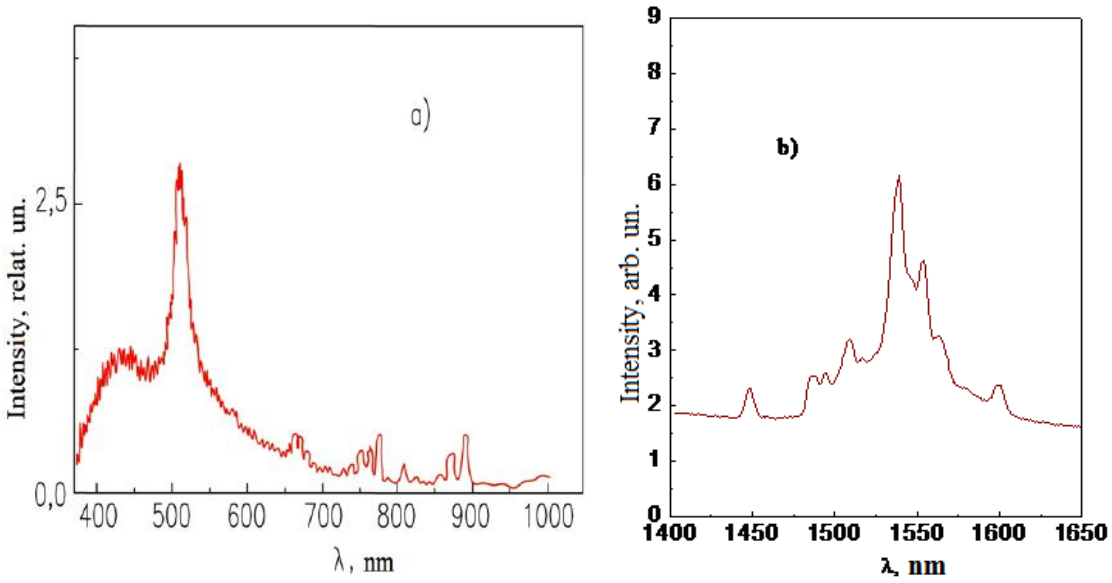

Fig. 9. PhL spectra of GaS single crystals: Er^{3+} (0.1 at. %) at λ_{exc}= 337,1 nm (a) and at λ_{exc} = 976 nm (b) and T= 300 K.

The luminescence kinetics at intra-band excitation of Tm^{3+} ions at 77K connected with $^3F_3 \rightarrow {}^3H_6$, $^3F_4 \rightarrow {}^3H_6$ transfers has the exponential character (fig.11) and life-time of excited states of $^3F_3$ and $^3H_4$ are ~20 and 100μsec, correspondingly. The luminescence damping connected with $^2F_{5/2} \rightarrow {}^2F_{7/2}$ transfer of Yb^{3+} ion in GaS (fig.11) also has the exponential character and life-time of excited state $^2F_{5/2}$ is ~140μsec in temperature region 77-270K (fig.12).

The kinetics of $^4S_{3/2} \rightarrow {}^4I_{15/2}$ transfer decay of Er^{3+} in GaS single crystals: Er takes place on exponential law. In GaS: Er life-time of excited level $^4S_{3/2}$ Er^{3+} at 77K is 2μsec (fig.13).

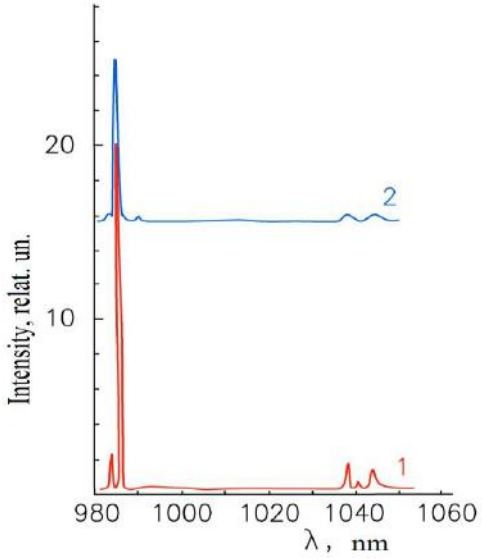

Fig. 10. PhL spectra of GaS: 0,15 at. % Yb^{3+} at λ_{exc}=441.6 nm:1– 77 K, 2– 293 K.

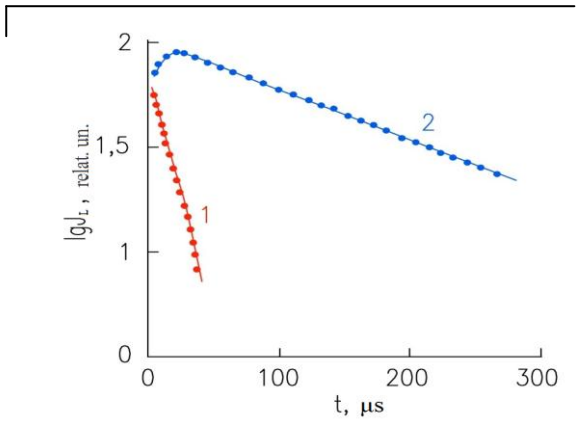

Fig. 11. The decay kinetics of excited states $^3F_3$ (1) and $^3H_4$ (2) in GaS: Tm at excitation in conduction band (λ_e= 353 nm, T= 77 K).

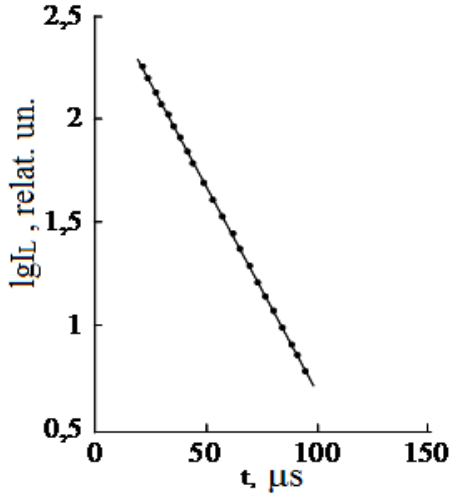

Fig. 12. The decay splot of excited states 1– $^4S_{3/2}$ Er^{3+} in GaS single crystals: Er at excitation by short light impulse with wave length λ=0,53 μm.

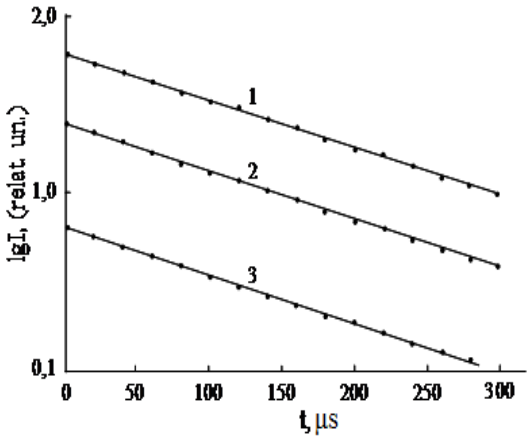

Fig. 13. The damping kinetics of PhL Yb^{3+} in GaS: 0.15at.% b^{3+} at different temperatures (K): 1– 77, 2– 170, 3– 270.

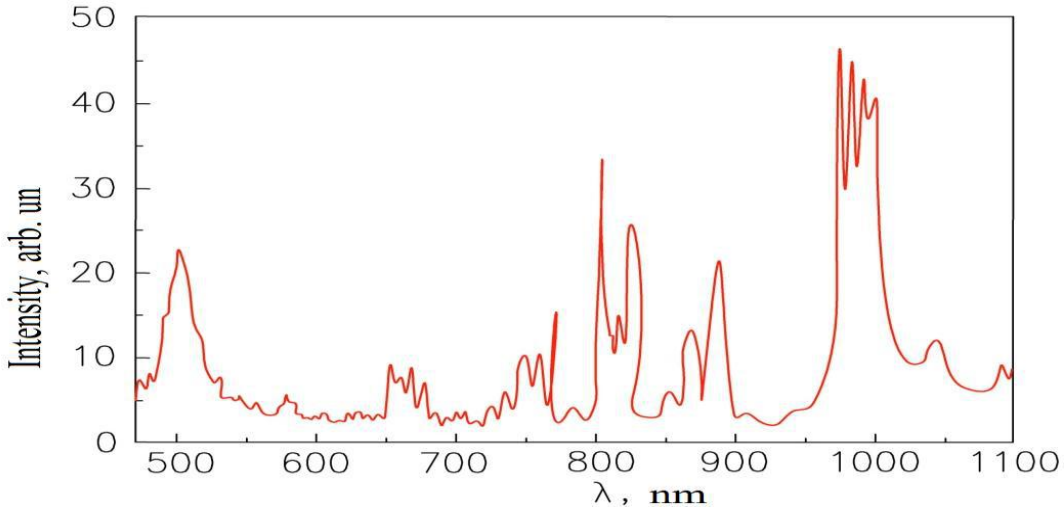

Fig. 14. PhL spectra of GaS single crystals: Er, Yb (by 0.1 at. % each) at λ_{excit}= 337,1 nm and T = 300 K.

The photoluminescence spectrum of GaS: Er^{3+} (0.1 at.%) при $\lambda_{exc.}$=337.1 nm and 300K consists of intensive wide-band (λ=480÷600 nm) and weak narrow-band regions (λ=650÷900 nm) (fig.9a). The wide-band emission has the maximum at 511nm and narrow-band region consists from separate narrow bands λ=650÷700 nm, λ=700÷800 nm, λ=800÷900 nm.

The spectrum of PhL crystal of GaS: Er^{3+}, Yb^{3+} at $\lambda_{exc.}$= 337.1 nm (fig.14) has the more wide of wave length. Unlike spectrum PhL of GaS: Er^{3+} in GaS spectrum: Er^{3+}, Yb^{3+} (on 0.1 at.% each) the narrow band intensity in region 650-900nm increases and the new-narrow-band emission consisting of some overlapping intensive narrow bands appears in region 900-1100nm.

The narrow-band emission in 650÷900 nm region is connected with intra-centered transfers $^4S_{3/2} \rightarrow {}^4I_{15/2}$ (525-600 nm), $^4F_{9/2} \rightarrow {}^4I_{15/2}$ (640-700 nm), $^4I_{9/2} \rightarrow {}^4I_{15/2}$ (700-800 nm), $^2H_{11/2} \rightarrow {}^4I_{13/2}$ (800-850 nm), $^4S_{3/2} \rightarrow {}^4I_{13/2}$ (850–900 nm) of Er^{3+} ion.

The emission intensity increase of PhL narrow bands in region of wave length 650-900nm and appearance of new intensive narrow bands in 900-1050nm in emission spectrum GaS: Er^{3+} and Yb^{3+} are probably connected with introduction of Yb^{3+} ion in these crystals. It is known that Er^{3+} and Yb^{3+} have the resonance excited $^2F_{5/2}$ и $^4I_{11/2}$ levels correspondingly and РЗИ in GaS single crystals excite through fundamental absorption bands and exciton states. That's why the energy transformation from excited level $^2F_{5/2}$ of Yb^{3+} ion to excited level $^4I_{11/2}$ of Er^{3+} ion is possible, i.e. Yb^{3+} ions play the sensibilizator role of Er^{3+} luminescence.

At excitation of GaS single crystal: Er^{3+} (0.1 at. %) at 300 K by IR radiation (λ_{exc}=976 nm) the anti-Stocks luminescence and Stocks one are observed (fig.15). The anti-Stocks luminescence has the spectral region 475—575nm and consists of four narrow bands. The first narrow intensive band (λ = 489 nm) overlaps with less intensive second band (λ = 495 nm), third (λ = 529 nm) and fourth (λ = 549.7 nm) bands are divided and each of them also consists of two bands.

Stocks luminescence has the wave length range 1425÷1625 nm.

At GaS crystal excitation: Er^{3+}, Yb^{3+} by IR radiation (λ_{exc}=976 nm) the anti-Stocks luminescence in spectrum region 500÷600 nm in the form of two narrow peaks is observed: at 527 and 549nm, and in nearest IR-region

(1450÷1650 nm) the narrow-band Stocks luminescence is observed (fig.16). The intensity of anti-Stocks luminescence is essentially less than intensity of Stocks one.

The dependences of anti-Stocks and Stocks luminescence on power of excited IR radiation (λ_{exc}=976 nm) в GaS: Er^{3+} and GaS: Er^{3+}, Yb^{3+} are investigated for revealing of anti-Stocks luminescence (fig.17).

At increase of excited IR radiation the almost quadratic law intensity growth of anti-Stocks luminescence shows what takes place the consistent absorption of two photons by Er^{3+} one ion (fig.18).

At GaS crystal excitation: Er^{3+}, Yb^{3+} (fig.19) by laser IR radiation (λ_{exc} = 976 nm) the electron passes from the main level $^2F_{7/2}$ on excited one $^2F_{5/2}$ of Yb^{3+} ion (transition 1), being on distance ~10000 cm^{-1}, further the energy transfer from $^2F_{5/2}$ to excited one $^4I_{11/2}$ of Er^{3+} ion (transition 2).

As a result of this transition Er^{3+} ion receiving the energy, passes to higher level $^4F_{7/2}$ (transition 3) and after thermal relaxation the transition $^4S_{3/2} \rightarrow {}^4I_{15/2}$ (transition 4) is carried out with emission in 550nm region. Simultaneously, the thermal relaxation from level $^4I_{11/2}$ on the level $^4I_{13/2}$ (transition 5), further the transition $^4I_{13/2} \rightarrow {}^4I_{15/2}$ (transition 6) 1550nm. (The supposed scheme of energy transformation from Yb^{3+} to Er^{3+} at excitation by titanium-sapphire laser (λ_{exc}= 976 nm) is presented on fig.19).

The thermoluminescence spectrums of GaS single crystals: Yb is investigated at heat velocities β= 0.67 K/c, 1.96 K/c (fig. 20). The thermoluminescence GaS spectrum: Yb presents itself the wide band having the temperature region 100÷440 K and consisting from five overlapping bands with maximums near 140, 164, 204, 306 and 376 K. The band intensity increases with increase of heat velocity. The band half-widths are equal to 26, 33, 69, 50 and 50 K correspondingly. The low-temperature part of first band has the big length ($T_m–T_1>T_2–T_m$) than high-temperature one. This corresponds to kinetics of first order (fig.20).

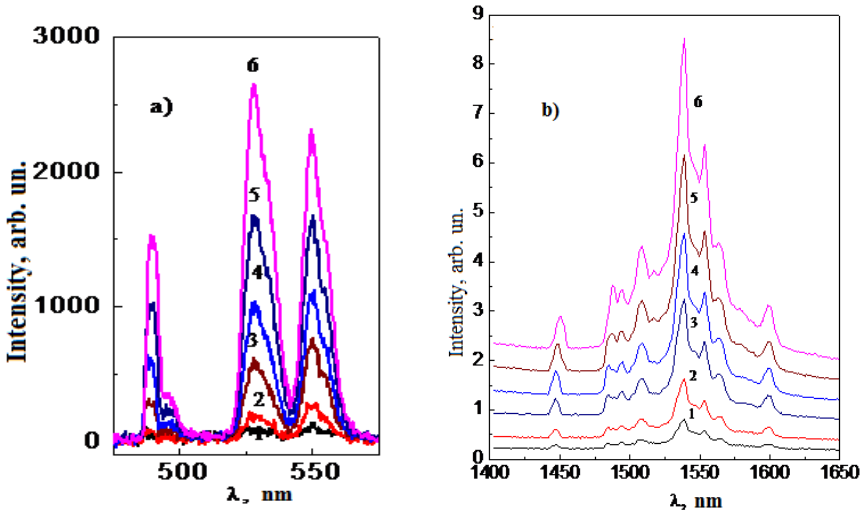

Fig. 15. The spectra of anti-Stocks (a) and Stocks (b) luminescence of GaS: Er^{3+} (0,1 at. %) at power of excited IR radiation 100 (1), 200 (2), 400 (3), 600 (4), 800 (5), 1000 mW (6), λ_{exc} = 976 nm and T= 300 K.

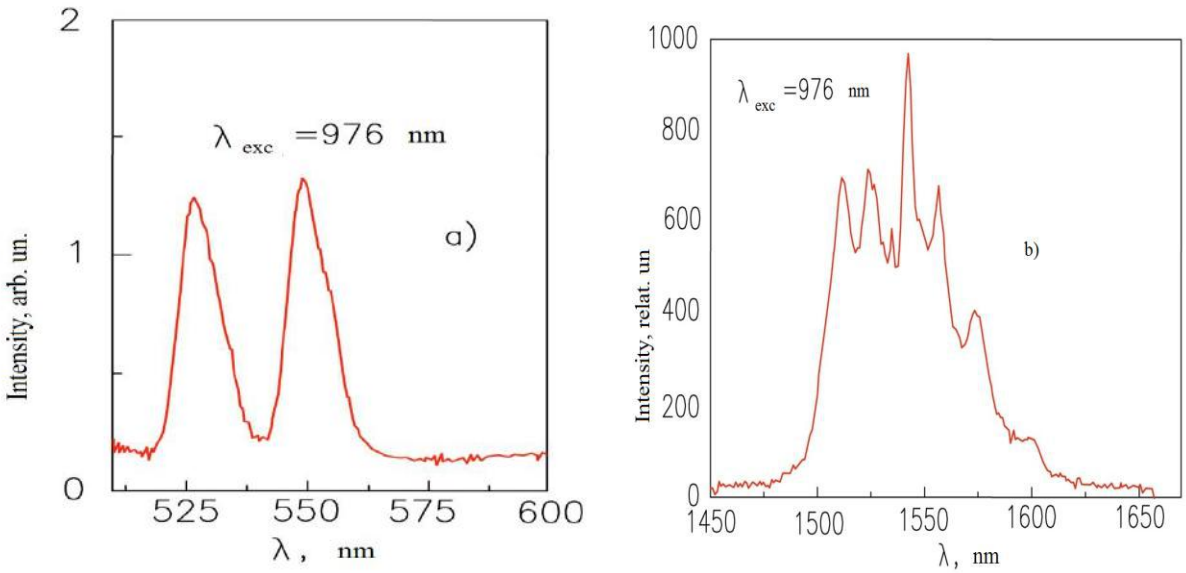

Fig.16. The spectra of anti-Stocks (a) and Stocks (b) luminescence of GaS: Er, Yb (by 0,1 at. % each) at $\lambda_{exc.}$= 976 nm and T= 300 K.

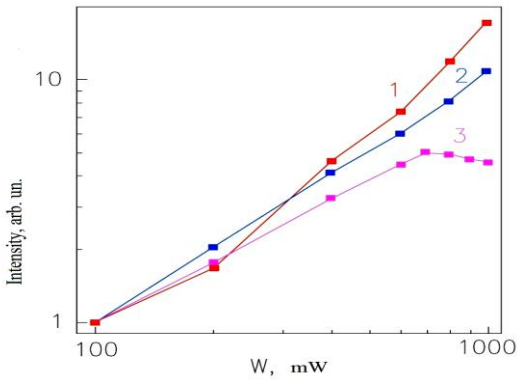

Fig.17. The dependences of intensity of anti-Stocks (1), Stocks (2) luminescence of GaS: Er^{3+} and intensity of Stocks luminescence GaS: Er^{3+}, Yb^{3+} (3) on power of excited IR- radiation.

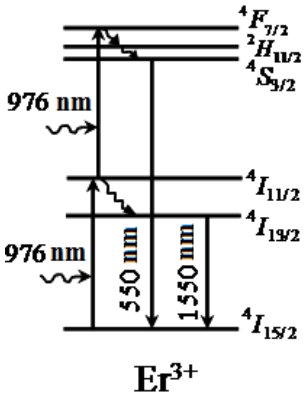

Fig. 18. The scheme of IR radiation transformation (λ_{exc}= 976 nm) into visible (λ =550nm).

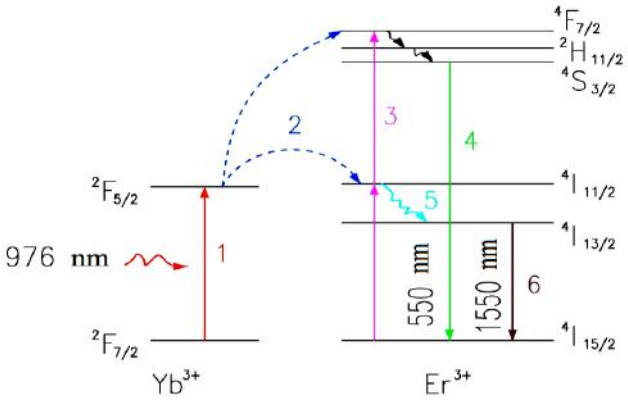

Fig. 19. The scheme of energy transformation from Yb^{3+} ion to Er^{3+} ion in GaS: Er^{3+}, Yb^{3+} at λ_{exc} = 976 nm.

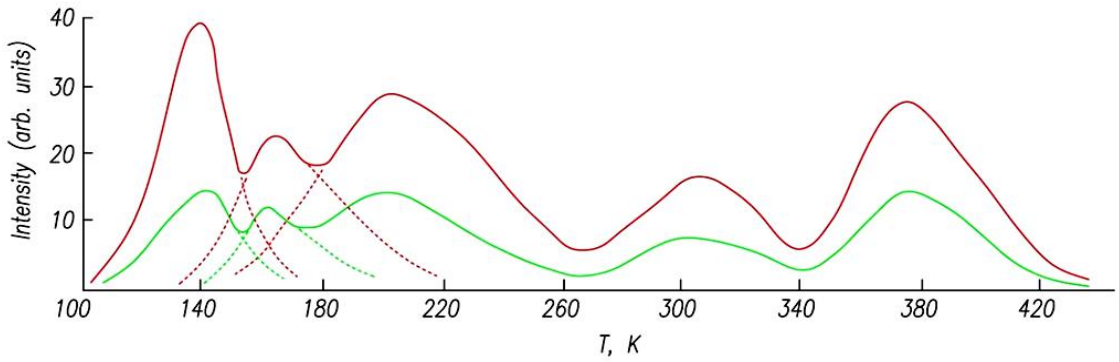

Fig. 20. The spectrum of thermoluminescence of GaS single crystals: at different heat velocities (K/c): 1-0,67; 2-1,96.

The length of rest four bands of high-temperature region is bigger than low-temperature one, i.e. for them the kinetics condition of second order (T_m-T_1<T_2-T_m) is carried out. The investigation results of TL are analyzed on the base of theories and models developed in works [9-12], the electron trap parameters are defined GaS: Yb, such as activation energy (E_t=0.30; 0.35; 0.43; 0.65 and 0.81 eV), frequency factors (S=$1.3\cdot10^{13}$; $4.9\cdot10^{11}$; $2.6\cdot10^{9}$; $1.4\cdot10^{8}$ and $1.8\cdot10^{11}$ sec^{-1}).

---

[1] *P.Q. Rustamov, B.N. Mardaxaev, M.Q. Safarov.* Izv.AN SSSR, Neorq. Materiali, 3,479,1967. (In Russian).

[2] *Z.S. Medvedeva.* Xalkoqenidi elementov IIIB podqruppi periodicheskoy sistemi. Izdatelctvo «Наука», Mockva, 1968, 216s.(In Russian).

[3] *M.A. Lampert , P. Mark.* Current injection in solids. Academic Press New York and London, 1970.

[4] *Q.L. Belenkiy, M.O. Qodjaev, E.Yu. Salaev.* Nepryamie eksitoni v sulfide qalliya // Pisma v JETF, 1977, t. 26, №5, s. 385-388.(In Russian).

[5] *A. Mercier, E. Mooser, J.P. Voitchovsky*. Near edge optical absorption and luminescence of GaSe, GaS and of mixed crystals // J. Luminescence, 1973, v. 7, p. 241-266.

[6] *B. Tagiev, G. Niftiev, S. Abushov.* Recombination and trapping levels in GaS: Mn single crystals // Phys. Stat. Sol. (a), 1983, v. 78, No 2, p. k183-k187.

[7] *O.Z. Alekperov, M.Z. Zarbaliev.* Vliyanie vakanskiy seri na fotoprovodimost monosulfida qalliya v UF – oblasti spek // Neorq. Mat., 1998, t.34, №10, s.1163-1167.(In Russian).

[8] *A.N. Nadjaev*. Politipizm I polimorfizm v kristallax I v ix dvoynix analoqax. Dis. dok.-ra xim. nauk., 2009, 454 s.(In Russian).

[9] *D. Rao*. On the analysis of thermoluminescence glow pattern // Phys. Stat. Sol. (a), 1974, v. 22, No 1, p. 337-341.

[10] *Yu.A. Qoroxovatskiy, Q.A. Bordovskiy*. M.: Nauka, 1991, s. 244.(In Russian).

[11] *J. Mentel.* A new kind of calculation of thermoluminescence parameters // Phys. Stat. Sol. (a), 1992, v. 130, No 2, p. k169-k173.

[12] *F. Urbach.* Stimulation von ZnS-phosphoren mit temperature // Wien. Ber. II a, 1930, No 139, p. 353-360.

Received: 12.11.2012

EFFECT OF DESMOSTEROL ON DPPC MODEL MEMBRANE: an FTIR STUDY

IPEK SAHIN[1], CISEM ALTUNAYAR[1] AND NADIDE KAZANCI[1]

[1]Department of Physics, Faculty of Science, Ege University, İzmir, 35100, Turkey
E-mail: nadide.kazanci@gmail.com, Tel.: +90 (232) 3112301, Fax: +90 (232) 3881036

In this work, the effect of desmosterol on model membrane consisting of DPPC phospholipid was investigated for the first time, by using FTIR spectroscopy technique by being analysed C-H stretching, C=O stretching, PO_2^- antisymmetric stretching modes. The result of FTIR studies shows that the addition of desmosterol at low concentration (3 mol %) into pure DPPC liposomes increases the order and decreases the dynamics in the gel phase, whereas high concentration of desmosterol (30 mol %) decreases the order and increases the dynamics of membrane in the gel phase. In the liquid crystalline phase, low desmosterol concentration (3 mol %) has a negligible effect in the order and causes a decrease in the dynamics of DPPC membrane, while high desmosterol concentration (30 mol %) induces an increase in the order and the dynamics of DPPC membrane. When frequency values of C=O stretching and PO_2^- antisymmetric stretching band are investigated, we observe that these frequency values decrease with the addition of desmosterol concentrations. This result indicates hydrogen bonding in between the hydroxyl group of desmosterol and carbonyl group and head groups of phospholipids.

Keywords: Desmosterol, Dipalmitoyl phosphatidylcholine (DPPC), Membrane, Fourier Transform Infrared (FTIR) Spectroscopy.
PACS: 61.10.-i, 87.80.-y, 64.75.+g

1. INTRODUCTION

Desmosterol, a primary biosynthetic precursor of cholesterol in the Bloch pathway of cholesterol biosynthesis, varys from cholesterol merely in a double bond at the 24th position in the flexible alkyl side chain [1]. The chemical structure of it is shown Fig. 1.

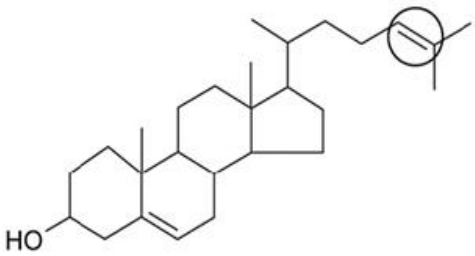

Fig. 1. Chemical structure of desmosterol [1].

Desmosterol consists of only trace quantities in most tissues, however it is an important component in spermatozoa, developing brain and accumulates during myotonia [2]. Desmosterol has also medical interest because there are various scarce and severe disorders including desmosterolosis, a rare humane disorder induced by the body's inability to transform desmosterol into cholesterol [3]. Desmosterolosis is an autosomal, recessive congenital disease and is characterized by multiple anomalies. It is induced by mutations in 3β-hydroxy-steroid-Δ24-reductase (DHCR24), an enzyme required in the final step of the Bloch pathway of cholesterol biosynthesis. Desmosterolosis is clinically diagnosed with increased levels of desmosterol and reduced levels of cholesterol in plasma, cells and tissues. This disease is characterized by different facial anomalies, underdeveloped genital organs and abnormalities in brain development and function, causing serious developmental and neurological dysfunctions [1]. Eventhough desmosterol is of many same functions as cholesterol in the structure, dynamics and other biophysical functions of membrane, only little is known about the physicochemical properties of desmosterol including bilayer membranes [4,5]. In the literature, the studies on the interaction of desmosterol with membranes at molecular level [5,6] are very limited. These NMR, EPR, fluorescence spectroscopy, steady-state DPH fluorescence polarization studies used 1-palmitoyl-d_{31}-2-oleoyl-*sn*-glycero-3 phosphocholine (POPC-d_{31}), spin-labeled lipids 1-palmitoyl-2-(5-doxylstearoyl)-*sn*-glycero-3 phosphocholine (C5-SL-PC) and 1-palmitoyl-2-(16-doxylstearoyl)-*sn*-glycero-3 phosphocholine (C16-SL-PC), 1-palmitoyl-2-oleoyl- *sn*-glycero -3-phosphocholine (POPC), sphingomyelin (SPM), dioleylphosphatidylcholine (DOPC) and dipalmitoylphosphatidylcholine (DPPC) model membranes in the form of multilamellar vesicles (MLV) and large unilamellar vesicles (LUV). They mainly reported the effect of desmosterol on membrane order, which were not always consistent with each other. In order to better understand the effect of desmosterol on biological membranes at molecular level, it is important to study its interaction with membrane components and specifically with lipids. The lipid having the largest body of experimental structural data is dipalmitoyl phosphatidylcholine (DPPC) (Fig. 2), which composes of two saturated 16-carbon fatty acid chains connected by a glycerol backbone with a zwitterionic headgroup [7].

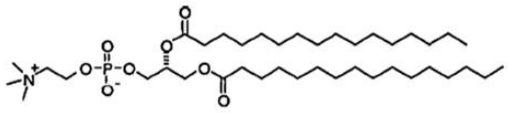

Fig. 2. Chemical structure of DPPC [8].

Various experimental and computational studies have focused on model systems consisting of a single lipid like DPPC. These studies of simplified systems have been essential and have enhanced our understanding of the properties of biological membranes [9].

In the present study, we have investigated in detail the interaction of desmosterol with dipalmitoyl phosphatidylcholine (DPPC) model membrane using Fourier transform infrared (FTIR) spectroscopy. FTIR spectroscopy was used to monitor subtle changes in the

structure and function of the lipid assemblies by analyzing the frequency, the bandwidth changes of the different vibrational modes representing the acyl chains, interfacial region and the head group region of lipid molecules. For this reason, in addition to membrane dynamics, this techniques allowed us to obtain structural properties of binary mixtures of desmosterol and phospholipid membranes such as lipid phase behaviour, membrane acyl chain order, hydration state of head group and glycerol backbone region [10].

2. MATERIALS AND METHODS

Desmosterol and DPPC were purchased from Sigma (St. Louis, MO, USA) and used without further purification.

For the infrared measurements, pure phospholipid MLVs were prepared according to the procedure, reported by Severcan et al. [10]. To prepare DPPC MLVs, 5 mg of phospholipid was dissolved in chloroform in a round-bottomed flask. A dried lipid film was obtained by evaporating it with a nitrogen flux and then pumping it for at least 2 h under vacuum by using Heto spin vac. The film was hydrated by adding 25 µl of 10 mM phosphate buffer, pH 7.4. Liposomes were formed by vortexing the mixture at a temperature above the gel-to-fluid phase transition for 20 min. In order to prepare desmosterol containing liposomes, appropriate amount of desmosterol was taken from the stock solution, in which desmosterol was dissolved in chloroform, and put in a round-bottomed flask. The excess chloroform was evaporated by nitrogen stream and then 5 mg of DPPC was added and dissolved in the same round-bottomed flask by chloroform. The same procedure for the preparation of pure DPPC liposomes was then followed. Sample suspensions of 20 µl were placed between CaF_2 windows with the cell thickness of 12 µm. Infrared spectra were obtained using a Spectrum 1 Perkin-Elmer FTIR spectrometer equipped with a DTGS detector. Interferograms were averaged for 50 scans at 2 cm^{-1} resolution. Temperature was regulated by a Graseby Specac digital temperature controller unit. The samples were incubated for 10 min at each temperature before data acquisition. Samples were scanned between 20 and 47 °C with 2 °C intervals, and between 50 and 70 °C with 5 °C intervals.

3. RESULTS

The infrared spectra of DPPC MLVs, both pure and containing different concentrations of desmosterol (3 mol% and 30 mol%), were investigated as a function of temperature. The C-H stretching modes at 2800-3000 cm^{-1}, C=O stretching mode at 1735 cm^{-1} and the PO_2^- antisymmetric stretching double bands at 1220-1240 cm^{-1} were considered. All experiments were repeated three times and similar trend was observed at each repeat.

Various kinds of information can be derived from these bands. Frequency shifts in different regions or changes in the widths of corresponding peaks can be used to extract information about various physicochemical processes taking place in the systems. For example, the frequencies of the CH_2 stretching bands of acyl chains depend on the degree of conformational disorder and hence the frequency values can be used to monitor the average trans/gauche isomerization in the systems. The shifts to higher wavenumbers correspond to an increase in number of gauche conformers. Furthermore the bandwidths of the CH_2 stretching bands give dynamic information about the system [10,11].

Fig. 3 shows the temperature dependence of the frequency of the CH_2 antisymmetric stretching bands of DPPC MLVs in the presence and absence of different concentrations of desmosterol. In the curve of DPPC MLVs, the frequency values at temperatures below 32 °C are characteristic of conformationally highly ordered acyl chains with a high content of trans isomers as found in solid hydrocarbons, whereas, the values at temperatures above 42 °C are characteristic of conformationally disordered acyl chains with a high content of gauche conformers as found in liquid hydrocarbons. The pretransition occurs around 35 °C [12]. The abrupt shift in the peak frequency of the CH_2 stretching modes of DPPC, which takes place during the main endothermic phase transition (~ 41°C), has been associated with the change from all trans to gauche conformers [12].

As seen from the figure, as the desmosterol concentration increases in the DPPC MLVs, the main phase transition temperature gradually shifts to lower values without affecting the general shape of the transition profile. In the gel phase, the addition of low concentration of desmosterol (3 mol%) into DPPC MLVs results in a decrease in the frequency, which indicates an increase in the number of trans conformers. The increase in the number of trans conformers implies an increase in the order of the bilayer [12-15]. Inclusion of high concentration of desmosterol (30 mol%) increases the frequency, which indicates an increase in the number of gauche conformers. The increase in the number of gauche conformers implies a decrease in the order of bilayer [15,16]. In the liquid crystalline phase, no significant change is observed in frequency values of the CH_2 stretching band with the addition of low concentration of desmosterol (3 mol%). This indicates that desmosterol has a negligible effect on the order of DPPC MLVs in the liquid crystalline phase. The incorporation of higher concentration of desmosterol molecules into the DPPC multibilayers induces a shift of the frequency to the lower values which implies an increase in the order of membrane.

Fig. 4 shows the temperature dependence of the bandwidth of the CH_2 antisymmetric stretching band of DPPC MLVs in the absence and presence of different desmosterol concentrations. Bandwidth was measured at 0.75x peak height position. The variation of the bandwidth gives information about the dynamics of the system. An increase in bandwidth is the indication of an increase in dynamics [12,16]. As seen from the figure, the bandwidth decreases both in the gel and the liquid crystalline phase with the addition of low concentration of desmosterol (%3 mol) into pure DPPC liposomes, indicating that low desmosterol concentration decreases the dynamics of the membrane in both phases. Inclusion of high concentration of desmosterol (30 mol%) increases the bandwidth, indicating that high desmosterol concentration desmosterol increases the dynamics of the membrane [13,15-18].

One of the most useful infrared band for probing the polar part of the membrane is that of band due to the ester group vibrations at the 1730 cm^{-1} (C=O stretching).

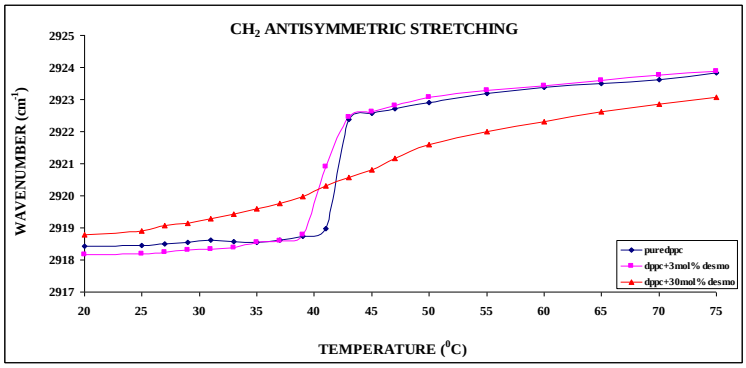

Fig. 3. Temperature dependent variation in the frequency of the CH_2 antisymmetric stretching modes of DPPC MLVs in the presence and absence of different concentrations of desmosterol.

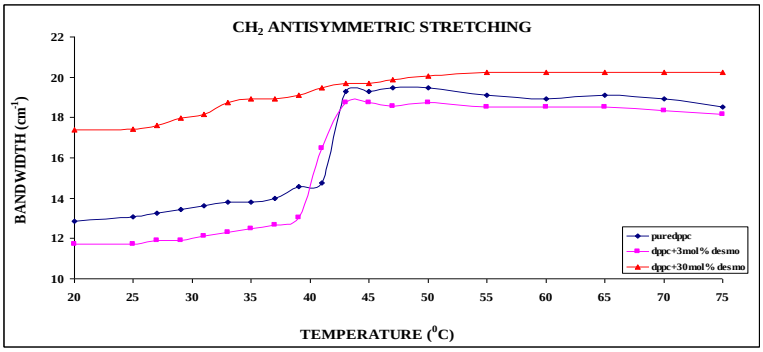

Fig. 4. Temperature dependence of the bandwidth of the CH_2 antisymmetric stretching modes of DPPC MLVs in the presence and absence of different concentrations of desmosterol.

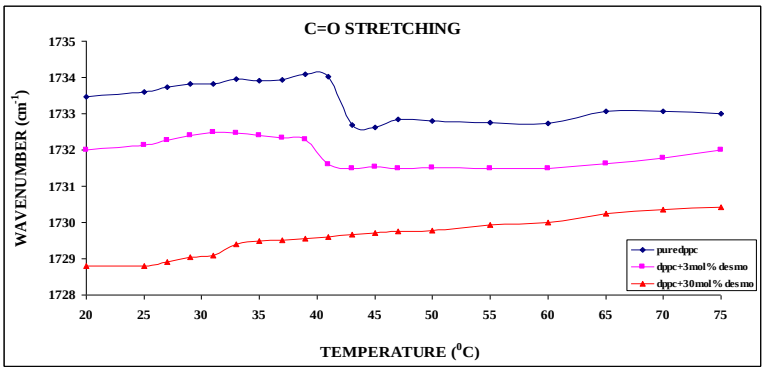

Fig. 5. Temperature dependence of the frequency of the C=O stretching mode of DPPC MLVs in the presence and absence of desmosterol.

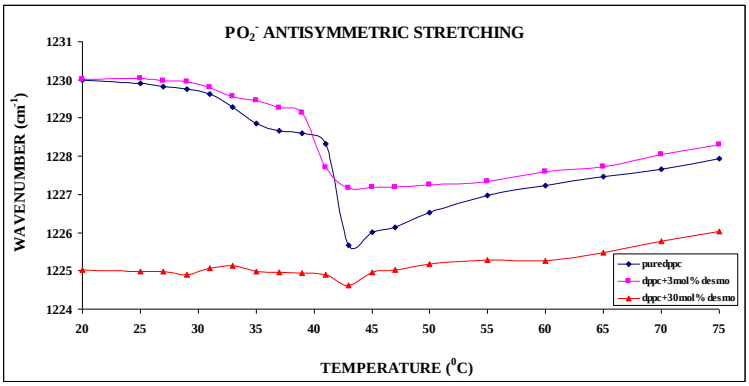

Fig. 6. The temperature dependence of the PO_2^- antisymmetric double bond stretching mode frequencies of DPPC liposomes in the presence and absence of desmosterol.

Temperature dependence of the frequency of the C=O stretching modes of DPPC multibilayers in the absence and presence desmosterol is shown in Fig. 5. As seen from the figure, a dramatic decrease in the frequency, in comparison to that of pure DPPC, is observed in the presence of desmosterol, both in the gel and liquid crystalline phase, which indicates that desmosterol increases the strength of hydrogen bonding around this functional group.

The other band for probing directly the head group of DPPC is the PO_2^- antisymmetric double stretching band, which is located at 1260 cm^{-1}. As seen from Fig. 6, the frequency of this band also shifts to lower values with the addition of high concentration of desmosterol (30 mol%) into DPPC MLVs, which indicates hydrogen bonding in between phosphate group of DPPC and desmosterol or water molecules [13]. The incorporation of lower concentration of desmosterol (3 mol%) into the DPPC multibilayers induces a shift of the frequency to the higher values, which shows that low desmosterol concentration causes dehydration in the head group of phospholipids.

4. DISCUSSION

The structure-function relations of sterols in biological membranes are quite wondered and are not still clearly understood. Furthermore, because of contradictory results in the literature, the effect of sterol structures on physical properties of membrane is not still obvious. The application of different physical techniques in sterol/lipid systems increases the diversity of the results obtained and it is also provided more detailed interpretations on the effects of the chemical structure of sterol on the structure and thermic phase features of membrane. The investigation of interactions in between sterols and neighbour phospholipid molecules is important in understanding of the features of sterols in biological membranes and of the roles of this type of interactions in many disease.

In the present study, we investigated for the first time the effect of desmosterol on the lipid phase transition, order and dynamics and hydration states of head group of zwitterionic DPPC MLVs as a function of temperature and desmosterol concentration by using FTIR spectroscopy technique. We examined the effect of desmosterol on hydrophilic part of membrane by analyzing C=O stretching band and PO_2^- antisymmetric stretching band and on hydrophobic part of membrane by analyzing C-H stretching region. We were particularly careful in distinguishing between structural parameters describing molecular order and motion parameters such as bandwidth describing molecular dynamics as suggested by others [19].

As a result of our FTIR studies, the addition of desmosterol into pure DPPC liposomes eliminates the pretransition and shifts the main transition to lower temperatures and then abolishes the main transition at high concentration of desmosterol. One of the structurally closest relatives of cholesterol in the Bloch pathway is its primary precursor desmosterol. The merely distinction between cholesterol and desmosterol is an extra double bond between carbon atoms 24 and 25 in the tail of desmosterol [6]. It is also well known from the literature that in the liquid-crystalline phase, the addition of cholesterol reduces the area per molecule in lipid monolayers, increases the orientational order of lipid acyl chains in lipid bilayers, and decreases the passive permeability of lipid bilayers. The opposite effects are observed when cholesterol is added to lipid systems in the gel phase [20]. In the absence of cholesterol, saturated lipids, such as DPPC, generally display a number of different thermodynamic phase transitions. The main phase transition takes the lipid bilayer from the gel to the liquid-crystalline phase, with increasing temperature [20]. At temperatures below the phospholipid phase transition temperature, cholesterol molecules interfere with the tight packing of the phospholipids molecules that is required for gel formation, giving rise to the fluidizing effect. An opposite effect is observed at temperatures above the phase transition temperature of the phospholipid. Thus, cholesterol has a dual effect of decreasing membrane fluidity at high temperatures and doing the opposite at low temperatures [21]. In our study, we observed the effect of desmosterol on model membranes that is similar with cholesterol mentioned in the literature. While the addition of 30 mol% desmosterol into DPPC liposomes decreases the order of DPPC membrane in gel phase, it increases the membrane order in the liquid crystalline phase. Serfis et al., which is in agreement with our study [22], investigated the interactions of cholesterol, desmosterol and 7-dehydrocholesterol (7DHC) at different concentrations (10 mol%, 20 mol% and 30 mol%) with egg PC monolayers at 37 ℃ by using Langmuir monolayer technique and found that the addition of desmosterol into PC monolayers causes an alteration in the molecular area and also at high desmosterol concentrations the alteration in the molecular area is higher. This alteration in the molecular area giving rise to desmosterol revealed that desmosterol induces a condensation effect into PC monolayers. These results showed that egg PC monolayers in the liquid crystalline phase at 37 ℃ packed more tightly with the effect of desmosterol. An another study examined the effects of cholesterol, desmosterol and 7DHC on saturated DPPC and unsaturated DOPC lipids in the liquid crystalline phase at around 50 ℃ by atomic scala simulation study showed that every three sterols lead to membrane condensation. The condensation effect which is defined as decrease of area per molecule and increase of hydrophobic thickness and chain order is closely related to the effect of the order [23,3]. Besides, it was stated that the reduction in surface area per molecule is associated with the enhancement of the membrane thickness. For this reason, the decreasing effects of these three sterols on the surface area per molecule of saturated DPPC lipids are the same with the increasing effects of them on the membrane thickness [24]. In a study comparing the effects of cholesterol, desmosterol and lanosterol on mobility of POPC LUV membranes labelled with PC analogs by using EPR spectroscopy, it was observed that these lipids

increase the order in the presence of 30 mol% sterol in the liquid crystalline phase at 30 ℃. In the same study, by using fluorescence spectroscopy, with the addition of 10 mol% and 30 mol% cholesterol and desmosterol into POPC LUV membrane at 30 ℃, it was indicated that emission peaks of these two sterols, in comparison to pure POPC LUV emission peak, are more intense, so both cholesterol and desmosterol increase the membrane order similarly. When sphingomyelin (SPM) lipid is used instead of POPC in the same study, it was revealed that these sterols increase the chain order of SPM profoundly in comparison to POPC LUV [5]. Another study investigated the effects of cholesterol and its two precursors; desmosterol and 7DHC on POPC LUVs and DPPC LUVs at different concentrations (0-50 mol%) by using steady state fluorescence measurements. It was observed that the anisotropy values decreases with the addition of increasing cholesterol concentrations (to 50 mol%) into DPPC membrane at room temperature (23 ℃). The reduction of these values interpreted that cholesterol makes DPPC membrane more disordered in the gel phase. Furthermore, with the addition of increasing desmosterol concentrations into DPPC membrane at the same temperature, it was observed that the anisotropy values decreases. The reduction of these values indicated that desmosterol decreases the order of DPPC membrane in gel phase. In the same study, POPC membrane is used instead of DPPC membrane at the same temperature (23℃) and the same sterol concentrations. Phase transition of POPC from the gel phase to the liquid crystalline phase is at -2 ℃, so POPC is in the liquid crystalline phase at 23 ℃. With the addition of high concentrations of desmosterol into POPC membrane, it was found that the anisotropy values increases substantially. The enhancement of these values inferred that increasing concentrations of desmosterol make POPC membrane more ordered in the liquid crystalline phase at 23 ℃ [25]. All these studies are in agreement with our study.

There is a limited number of studies in the literature about the effect of desmosterol on membrane dynamics and fluidity. Benesch et al., which is in agreement with our study [26], investigated the effect of lathosterol which is the penultimate intermediate in the biosynthesis of cholesterol in the Kandutsch-Russell pathway, differing Bloch pathway which desmosterol is formed, on DPPC and DPPC-d_{62} model membranes by using FTIR spectroscopy and found that values of absorption bandwidth of C−H stretching region (3000-2800 cm^{-1}) of DPPC model membranes consisting of 30 mol% lathosterol increase with the enhancement in temperature and so the fluidity of lipid hydrocarbon chain increases. Moreover, it was observed that with the addition of 30 mol% lathosterol into pure DPPC-d_{62} membrane, the bandwidth values of CD_2 symmetric stretching band, in comparison to pure DPPC-d_{62} membrane, are in higher values. This situation showed that lathosterol which is one of the precursors of cholesterol like desmosterol, increases the fluidity of hydrocarbon chains of DPPC-d_{62} membrane in gel phase. In another study which is examined the changes in CH_2 symmetric stretching bandwidth of DPPC bilayers including ergosterol by using FTIR spectroscopy and depending on the temperature, it was observed that at the temperatures below the main phase transition, namely in the gel phase, DPPC membranes containing 30 mol% ergosterol increase the hydrocarbon chain mobility, in comparison to pure DPPC membrane [27]. The enhancement in the width of absorption bands represents that lipid hydrocarbon chain mobility increases [26].

In the present work, we indicated the hydrophobic interaction in between DPPC molecule and desmosterol. Both methyl groups and long hydrocarbon chains of DPPC and also steran ring of desmosterol may cause a strong enviroment for the hydrophobic interaction. DPPC and desmosterol molecules can be also connected to each other with the van der Waals interactions in addition to hydrophobic interactions. The interactions of hydrocarbon chain and neighboring molecules are determined primarily by van der Waals forces, which have non-directional attractive and directional repulsive components and by dispersion forces which together determine the lateral forces applied along the length of neighboring lipid molecules in the bilayer [28]. Van der Waals interactions in the hydrophobic area are non-polar interactions and contribute to the strength of hydrophobic effect [24,3] and are very important for the structure and interaction of biological molecules [29].

Investigation of the interfacial region and polar head group region of DPPC membrane in our study revealed that the hydroxyl group of desmosterol makes strong hydrogen bonding with carbonyl group and head groups of phospholipids. DPPC is a phospholipid which has high quality to make hydrogen bonding with both phosphate group (PO_2^-) and ester groups (C = O) and tertiary amine regions in its structure. Desmosterol is capable of making hydrogen bonding by means of hydroxyl group (OH) in steran ring. Róg et al., which is in agreement with our study [24], examined the effects of cholesterol, desmosterol and 7DHC on saturated DPPC and unsaturated DOPC lipids in the liquid crystalline phase at about 50 ℃ by atomic scala simulation study and found that the orientation of these three sterols is different, but all of them are similarly found at the membrane water interface and hydroxyl (OH) groups of different sterols have the same distance from phosphate oxygen atoms of DPPC. Moreover, according to the result of the interaction of hydroxyl groups of sterols with the head groups of PC and water molecules at atomic level, it was also found that hydroxyl groups of all three sterols give rise to hydrogen bonding with water and PC oxygen atoms. As a result of this, it was stated that the hydrogen bonding shape of all three sterols is the same and they make hydrogen bonding with ester group of *sn-2* chain of DPPC and DOPC. Furthermore, it was observed that the interaction shapes of hydroxyl groups of all three sterols are similar for both DPPC and DOPC membranes. In another study, it was also found that there is an interaction in between OH group of cholesterol and hydrophilic polar head group of lecithin and that hydrogen bonding occurs [30]. Similar results have been observed in some other studies [31,32]. In the study investigated C=O stretching vibrations of ester carbonyl groups of DPPC in polar-apolar interfacial region of bilayer by using FTIR spectroscopy, Benesch et al. found that the shape of ester

carbonyl stretching band of DPPC membrane consisting 30 mol % lathosterol is different in comparison to that of pure DPPC indicating the increasing existence of hydrogen bounded ester carbonyl groups of DPPC. Besides, they also stated increasing hydrogen bonding degree in between hydroxyl group of lathosterol and water [26]. In another study examined changes of FTIR spectrums of DPPC bilayers containing 30 mol% ergosterol depending on temperature, it was specified that the changes in the shape of C=O stretching absorption band reflect the variations in hydration or in the number of hydrogen bonded ester carbonyl groups in the interfacial region. In addition, it was observed that the shape of C=O stretching band of DPPC bilayers containing ergosterol is different from the shape of C=O stretching band of pure DPPC membrane. This difference was interpreted as increasing population of hydrogen bonded ester carbonyl group in enviroment [27]. In the study of the same group used 30 mol% epicholesterol as a sterol for this time, it was found that epicholesterol increases the hydrogen bonding degree of DPPC carbonyl groups indicating that this enhancement caused by epicholesterol arises from hydrogen bonding in between C3-hydroxyl group of epicholesterol molecule and ester carbonyl group of DPPC and also from the increase of the degree of water penetration in glycerol backbone region of DPPC bilayer [33].

5. CONCLUSION

In the present study, we have investigated for the first time the interaction of desmosterol with a zwitterionic lipid, dipalmitoylphosphatidylcholine (DPPC) by means of lipid order and dynamics, phase behavior and hydration as a function of temperature and at low and high desmosterol concentration by using FTIR spectroscopy technique. Our results revealed that low concentration of desmosterol (3 mol%) decreases acyl chain flexibility, i.e., increases order of DPPC membrane, and the dynamics in gel phase and has a negligible effect in order and decreases the dynamics in liquid crystalline phase and that the inclusion of high desmosterol concentration (30 mol%) increases the conformational disorder and the dynamics in gel phase and decreases the number of gauche conformers (ordering) and increases the dynamics in liquid crystalline phase. Furthermore, we also showed that desmosterol interacts strongly with head group of zwitterionic membranes and that it makes strong hydrogen bonding with the carbonyl and phosphate groups of these membranes.

ACKNOWLEDGEMENTS

This work was supported by Ege University Research Fund 2011 FEN 046. We would like to thank Prof. Dr. Feride Severcan of the Department of Biological Sciences at Middle East Technical University for the generous use of her laboratory.

[1] *P. Singh, R. Saxena, Y.D. Paila, Md. Jafurulla and A. Chattopadhyay*, ‘‘Differential effects of cholesterol and desmosterol on the ligand binding function of the hippocampal serotonin$_{1A}$ receptor: Implications in desmosterolosis’’ Biochimica et Biophysica Acta, 1788 (2009) 2169-2173.

[2] *R.W. Evans, M.A. Williams and J.Tinoco*, ‘‘Surface areas of 1-palmitoyl phosphatidylcholines and their interactions with cholesterol’’ Biochem. J., 245 (1987) 455-462.

[3] *T. Róg, M. Pasenkiewicz-Gierula, I. Vattulainen and M. Karttunen*, ‘‘Ordering effects of cholesterol and its analogues’’ Biochimica et Biophysica Acta, 1788 (2009) 97–121.

[4] *W. Chen, B. Su, H. Xing, Y. Yang and Q. Ren*, ‘‘Solubilities of cholesterol and desmosterol in binary solvent mixtures of n-hexane + ethanol’’ Fluid Phase Equilibria, 287 (2009) 1–6.

[5] *D. Huster, H. A.Scheidt, K. Arnold, A. Herrmann, and P. Müller*, ‘‘Desmosterol may replace cholesterol in lipid membranes’’ Biophysical Journal, 88 (2005)1838-1844.

[6] *S. Vainio, M. Jansen, M. Koivusalo, T. Róg, M. Karttunen, I. Vattulainen and E. Ikonen*, ‘‘Significance of Sterol Structural Specificity: Desmosterol cannot replace cholesterol in lipid rafts’’ The Journal Of Biological Chemistry, 281 (2006) 348-355.

[7] *S. E. Feller*, ‘‘Computer simulation of a DPPC phospholipid bilayer: structural changes as a function of molecular surface area’’ Langmuir, 13 (1997) 6555-6561.

[8] *A. Hasanovic, S. Hoeller and C. Valenta*, ‘‘Analysis of skin penetration of phytosphingosine by fluorescence detection and influence of the thermotropic behaviour of DPPC liposomes’’ International Journal of Pharmaceutics, 383 (2010) 14-17.

[9] *C. Hofsäß, E. Lindahl and O. Edholm,* ‘‘Molecular dynamics simulations of phospholipid bilayers with cholesterol’’ Biophysical Journal, 84 (2003) 2192-2206.

[10] *F. Severcan, I. Sahin and N. Kazancı,* ‘‘Melatonin strongly interacts with zwitterionic model membranes—evidence from Fourier transform infrared spectroscopy and differential scanning calorimetry’’ Biochimica et Biophysica Acta, 1668 (2005) 215–222.

[11] *F. Korkmaz and F. Severcan*, ‘‘Effect of progesterone on DPPC membrane: Evidence for lateral phase separation and inverse action in lipid dynamics’’ ABB, 440 (2005) 141–147.

[12] *H. L. Casal and H. H. Mantsch*, ‘‘Polymorphic phase behaviour of phospholipid membranes studied by infrared spectroscopy’’ Biochim. Biophys. Acta, 779 (1984) 381.

[13] *N. Toyran and F. Severcan*, ‘‘Competitive effect of Vitamin D2 and Ca^{2+} on phospholipid model membranes: a FTIR study’’ Chem. Phys. Lipids, 123 (2003) 165–176.

[14] *F. Severcan*, ‘‘Vitamin E decreases the order of the phospholipid model membranes in the gel phase: an FTIR study’’ Biosci. Rep., 17 (1997) 231–235.

[15] *J. Villalain, F. J. Arranda and J. C. Gomez-Fernandez,* ‘‘Calorimetric and infrared spectroscopic studies of the interaction of a-tocopherol and a-tocopheryl acetate with phospholipid vesicles’’ Eur. J. Biochem., 158 (1986) 141–147.

[16] *N. Kazancı, N. Toyran, P. I. Haris and F. Severcan,* ‘‘Vitamin D2 at high and low concentrations exert opposing effects on molecular order and dynamics of dipalmitoyl phosphatidylcholine membranes’’ Spectroscopy, 15 (2001) 47–55.

[17] *H. L. Casal, D. G. Cameron, I. C. P. Smith and H.H. Mantsch,* ‘‘Acholeplasma laidlawii membranes—Fourier-transform infrared study of the influence of protein on lipid organization and dynamics’’ Biochemistry, 19, (1980) 444–451.

[18] *F. Lopez-Garcia, J. Villalain and J. C. Gomez-Fernandez,* ‘‘Infrared spectroscopic studies of the interaction of diacylglycerols with phosphatidylserine in the presence of calcium’’ Biochim. Biophys. Acta, 1169 (1993) 264–272.

[19] *G. V. Ginkel, H. V. Langen and Y. K. Levine,* ‘‘The membrane fluidity concept revisited by polarized fluorescence spectroscopy on different model membranes containing unsaturated lipids and sterols’’ Biochimie, 71 (1989) 23–32.

[20] *M. J. L. de Lange, M. Bonn and M. Müller,* ‘‘Direct measurement of phase coexistence in DPPC/cholesterol vesicles using Raman spectroscopy’’ Chemistry and Physics of Lipids, 146 (2007) 76–84.

[21] *K. Gong, S.-S. Feng, M. L. Go and P. H. Soew,* ‘‘Effects of pH on the stability and compressibility of DPPC/cholesterol monolayers at the air–water interface’’ Colloids and Surfaces A: Physicochemical and Engineering Aspects, 207 (2002) 113–125.

[22] A.*B. Serfis, S. Brancato and S.J. Fliesler,* ‘‘Comparative behavior of sterols in phosphatidylcholine-sterol monolayer films’’ Biochimica et Biophysica Acta, 1511 (2001) 341-348.

[23] *A. Filippov, G. Orädd, and G. Lindblom,* ‘‘Effect of NaCl and CaCl2 on the lateral diffusion of zwitterionic and anionic lipids in bilayers’’ Chemistry and Physics of Lipids, 159 (2009) 81-87.

[24] *T. Róg, I. Vattulainen, M. Jansen, E. Ikonen, and M. Karttunen,* ‘‘Comparison of cholesterol and its direct precursors along the biosynthetic pathway: effects of cholesterol, desmosterol and 7-dehydrocholesterol on saturated and unsaturated lipid bilayers’’ The Journal Of Chemical Physics, 129 (2008)154508.

[25] *S. Shrivastava, Y. D. Paila, A. Dutta and A. Chattopadhyay,* ‘‘Differential effects of cholesterol and its immediate biosynthetic precursors on membrane organization’’ Biochemistry, 47 (2008) 5668–5677.

[26] *M. G. K. Benesch, D. A.Mannock, R. N. A. H.* Lewis and R.N. McElhaney, ‘‘A calorimetric and spectroscopic comparison of the effects of lathosterol and cholesterol on the thermotropic phase behavior and organization of dipalmitoylphosphatidylcholine bilayer membranes’’ Biochemistry, 50 (2011) 9982-9997.

[27] *D. A. Mannock, R. N. A. H Lewis and R. N. McElhaney,* ‘‘A calorimetric and spectroscopic comparison of the effects of ergosterol and cholesterol on the thermotropic phase behavior and organization of dipalmitoylphosphatidylcholine bilayer membranes’’ Biochimica et Biophysica Acta, 1798 (2010) 376-388.

[28] *D. A. Mannock, R. N. A. H. Lewis, T. P. W. McMullen and R. N. McElhaney,* ‘‘The effect of variations in phospholipid and sterol structure on the nature of lipid–sterol interactions in lipid bilayer model membranes’’ Chemistry and Physics of Lipids, 163 (2010) 403–448.

[29] *A. V. Finkelstein,* ‘‘Average and extreme multi-atom Van der Waals interactions: Strong coupling of multi-atom Van der Waals interactions with covalent bonding’’ Chemistry Central Journal, 1 (2007) 21.

[30] *D. Bongiorno, L. Ceraulo, M. Ferrugia, F. Filizzola, A. Ruggirello, and V. T. Liveri,* ‘‘Localization and interactions of melatonin in dry cholesterol/lecithin mixed reversed micelles used as cell membrane models’’ J Pineal Res., 38 (2005) 292-298.

[31] *C. Gliss, O. Randel, H. Casalta, E. Sackmann, R. Zorn, and T. Bayerl,* ‘‘Anisotropic motion of cholesterol in oriented DPPC bilayers studied by quasielastic neutron scattering: the liquid-ordered phase’’ Biophysical Journal, 77 (1999) 331-340.

[32] *A.M. Smondyrev and M.L. Berkowitz,* ‘‘Molecular dynamics simulation of dipalmitoylphosphatidylcholine membrane with cholesterol sulfate’’ Biophysical Journal, 78 (2000) 1672-1680.

[33] *D.A. Mannock,M.Y.T. Lee,R.N.A.H. Lewis and R.N. McElhaney,* ‘‘Comparative calorimetric and spectroscopic studies of the effects of cholesterol and epicholesterol on the thermotropic phase behaviour of dipalmitoylphosphatidylcholine bilayer membranes’’ Biochimica et Biophysica Acta, 1778 (2008) 2191-2202.

Received: 02.11.2012

DEPOSITION OF Al-DOPED ZnO FILMS BY DC MAGNETRON SPUTTERING: EFFECTS OF DAMP EXPOSURE AND ANNEALING ON THEIR PROPERTIES

E. P. ZARETSKAYA[1], I.A. VICTOROV[1], O.V. GONCHAROVA [2], T. R. LEONOVA [3], M. GARTNER[4], N.N. MURSAKULOV[5], N.N. ABDULZADE[5], Ch.E. SABZALIYEVA[5]

[1] State Scientific and Production Association "Scientific-Practical Materials Research Centre of the National Academyof Sciences of Belarus, P. Brovka str. 19, 220072 Minsk, Belarus, +375-17-2841249, fax: +375-17-2840888, email:ezaret@ifttp.bas-net.by

[2] Institute of Molecular and Atomic Physics, National Academy of Sciences of Belarus,Independence Avenue 70, 220072 Minsk, Belarus

[3] B.I. Stepanov Institute of Physics National Academy of Sciences of Belarus, Logoiski trakt 22, 220090 Minsk, Belarus,

[4] Institute of Physical Chemistry, Romanian Academy, Spl. Independence 202, 060021 Bucharest, Romania

[5]Institute of Physics, National Academy of Azerbaijan, H. Cavid ave., 33, Baky, Az-1143,email: nmursakulov@physics.ab.az

High-quality Al-doped zinc oxide (AZO) thin films have been deposited on glass substrates by modified d.c. magnetron sputtering at room temperature for thin film solar cell applications. Effect of air annealing and damp exposure on the electrical and optical properties of AZO films have been investigated.

It was found the electrical resistivity of the films increases by two order of magnitude with the annealing temperature increase up to 250–300 °C and by three order of magnitude under multiple damp exposure. The transmittance and optical absorption of as-grown and treated AZO films are also investigated. The relationship between optical properties changes and the observations of the resistivity increase by damp heating is discussed.. It is suggested that grain boundaries modification has more close relation with both the resistivity increase and blue-wavelength shift of absorption edge.

Keywords: solar cells; ZnO:Al; sputtering, thin films; damp heat stability
PACS: 42.70.Km; 68.35.Dv; 68.60.Dv; 73.61.Ga; 78.66.Hf; 81.15.Cd

1. INTRODUCTION

ZnO (zinc oxide) is a wide-gap semiconductor with a room temperature direct band gap ($E_g \geq 3{,}4$ eV) and a large exciton binding energy of about 60 meV, which is a prerequisite for realization of efficient and stable optoelectronic systems. ZnO show a high optical transparency in the visible range and provides high shielding of the UV and IR regions which makes this a very attractive material for optoelectronic applications such as plasma displays, liquid crystal displays, transparent electrodes for solar cells, infrared (IR) windows and other optoelectronic devices. ZnO has a great advantage over indium transparent oxide (ITO) due to combination of its excellent electro-optical properties with long-term environmental stability, low costs and non-toxicity.

Magnetron sputtered undoped and Al-doped ZnO thin films are employed as front conducting contacts for silicon or Cu(In,Ga)Se_2 (CIGS) based thin-film solar cells [1–4]. Well-known requirements for front contacts are high transparency in the visible and near-UV regions as well as high conductivity. Among the ZnO film techniques such as laser deposition, chemical vapor deposition, atomic layer deposition, molecular beam epitaxy, most commonly used radio-frequency (RF) magnetron sputtering has some advantages due to its simple set-up, high deposition rate and low deposition temperatures and small cost of the films production [5–9]. As-grown ZnO films have *n*-type conductivity caused by native point defects [9,10]. In particular, oxygen vacancies and zinc interstitials are often mentioned as sources of *n*-type conductivity in ZnO, but the role of bulk defined or surface defects in formation of optical and electrical properties of ZnO films is still not well known [2, 9–12]. The conductivity of the films can be changed significantly by the deposition and post-deposition conditions and be improved by doping with atoms of higher valence than Zn, such as Al, In and Ga [6, 11].

The main parameter determining the reliability of solar cells and modules is the stability properties of the constituent components. While some studies of the influence of humidity and heating on the electrical properties of Cu(In,Ga)Se_2-based solar cell and modules have been performed [13–15], to our knowledge the above mentioned effects in the case of AZO films are not well understood [6, 11]. In this paper we have investigated the changes in electrical and optical properties of reactive magnetron sputtered AZO films depending on post-growth annealing in air and damp heat treatment.

2. EXPERIMENT

The Al-doped ZnO-coatings with different thicknesses in the range from 0.1 to 1.2 μm were deposited on glass substrates by DC (= direct current) planar magnetron sputtering. The special two-component

planar target, 114 mm in diameter and 10 mm thickness was designed in such a way that the content of Zn and Al (a purity of zink 99.99 % and aluminum 99.999 %) in it can widely varied. The Zn/Al ratio in the deposited film was set by the ratio of sputtering surface areas of Zn and Al in the target with consideration their sputtering coefficients.

In order to minimize the plasma bombardment effect on the substrates, a low RF power of 60 W was applied to each deposition. The deposition of the AZO films was carried out with the optimum conditions for the used system: an atmosphere of mixture of high-purity Ar (80 %) and O_2 (20 %) gas and a working deposition pressure of 1.0–1.3 Pa.

The distance between the substrate and the target was 45 mm and the DC power was maintained constant at 200 W. The growth rate for this deposition conditions is 30 nm/min. The substrate temperature on the anode was preheated to RT and during the deposition process it was heated up to 150 °C due to the ion bombardment of the substrate.

Crystal structure of the materials was studied by X-ray diffraction (XRD) using a Siemens D-5000 diffractometer (having CuK_α λ = 1.5418 Å radiation and a Ni filter) operated at 30 kV and 20 mA. SEM, AFM, spectroscopic ellipsometry and optical spectroscopy measurements were carried out to establish correlations between electrical, structural and optical properties of the films. Optical transmittance (*T*) and reflectance of samples were measured with a *Cary 500 Scan* double beam spectrophotometer in the spectral range 190–3300 nm.

Electrical resistivity ρ was determined from Hall effect measurements using the Van der Pauw method.

3. RESULTS AND DISCUSSION

3.1. Structural and morphological properties

The XRD spectra of as deposited AZO films show only (002) and (004) diffraction peaks at 2θ = 34,34° and 2θ = 72,41°, respectively with very good agreement with JCPDS data (card № 80-0074) for normally pure ZnO of hexagonal wurtzite type structure (Fig. 1). The strongest peak for AZO film was from the (002) plane, indicating that the layer have preferred orientation towards to [002] direction with a c-axis perpendicular to the substrates. No peaks from foreign phases were detected in XRD spectra of AZO films.

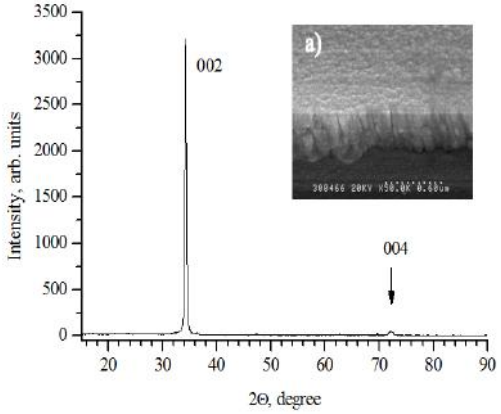

Fig.1. XRD pattern of AZO film.

All ZnO films, prepared by the described method, have the pinholes- and micro cracks free microstructure consisting of densely packed crystalline columns. Coherent ordering of the growth direction of crystalline columns for AZO films indicates on the high crystallinity of the grown films (Fig. 1, insert a)).

The atomic force microscopy (AFM) images were recorded in non-contact mode using a Park XE-100 (2010) equipment equipped with CONTSCR silicon tips (less than 10 nm at the apex).We used the horizontal line by line flattening as planarization method line by line flattening as planarization.

The AFM scans were taken over the area of 10×10 μm^2 and 2×2 μm^2. We used the horizontal method. Statistical parameters (e.g. root-mean-squared and average roughness) were evaluated for all images, at both large (10×10 μm^2) and low (2×2 μm^2) scale of measurements. It shows that the roughness increased sequentially on the AZO films from 21 to 64nm with increasing Al content in the film.

Fig. 2 presents AFM topography of the AZO film (Al content 4.73 at.%) with typical protruding grains, due to the columnar growth of the films (as generally observed on ZnO-based films), having diameters in the range of 60-100 nm .

3.2. Electrical and optical properties

Prepared films show RT resistivities in a broad range (0.0013–19 Ω cm) (Table 1, column RT), whicture of the substrate [9, 16]. Samples with the same h vary by thickness, deposition time and result temperaphysical properties, used in this study for detailed investigation of the treatments effect, were prepared by separation into four parts defined AZO film (Table 1, column RT, film 5). After the separation, the first part, sample 5-1, was annealed in air up to 300 °C. Annealing was performed in nominal steps of 50 °C with 1-hour duration for each cycle starting from 50 °C.

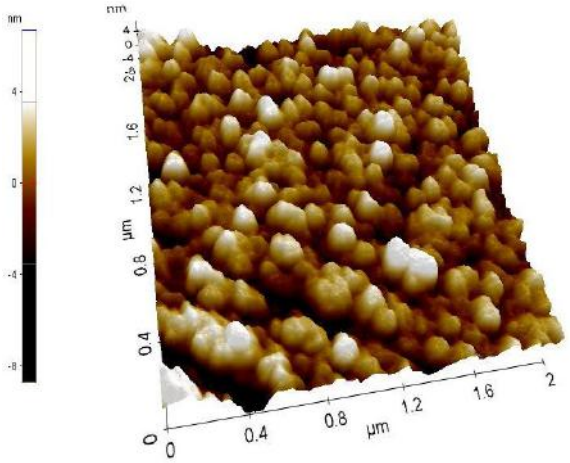

Fig. 2. AFM image of AZO film.

3.3 Results and discussion.

(The results related sample 5-1 is presented in Table 1, row 5, excepting "RT" cell.) The second part, sample 5-2, was exposed to 1-hour-cycles heating in a vapor of boiling water at 100 °C. The third part, sample 5-3, was

kept at RT in a saturated water vapor atmosphere and its resistivity was measured with 1-day cycle.

The last non-treated part of film 5 was used as reference marked here as sample 5-0.Selected AZO films with different thicknesses *h*, films 1–5, and samples with *h* = 180 nm were subjected to various sequential exposures and post-exposure RT measurements of electrical resistivity ρ, only selected data at defined temperatures and atmosphere are presented in Table 1, Figs. 3 and 4, and only the most important results will be discussed in the this paper.

Table 1 summarizes electrical resistivity determined from Hall Effect measurements for AZO films before (RT column) and after 1-hour annealing in air as well as Figs. 3, 4 are related to the results of damp exposure of the samples.

First, it was found that after the 1-hour annealing in the air at 50 °C the of AZO films electrical resistivity decreases and then gradually increases with the increase of the annealing temperature (see Table 1). Such behavior was observed for films 1, 2, 3 and 5 and can be explained by the diffusion and aggregation of the interstitial precipitates [9], resulting in more perfect film structure after annealing at 50 °C, as well as by oxidation of the samples at higher temperatures and longer annealing in air.

Second, Fig. 3 shows that during the sequential exposure of sample 5-2 to 1- hours heating at 100 °C in 100 % water vapor atmosphere there is notable increase of its resistivity. However, while after the first 5 cycles of such damp treatment the increase of resistivity is detectable on the level of two order of value, after 6–8 cycles it is stabilized near the value of $(2.5 \div 3.0)\ 10^{-1}$ Ω cm.

Table 1.

Dependency of the AZO resistivity on the annealing temperature

Selected AZO films	ρ, Ω cm						
	RT	50 °C	100 °C	150 °C	200 °C	250 °C	300 °C
1	$4.6\ 10^{-2}$	$2.7\ 10^{-2}$	$3.6\ 10^{-2}$	$1.5 \cdot 10^{-1}$	$8.7 \cdot 10^{-1}$	$8.1 \cdot 10^{0}$	-
2	$4.3\ 10^{-2}$	$1.9\ 10^{-2}$	$2.8\ 10^{-2}$	$1.4 \cdot 10^{-1}$	$2.5 \cdot 10^{-1}$	$4.3 \cdot 10^{0}$	-
3	$1.9\ 10^{1}$	$1.4\ 10^{1}$	$2.2\ 10^{1}$	$1.5 \cdot 10^{2}$	$3.1 \cdot 10^{3}$	-	-
5	$1.3\ 10^{-3}$	$1.1\ 10^{-2}$	$1.4 \cdot 10^{-3}$	$3.7 \cdot 10^{-3}$	$1.0 \cdot 10^{-2}$	$1.5 \cdot 10^{-1}$	$7.7\ 10^{-1}$

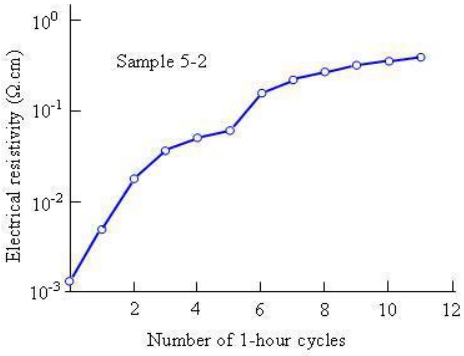

Fig.3. Resistivity of an AZO film exposed to 1-hour-cycles heating in a vapour of boiling water at 100 °5-2. There were 11 cycles.

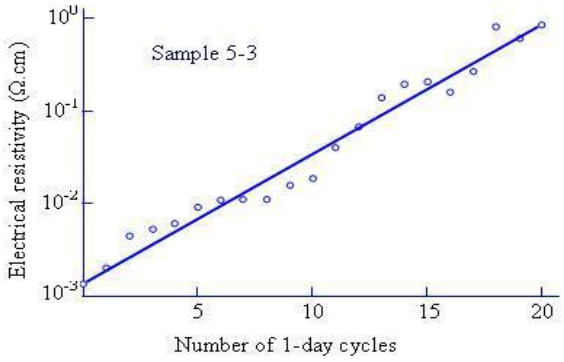

Fig.4. Resistivity of an AZO film exposed to 1-day-Cycles keeping in a vapour of a boiling water at RT, Sample 5-3.The cycles quantity was 20.

Third, Fig. 4 shows a steadily increase of electrical resistivity of sample 5-3 with the growth of the exposure time of the 100 % humidity at RT with 1 day cycle.

The analysis of resistivity of annealed and damp exposed samples presented in Table 1 and Figs. 1-2 shows that samples annealed at a higher temperature and at a higher level of humidity or damp exposed during more long time period possess higher electrical resistivity. This is established phenomenon in oxides and in AZO films in particular, where the large concentrations of oxygen excess favor the increase of film transmission at the expense of conductivity [2, 17]. Usually, oxygen is supplied to suppress generation of oxygen vacancies degrading electrical and the optical properties, such as carrier concentration and mobility. However, oxygen also generates formation of Al-oxide in films during growing and annealing AZO films [18]. Some additional incorporation of oxygen atoms in the case of polycrystalline films can take place at grain boundaries and forms electrical barriers [1, 9].

The results of compositional analysis of the samples, presented in Table 2, show that the increase of temperature and time of annealing as well as of concentration of water vapor in atmosphere is accompanied mainly by Zn and Al content deviations in composition of sample 5-2.

The structure of grains (nanocrystals) of polycrystalline films can be conditionally subdivided into the core (or bulk) and the surface (or grain boundary). Both the rearrangement of the surface atoms from their positions in the bulk semiconductor and the formation of

near surface shells with defined composition affect the properties of film grains. Due to a high ratio of surface area to volume of film grains, the structure and composition of their boundaries (shells) may have particular significance for physical properties of polycrystalline films [19].

So, there are reasons to suppose, that a reduced conductivity of AZO samples is mainly attributed to changes of surface comparing to bulk electron structure of film grains [2, 15, 20] and that damp heat treatment at 100 °C introduces stronger modification in near surface regions of the grains.

Table 2.

Composition of AZO samples

Samples (after corresponding final treatment)	Concentration, at. %		
	Zn	O	Al
5-0	44.83	49.20	5.97
5-1	44.72	48.72	6.56
5-2	46.38	48.89	4.73
5-3	44.36	48.76	6.87

It is shown early that the resistivity increase of ZnO films correlates with the decrease in the free carrier density and, as a result, with the decrease of the losses in infrared (IR) region [2, 21]. In Figure 5, the RT transmittance of all investigated AZO samples is nearly 80 % in the visible region. However, the transmittance of some samples starts to decrease at wavelengths 1600–2700 nm. The IR losses are the same in the case of non-treated and RT exposured to humid air samples, 5-0 and 5-3 respectively. A decrease of the IR losses is observed upon the increase of heating temperature of samples 5-2 and 5-1.

The various treatments of the starting film lead also to different changes in visible transmittance. In comparison with non-treated sample 5-0, films exposed to water-vapor atmosphere at RT and 100 °C, sample 5-3 and 5-2, showed a small decrease in transmittance and the blue-wavelength shift of absorption edge, respectively.
The last effect as well as disappearance of the interference fringes for sample 5-2 can be produced by a decrease the thickness or/and the refractive index of the sample due to more high contribution of Al_2O_3-component [18].

The relation between the absorption coefficient (α) and incident photon energy hv can be written as $\alpha \times hv = A\,(hv - E_g)^m$, were A is constant and m = ½, 2 for direct and indirect allowed transitions respectively. The graphs of $(\alpha \times hv)^2$ versus hv are found to lead straight lines over the main part of optical absorption spectra (Fig. 6), supporting the interpretation of direct rather than the indirect band gap for all samples. The band gaps E_g are found to be 3.3 eV for samples 5-0, 5-1, 5-3 and 3.4 eV for sample 5-2 respectively. Thus, AZO film exposed to humid air at 100 °C during 11 hours, sample 5-2, has a gap which agrees with gap of pure ZnO crystals.

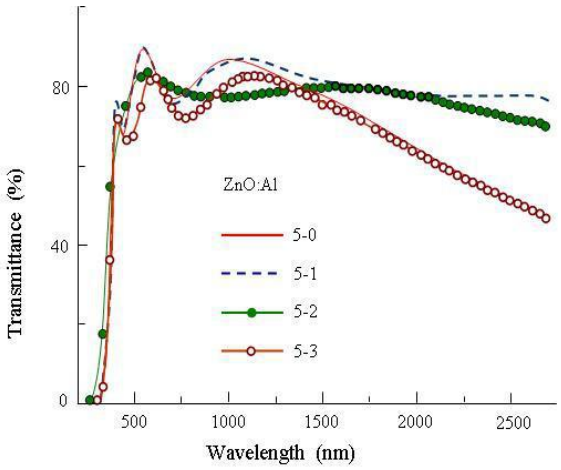

Fig. 5. Transmission spectra at RT of AZO films before, sample 5-0, and after heating in air, sample 5-1, exposure to humid air at RT, sample 5-3, and at 100 °C, sample 5-3. Samples were 400 nm thick and were cutted from film 5. 5-0 is non-treated part of film 5.

A larger band gap of sample 5-2 can be due to three main causes: a free carriers concentration increase [7, 8], purity increase, or a decrease in grain size [9]. The first is not considered to be possible in our case, since a significant resistivity increase was observed; furthermore, the reducing of Al content (Table 2) indicates that a part of aluminum is not electrically active in the sample. This point and the fact that we observe a sharp fall of transmittance at the absorption edge, which is an indication of good crystallinity in the film sample, lead us to ascribe the absorption edge shift to higher purity of grain cores and their size decrease. Sample 5-2 may have smaller grains and a larger band gap due to Al_2O_3 shells formation [18]. The both former effects can be the origine of resistivity increase [22].

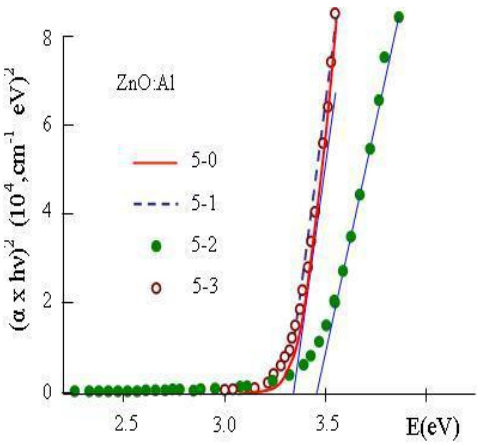

Fig. 6. $(\alpha \times hv)^2$ versus photon energy of non-treated film, sample 5-0, and the film, annealed in air up to 300°C, 5-1, exposed to humid air at 100 °C during 11 Hours and at RT during 20 days, 5-2 and 5-3 respectively. Larger band gap on the right belongs to sample 5-2.

4. CONCLUSION

We investigated the electrical and optical properties of Al-doped ZnO films in terms of annealing and damp heat treatment conditions. A decrease of electrical conductivity

is observed during heating the samples in air, exposure to humid air at 100 °C and exposure to humid air at room temperature. The results suggest that the changes in bulk intrinsic defect concentration and introduction of barriers at grain boundaries play a critical role in the detected effects. The authors consider diffusion of metal interstitials, their aggregation and oxidation as possible origins for the changes. Thus, in order to comprehend fully the properties of elaborated AZO films, it is necessary to determine the structure of their grain boundaries. Future experiments are planned to recognize the origine of a larger band gap but a reduced conductivity of the samples exposured to humid air at 100 °C.

ACKNOWLEDGEMENTS: This work has been supported by Belorussian Republican Fund for Fundamental Research, grant F12 RA-003 and was supported by the Science Development Foundation under the President of the Republic of Azerbaijan- Grant № EIF-1(3)-82/03/1

[1] *J. Hedstrom, H. Ohlsen, M. Bodegart, Kylner, L. Stolt, D. Hariskos, M. Ruckh, H.W. Sckock.* Proc 23rd PSE IEEE Photovolt. Spes. Conf. (IEEE, New, York 1993), P 364.
[2] *W.E. Dewaney, W.S. Chen, J.M. Stewart, R.A. Mickelsen.* // IEEE Transictions on Electron Devices. 1990, V.37, No2, P 428-432.
[3] *M. Powalla, D. Hariskos, E. Lotter, M. Oertel, J. Springer, D. Stellbogen, B. Dimmlerb, R. Schaffler.* Thin Solid Films 431–432 (2003) 523.
[4] *F.H. Karg,* Sol. Energy Mater. Sol. Cells 66 (2001) 645.
[5] *T. Nagase, T. Ooie, H. Kominami, Y. Nakanish, N. Mizutani.* Jpn. J. Appl. Phys., 2003, v. 42, N 3, p. 1179-1184.
[6] *D. Herrmann et al.,* Surf. Coat. Technol. 174-175, 229 (2003).
[7] *K. Kim et al.,* Jpn. J. Appl. Phys. 44, 4776 (2005).
[8] *T. Minami, H. Nanto, and S. Takata,* Jpn. J. Appl. Phys. 24, L605 (1985).
[9] *B. Oh et al.,* J. Cryst. Growth 274, 453 (2005)
[10] *S. Lin, J. Huang, and P. Sajgalik,* Surf. Coat. Technol. 190, 39 (2005).
[11] *Janotti and C.G. Van de Walle,* J.Cryst 287, 58 (2006).
[12] *P. Nunes, E. Fortunato, and R. Martins,* Thin Solid Films 383, 277 (2001).
[13] *J.J. Robbins et al.,* Thin Solid Films 473, 35 (2005).
[14] *M. Schmidt et al.,* Thin Solid Films 361–362, 283 (2000).
[15] *Igalson, M. Wimbor, and J. Wennerberg,* Thin Solid Films 403-404, 320 (2002).
[16] *C. Deibel et al.,* Thin Solid Films 403-404, 325 (2002).
[17] *M.K. Jayaraj, A. Antony, and M. Ramachandran,* Bull. Mater. Sci. 25, 227 (2002).
[18] *R. Menner, R. Schaffler, B. Sprecher, and B. Dimmler,* Proc. of the 2-nd Intern. Conf. on Photovoltaic Solar Energy Conversion, Vienna, Austria, 1998, p. 660.
[19] *D.C. Altamirano - Juarez et al.,* Superficies Vac. 13, 66 (2001).
[20] *O.V. Goncharova, F.V. Karpushko, and G.V. Sinitsyn,* Technical Physics 28, 1142 (1983).
[21] *P. Voitovich, O.V. Goncharova and V.S. Kalinov,* J. Appl. Spectrosc. 72, 301 (2005).
[22] *L.-S. Hsu et al., J. Optoelectr.* Adv. Mater. 7, 3039 (2005).
[23] *Y. Liu and J. Lian,* Appl. Surf. Sci. 253, 3727 (2007).

Received: 10.12.2012

THE THERMAL EXPANSION COEFFICIENT DETERMINATION FOR MAGNETIC SEMICONDUCTOR OF $CuFeSe_2$ CRYSTALS BY HIGH TEMPERATURE X-RAY DIFFRACTION

G.G. GUSEINOV, Y.I. ALIYEV, S.K. ORUDJOV, A.S. AMIROV, B.A. TAHIROV

Institute of Physics, Azerbaijan National Academy of Science,
H. Javid ave., 33, Baku, AZ-1143
e-mail: yusifafshar@gmail.com

The $CuFeSe_2$ tetragonal monocrystals with the lattice parameters: a=5.521 Å, c=11.042 Å, sp.gr. $P\bar{4}2c$, Z=4, ρ_{rent}=5.476 g/cm^3 are grown up from melt at the room temperature. The linear and volumetric thermal expansion (α) are calculated by the high temperature powder x-ray diffraction method in the $20^0C<T<500^0C$ area. It is found that they are approximately $\alpha_a = \alpha_b = 4\cdot10^{-6}\,{}^0C^{-1}$; $\alpha_c = 8.6\cdot10^{-6}\,{}^0C^{-1}$; $\alpha_v = 16.7\cdot10^{-6}\,{}^0C^{-1}$.

Keywords: high temperature X-ray diffraction, ternary copper chalcogenides
PACS: 65.40.-b 68.55.ag 68.60.Dv

INTRODUCTION

Chalcopyrite - $CuFeS_2$ and its chemical analogues such as Cu(Ag)Fe(Ga, In)Se_2(Te_2) are the perspective magnetic and optic semiconductors. It is known that chalcopyrite and its analogues mentioned above are the rectilinear, radiation-resistant materials with the high optical absorption coefficient making them perspective as the material being compatible with silicon photocells [1, 2]. According to the structural characteristics, such analogues are divided into three groups: a) the pure chalcopyrite structured crystals ($I\bar{4}2d$) [3]; b) Cu_3VS_4 ($P\bar{4}2c$) sulvanite structured crystals [4]; c) $Cu_{4-x}Te_2$ (P4/nmm) ricardite structured crystals [5]. Crystallographic parameters of these compound groups are the same, that is the lattice sizes are almost identical. They crystallize in the tetragonal crystal system but differ with their structure and, naturally, symmetry. The second compound group also covers the large group of $A^{II}B_2^{III}X_4 = 2A_{0.5}B_2X_2$ semiconductors [6].

Note that the magnetic and optical properties for the compound described above are discussed in the works [7-12].

When the crystal structures of the chalcopyrite chalcogenides mentioned above are compared, it will be found that $CuFeS_2$ is described as the double lattice of the ZnS cubic sphalerite. In the case of $CuFeSe_2$, the double version of the Cu_3VS_4 cubic sulvanite phase with the a=5.39 Å, s.g. $P\bar{4}3m$ is obtained. And in the case of the $CuFeTe_2$, the Cu and Fe metal valency changes and the structural formula becomes $Cu^+Cu_{0.15}^{2+}Fe^{2+}Fe_{0.23}^{3+}Te_2$. As a result, the layer structure of the $CuFeS_2$ based $Cu_3^+Cu_{0.5}^{2+}Te_2$ rickardite is formed.

The current paper describes the results concerning the linear and volumetric coefficient of thermal expansion determination for $CuFeSe_2$ crystals by high temperature x-ray diffraction in vacuum. Experiments were carried out by "D8 Advance" diffractometer. Mode – 40 kV, 40 mA, $10^0 < 2\Theta < 100^0$, CuKa-radiation, $T=20^0$- 440^0C, vacuum – 10^{-3} tor.

EXPERIMENTS

To study the thermal expansion (CTE), the $CuFeSe_2$ monocrystals were synthesized and grown up from the melt. The X-ray diffraction studies described above jave shown that their quality meet the experimental requirements. To carry out the experiment, the monocrystals were powdered.

The monocrystale powders were placed into the chamber (TTK 450), and diffraction images were taken in every 100^0C (table 1, figure 1). The diffraction data were treated through "EVALUATION" software.

As a result of the diffraction findings it has been found that no specific structure and diffraction modifications take place in the $20^oC<T<450^oC$, and the diffraction images are almost identical, that is the reflection intensity and their angles (2Θ) weakly depend of the temperature rate. It means that structural phase transitions do not take place in the temperature zone mentioned above.

To determine the linear and volumetric expansion (α), the temperature rates of the parameter modifications and the grid volume are used by the formula

$$\alpha_L = \frac{\Delta L}{\Delta t \cdot L}; \qquad (L = a, b, c, V)$$

The calculated rates (CTE) are shown in table 2, and their diagram is in figure 2. It should be noted that according to the calculated data mentioned above, the linear and volumetric expansion is of abnormal nature. Apparently, it may be related to the high covalency in the $CuFeSe_2$ crystal structure.

Table 1.

X-ray diffraction date for $CuFeSe_2$ at different temperature.

T, ^oC	d_c	hkl	Parameter
0	5.49248 3.17806 2.75275 2.46405 1.94890 1.83805 1.66248 1.37863 1.33796 1.26587 1.20436	002 112 200 104 204 214 312 400 324 316 218	a=5.5210 Å c=11.0420 Å V=336.576 $Å^3$ ρ_x=5.4708 g/sm^3
100	5.49403 3.17898 2.46419 1.94982 1.83838 1.66306 1.53053 1.37916 1.26639 1.20488	002 112 200 104 204 214 312 400 324 316	a=5.5216 Å c=11.0580 Å V=337.1370 $Å^3$ ρ_x=5.4617 g/sm^3
200	5.48097 3.18022 2.75534 2.46556 1.95066 1.83972 1.66434 1.36052 1.33051 1.26748	002 112 200 104 204 214 312 400 324 316	a=5.5240 Å c=11.0610 Å V=337.5217 $Å^3$ ρ_x=5.4555 g/sm^3
300	5.49212 3.18200 2.75924 2.46736 1.95261 1.85071 1.66598 1.53238 1.38160 1.34072 1.26835 1.20700	002 112 200 104 204 214 312 304 400 324 316 218	a=5.5262 Å c=11.0690 Å V=338.0349 $Å^3$ ρ_x=5.4472 g/sm^3
400	5.48812 3.18170 2.76013 2.46826 2.95350 1.84210 1.66654 1.38267 1.34096 1.26912 1.20684	002 112 200 104 204 214 312 400 324 316 218	a=5.5300 Å c=11.0800 Å V=338.8363 $Å^3$ ρ_x=5.4343 g/sm^3

Table 2.

The coefficients of thermal expansion for $CuFeSe_2$ at different temperatures

T, ^oC	$\alpha_a=\alpha_b$	α_c	α_V
20-100	$1{,}1\cdot10^{-6}C^{-1}$	$14{,}4\cdot10^{-6}C^{-1}$	16.6
100-200	$4{,}3\cdot10^{-6}C^{-1}$	$2{,}7\cdot10^{-6}C^{-1}$	11.4
200-300	$3{,}9\cdot10^{-6}C^{-1}$	$0{,}7\cdot10^{-6}C^{-1}$	15.2
300-400	$6{,}8\cdot10^{-6}C^{-1}$	$9{,}9\cdot10^{-6}C^{-1}$	23.7

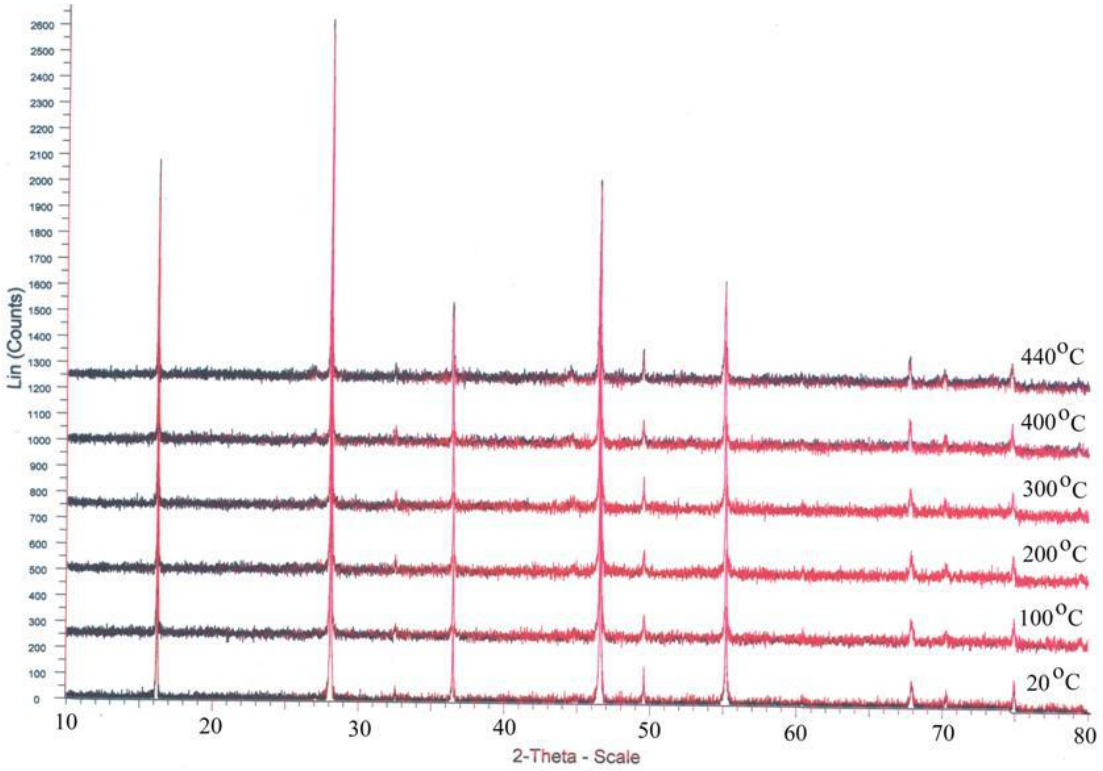

Fig. 1. X-ray diffraction pattern of $CuFeSe_2$ at different temperatures.

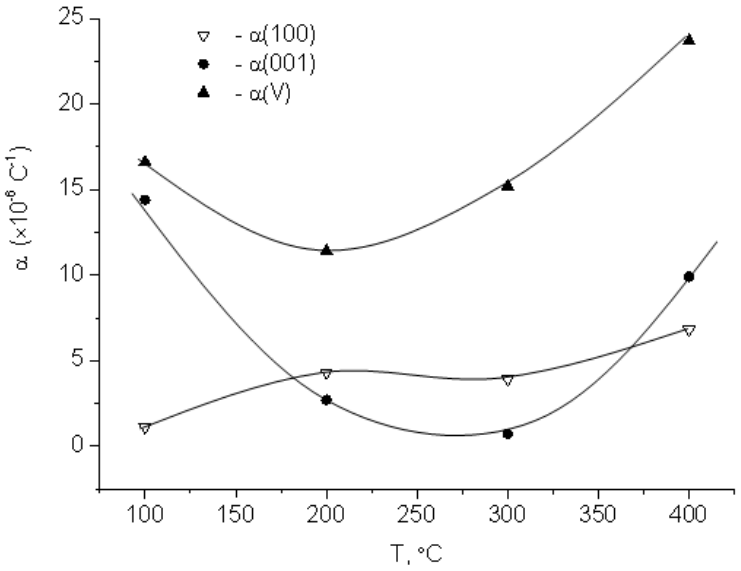

Fig. 2. Dependence of the CTE on temperature.

[1] *S. Fonash, A. Rotvorf, L. Kazmerski, et al. Modern problems of semiconductor photovoltaics: Translation from English., under red.T. Coates, J. Meakin. Academic Press, 1988, 307 p.*

[2] *R.J. Mirzoyev, M.R. Allazov , M.B. Babanly. Zh. Neorgan. Materials, 2008, V.44, № 11, p.1307-1309 (in Russian).*

[3] *L.Pauling and L.O. Brockway. Z. Krist., 82: 188 (1932). 74.*

[4] *J. Felix. J. Am. Min., v. 51, may-june, 1966, p.890-894.*

[5] *S.A. Forman, M.A. Peacock. J.Am. Min., 1949, 34, N5-6, p.441.*

[6] *T. Teranashi , J. Phys. Soc.Jap., 1961, v.16, p.1881-1887.*

[7] *L. Qingyi , H. Junqing, T. Kaibin , et all. J. Crystal Growth, 217, 2000, p. 271-273.*

[8] *J.C. Woolley, A.M. Lamarche , G. Lamarche , et all. J. Magnetisim and Magnetic Materials, 164, 1996, p.154-162.*

[9] *J.M. Delgado , G. Diaz , M. Quintero , et all. Mater. Res. Bull., 27, 1992, p.367.*

[10] *L.V. Kardinova, A.M. Polubotko , V.V. Popov et all.* Semicond. Sci. Technol., 8, 1993, p.1616-1619.

[11] *A.M. Lamarche , J.C. Woolley , G. Lamarche , et all.* J. Magnetisim and Magnetic Materials, 186,

[12] *A.I. Najafov, G.G. Guseinov, O.Z. Alekperov*. J. Physics and Chemistry of Solids, 64. 2003. pp.1873-1875.

Received: 16.11.2012

TEMPERATURE DEPENDENCE OF BARRİER HEİGHTS OF Au/p-GaAs SCHOTTKY STRUCTURES

AHMET ASİMOV, KEMAL AKAY
Department of Physics, Uludağ University, 16059, Görükle, Bursa, Turkey
** Corresponding author. Tel.: 00905350628201*
E-mail address: fizikasimov@hotmail.com , kakay@uludag.edu.tr

ELCHİN HUSEYNOV
The Institute of Radiation Problems of ANAS, Baku, Azerbaijan
**E-mail address: elchin55@yahoo.com*

The current–voltage (I–V) measurements of Au/p-GaAs Schottky barrier diodes (SBD) were measured in the temperature range 80–230K. By using the thermionic emission (TE) theory, the Φ_{B0}(I–V) and n were found to depend strongly on temperature, and the n decreases with increasing temperature while the Φ_{B0} (I–V) increases. The forward bias I–V of SBDs have been studied at the temperatures range of 80–230 K. The values of Φ_{B0} and n ranged from 0.18 eV and 6,74 (80K) to 0.5 eV and 3,06 (230K), respectively. Such behavior of Φ_{B0} and n is attributed to Schottky barrier inhomogeneities by assuming a Gaussian Distribution (GD) of BHs at Au/p-GaAs interface. The zero-bias barrier height Φ_{B0} vs q/(2kT) plot has been drawn to obtain evidence of a Gaussian distribution of the barrier heights, and values of Φ_{B0} = 0,64 eV and σ_0 = 0.042 V for the mean barrier height and zero-bias standard deviation have been obtained from this plot, respectively.

Keywords: Schottky barrier diode; Ideality factor; Temperature dependence of Schottky barrier height, Gaussian Distribution (GD)
PACS:72.10-d; 73.30.+y; 73.40.GK

1. INTRODUCTİON

Schottky barriers formed by metal–semiconductor contact have been widely studied in the past 50 years. Due to technological importance of MS GaAs SBDs, a full understanding of the nature of the electrical characteristics of SBDs in this system is of great interest. Thus, SBSs have an important role for electronic technology [1–6]. Electronic properties of a Schottky diode are characterized by its barrier height and ideality factor parameters. The interface states play an important role on determination of Schottky barrier height and other characteristic parameters and these can affect device performance, stability and reliability [1,7–9]. Gallium arsenide is one of the advantageous semiconductors for high-speed and low-power devices. Experimental results, especially only at room temperature, do not give detailed information about conduction mechanisms or the nature of barrier formation at the MS or MIS Schottky diodes. Therefore, the current–voltage characteristics of the samples have been studied as a function of temperature in the temperature range of 80–230 K. The temperature dependence of the I–V characteristics allows ustounderstand different aspects of conduction mechanisms. Therefore an attempt has been made to study the current transport characteristics of Au/p-GaAs (100) Scottky diodes in the temperature range 80–230 K. The analysis of the I–V characteristics of these devices on the basis of thermionic emission–diffusion (TED) theory of current transport usually reveals an abnormal decrease of zero-bias barrier height and the increase of ideality factor n with decrease of temperature [5–15]. This abnormal behaviour of I–V characteristics of MS contacts at low temperatures has been attributed to the barrier inhomogeneities present in MS contacts. The decrease in the barrier height at low temperatures in fact leads to the non-linearity in the activation energy ($\ln(I_o/T^2)$ vs q/kT) plot. Thus, it is found to be non-linear by the temperature dependence of the barrier height and the ideality factor.

In this study, the I–V characteristics of Au/p-GaAs (100) Schottky diodes were measured in the 80–230K temperature range. The experimental results shows that the barrier height and ideality factor determined from forward bias I–V characteristics were found to be strong function of temperature. The ideality factor n was found to decrease, while the BH increases with the increasing temperature.

2. EXPERİMENTAL PROCEDURES

The Au/p-GaAs Schottky diodes used in this study were fabricated using p-type (Zn-doped) single crystals silicon wafer with (100) surface orientation having thickness of 300 μm, 2 in. diameter. The sample was ultrasonically cleaned in trichloroethylene and ethanol, etched by $H_2SO_4/H_2O_2/H_2O$=5:1:1 (weight ratio) solution for 30 s., rinsed by propylene glycol and blown with dry nitrogen gas. Immediately after surface cleaning, ohmic contacts of low resistance on the backside of the samples were formed by evaporating 1900A˚ thick Au followed by a temperature treatment at 450 C^0 for 5 min in N_2 atmosphere. After that rectifier Schottky contacts were formed on the other faces by evaporating 1900A˚ thick Au. The evaporation process was carried out in a vacuum of $1{,}2x10^{-6}$ Torr. The native oxide on the front surface of the substrate was removed in HF:H_2O (1:10) solution and finally,the wafer was rinsed in de-ionised water for 30 s before forming an organic layer on the p-type GaAs substrate. Preceding each cleaning step, the wafer was rinsed thoroughly in de-ionized water of resistivity of 18 MΩ cm.

The temperature dependence of current–voltage measurements were performed by the use of a Keithley 220 programmable constant current source, a Keithley 614 electrometer in the temperature range of 80–230K using a temperature-controlled Janes vpf-475 cryostat, which enables us to make measurements in the temperature range of 80–230 K. The sample temperature was always monitored by using a copper-constantan thermocouple close to the sample and measured with a dmm/scanner Keithley model 199 and a Lake Shore model 321
auto-tuning temperature controllers with sensitivity better than ±0.1K. All measurements were carried out with the help of a microcomputer through an IEEE-488 ac/dc converter card

3.1. THE CURRENT–VOLTAGE CHARACTERİSTİCS AS A FUNCTİON OF TEMPERATURE

The current-voltage (I-V) measurements of the Au/p-GaAs Schottky diodes were performed in the temperature range from 80 to 230 K are shown in Fig 1. At first, we analyze the experimental I–V characteristics by well-known thermionic emission theory given as follows at forward bias [2]

$$I = I_0 \exp\left(\frac{qV}{nkT}\right)\left[1-\exp\left(\frac{-q}{kT}V\right)\right] \quad (1)$$

where I is the measured current, V is the applied voltage, q is the electronic charge, n is the ideality factor that describes the deviation from the ideal diode equation for reverse bias as well as forward bias, k is the Boltzmann's constant, T is the absolute temperature in Kelvin, I_0 is the saturation current derived from the straight line intercept of lnI at zero-bias and is given by

$$I_0 = AA^{*}T^2 \exp\left(-\frac{q\phi_{B0}}{kT}\right) \quad (2)$$

where q is the electronic charge, A the effective diode area, A^* is the effective Richardson constant and equals 79.4 A $cm^{-2}K^{-2}$ for p-type GaAs [17], k is the Boltzmann constant, T is the temperature in K, Φ_{B0} (I-V) is the zero bias barrier height and *n* is the ideality factor. From Eq. (1), ideality factor n can be written as:

$$n = \frac{q}{kT}\left(\frac{dV}{d(\ln J)}\right) \quad (3)$$

The semilog forward and reverse bias I–V characteristics of Au/p-GaAs SBDs are shown in the temperature range of 80–230 K in Fig. 1. The experimental values of Φ_{B0} and n were determined from intercepts and slopes of the forward-bias lnI versus V plot at each temperature (Fig. 1), respectively. The experimental values of Φ_{B0} and n for the device range from 0.5 eV and 3,06 (at 230 K) to 0,18 eVand 6,74 (at 80 K), respectively. These values are given in Table 1. Fig. 2 shows the values of n obtained from the linear portion of the forward bias I–V characteristics in Fig. 1. The experimental value of n increased with a decrease in temperature, as can be seen in Fig 2.

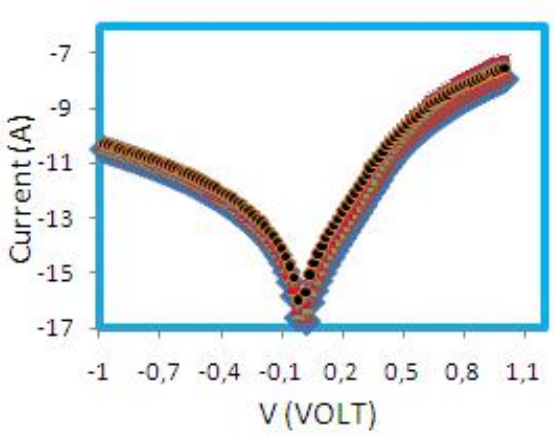

Fig. 1. Experimental forward-bias current–voltage characteristics of Au/p-GaAs Schottky diodes in the temperature range of 80-230 K

Table1. Temperature dependent values of various diode parameters determined from I–V characteristics of Au/p-GaAs Schottky barrier diodes in the temperature range of 80–230 K

T(K)	n	Φ_{B0} (I-V)	I_0
80	6,74	0,18	4,14E-8
110	4,86	0,25	4,58E-8
140	4,04	0,32	6,83E-8
170	3,61	0,39	9,21E-8
210	3,27	0,47	3,61E-7
230	3,06	0,50	8,32E-7

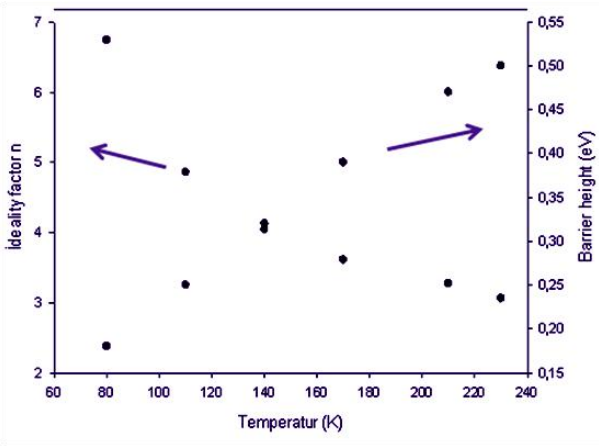

Fig.2. The variation in the ideality factor and zero-bias barrier height with temperature for Au/p-GaAs (SBD).

The zero bias barrier height in Eq. (2) is obtained from the intercept of this plot and can be expressed as:

$$\Phi_{B0} = \frac{kT}{q}\ln\left(\frac{AA^{*}T^{2}}{I_0}\right) \qquad (4)$$

Generally, it is known that the ideality factor n increases while the zero bias barrier height Φ_{B0} decreases with decreasing temperatures [17].The temperature coefficient β of barrier height is calculated 2,2 meV. Moreover the value of (E_a=Φ_{B0}) at 0 K is found to be 0.0134 eV.

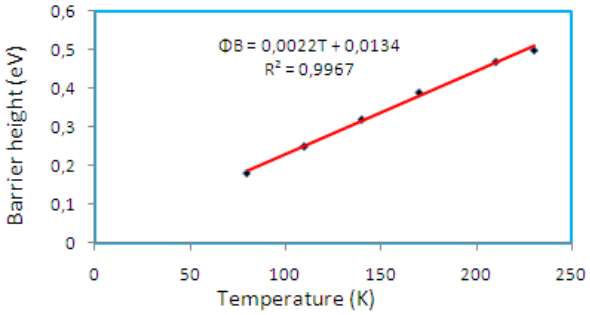

Fig. 3. Zero-bias barrier height vs. temperature of a typical Au/p-GaAs Schottky diode at different temperatures

For the evaluation of the barrier height, one may also make use of the Richardson plot of the saturation current. Eq. (2) can be rewritten as

$$\ln\left(\frac{I_0}{T^2}\right) = \ln(A\cdot A^{*}) - \frac{q}{kT}\Phi_{B0} \qquad (5)$$

The dependence of $\ln(I_0/T^2)$ versus q/kT is found to be non-linear in the temperature range measured (Fig.4). The non-linearity of the conventional $\ln(I_0/T^2)$ versus q/kT is caused by the temperature dependence of the barrier height and ideality factor. The values of the activation energy (E_a) and Richardson constant (A^{*}) were obtained from the slope and intercept of this straight-line as 0,0084 eV and $1{,}1\times10^{-10}$ A/cm^2 K^2, respectively. This value is very much lower than the known value of 79 A/cm^2 K^2 in for holes in p-type GaAs. The value of activation energy (E_a) 0,0084 eV is very close to 0,0134 eV of the zero bias barrier height $\overline{\Phi}_{Bo}$ (T = 0).

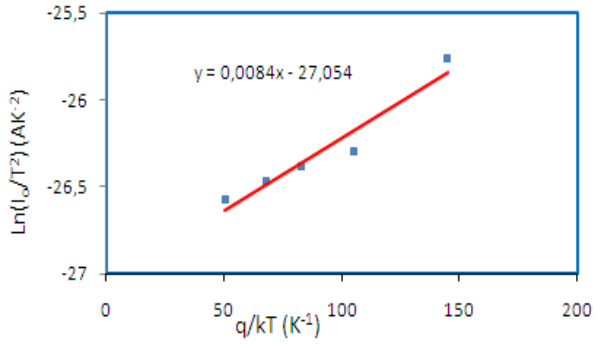

Fig. 4. Richardson plot of $\ln(I_0/T^2)$ vs. q/kT for Au/p-GaAs Schottky diode.

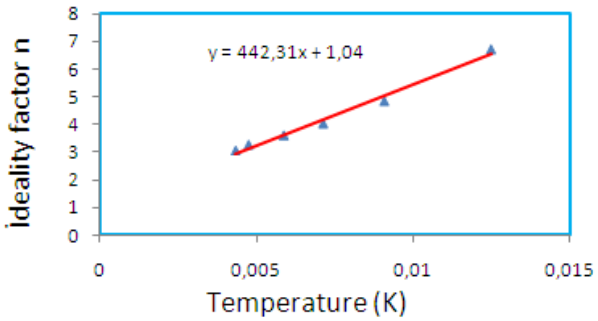

Fig. 5. The plot of n – 1/T for the Au/p-GaAs Schottky barrier.

3.2. THE T_0 EFFECT

The ideality factor increasing with the decreasing temperature was found to change linearly in Fig. 5 with the inverse temperature as

$$n(T) = n_0 + \frac{T_0}{T} \qquad (6)$$

where the n_o and T_o are constant which were found to be 1,04 and 442 K, respectively. The increase in the ideality factor with the decreasing temperature is known as T_o effect [16].

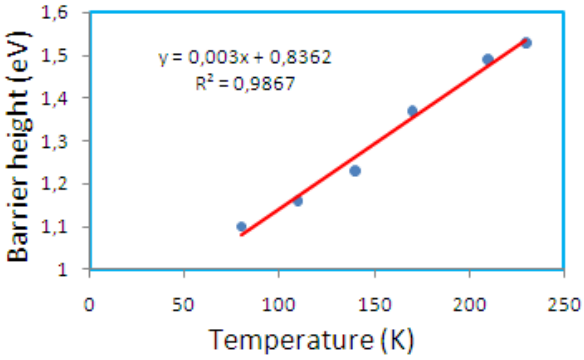

Fig. 6. Temperature dependence of flat-band barrier height for Au/p-GaAs Schottky diode

The barrier height, which decreases with decreasing temperature, obtained from Eq. (2) is called apparent or zero-bias barrier height. The barrier height obtained under flat-band condition is called flat-band barrier height and is considered to be real fundamental quantity. The flat-band BH Φ_{bf} can be calculated from the experimental ideality factor and zero-bias BH Φ_{b0} according to [18].

$$\Phi_{bf} = n\Phi_{bo} - (n-1)\left(\frac{kT}{q}\right)\ln\left(\frac{N_V}{N_A}\right) \qquad (7)$$

where N_v is the effective density of states in the valence band and N_A is the acceptor concentration .The temperature dependent barrier height Φ_{bf} is obtained from Eq. (7) for each temperature and presented in Table 1. The flat-band Φ_{bf} is also shown in Fig. 6 as a function of the temperature. The Φ_{bf} increases with decreasing temperature in the temperature range of 80–230 K.

Furthermore, the temperature dependence of the flat-band barrier height can be described as:

$$\Phi_{bf}(T) = \Phi_{bf}(T=0) + \alpha T \qquad (8)$$

where $\Phi_{bf}(T = 0K)$ is the flat-band barrier height extrapolated to zero temperature and α is the temperature coefficient of $\Phi_{bf}(T)$. In Fig. 6, the fitting of the $\Phi_{bf}(T)$ yields $\Phi_{bf}(T=0)$= 0,84eV and $\alpha = 3\times10^{-3}$ eV/K.

3.3. THE ANALYSİS OF THE İNHOMOGENEOUS BARRİER AND MODİFİED RİCHARDSON PLOT.

The above abnormal behaviors can be explained using an analytically potential fluctuation model based on spatially inhomogeneous barrier heights at the interface [7,12]. Let us assume a Gaussian distribution of the barrier heights with a mean value Φ_{B0} and a standard deviation σ_s in the form:

$$P(\Phi_b) = \frac{1}{\sigma_S\sqrt{2\pi}}\exp\left(-\frac{(\Phi_b - \bar{\Phi}_b)^2}{2\sigma_S^2}\right) \qquad (9)$$

where Φ_{B0} denotes the mean barrier height, σ_s the standard deviation and $1/(\sigma_S\sqrt{2\pi})$ stands for the normalization constant of the Gaussian barrier height distribution. The total current through the SB at the forward bias then becomes

$$I(V) = \int_{-\infty}^{+\infty} I(\Phi_B, V) P(\Phi_B) d\Phi \qquad (10)$$

where $I(\Phi_B, V)$ is the current at a bias V for a barrier of height based on the ideal (TED) theory and $P(\Phi_B)$ is the normalized distribution function giving the probability of accuracy for barrier height. Now integration from - ∞ to + ∞, the current *I(V)* through a Schottky barrier at a forward bias V has a similar from Eqs.(1) and (2) but with the modified BH as, we get

$$I(V) = AA^*T^2\exp\left[-\frac{q}{kT}\left(\bar{\Phi}_B - \frac{q\sigma_S^2}{2kT}\right)\right]\exp\left(\frac{qV}{n_{ap}kT}\right)\left[1-\exp\left(\frac{-qV}{kT}\right)\right] \qquad (11)$$

with

$$I_o = AA^*T^2\exp\left(-\frac{q\Phi_{ap}}{kT}\right) \qquad (12)$$

where $\overline{\Phi}_{Bo}$ and n_{ap} are the apparent barrier height and apparent ideality factor, respectively. The assumption of the Gaussian distribution for the BH yields the following equation for the barrier height [12]

$$\Phi_{ap} = \overline{\Phi}_{Bo} - \frac{q\sigma_o^2}{2kT} \qquad (13)$$

where $\overline{\Phi}_{Bo}$ is the mean SBH at zero bias and extrapolated towards zero temperature, σ_o is the standard deviation at zero bias. In the ideal case (n=1), the expression is obtained as following suggested by [7,8,33]

$$\left(\frac{1}{n_{ap}} - 1\right) = \rho_2 - \frac{q\rho_3}{2kT} \qquad (14)$$

where ρ_2 and ρ_3 are the voltage coefficients that depict the voltage deformation of the barrier height distribution.The experimental $\overline{\Phi}_{ap}$ vs. q/2kT and ((1/n)-1) vs.q/2kT plots obtained from Eqs.(3) and (4), respectively,from Fig. 1 are shown in Fig.7. The temperature dependence of the SBH Au/p-GaAs (100) Schottky diodes (Fig.7) depicts one Gaussian distribution with $\overline{\Phi}_{Bo}$(T=0)=0,64 eV and σ_0=0,042 eV in the 80-230K. The standard deviation is a measure of the barrier homogeneity. The lower value of σ_0 corresponds to more homogeneous BH. Clearly, the diode with the best rectifying performance presents the best barrier homogeneity with the lower value of standard deviation. It was seen that the value of σ_0 =0,042V is not small compared to the mean value of Φ_{B0}; and it indicates the presence of the interface inhomogeneities. The plot of n_{ap} vs. q/kT should be a straight line that gives voltage coefficients ρ_2 and ρ_3 from the intercept and slope, respectively (Fig.7(b)). The values of ρ_2= - 0,58V and ρ_3= - 0,0018V were obtained from the experimental n_{ap} vs. 1/T plot (Fig. 7). The linear behavior of this plot demonstrates that the ideality factor does indeed express the voltage deformation of the Gaussian distribution of the Schottky BH. Furthermore, the experimental results of n_{ap} fit very well with theoretical Eq. (14) with ρ_2=-0,58 V and ρ_3= 0,0018V: The continuous solid line in Fig. 2 represents data estimated with these parameters using Eq. (14).

Now, combining Eqs. (12) and (13), we get

$$\ln\left(\frac{I_0}{T^2}\right) - \left(\frac{q^2\sigma_o^2}{2k^2T^2}\right) = \ln(AA^*) - \frac{q\overline{\Phi}_{Bo}}{kT} \qquad (15)$$

The modified $\ln(I_0/T^2) - q^2\sigma_o^2/2k^2T^2$ versus q/kT plot according to Eq. (15) should give a straight line with the slope directly yielding the mean $\overline{\Phi}_{Bo}$ and the intercept ($\ln AA^*$) at the ordinate determining A^* for a given diode area A (Fig. 8). In Fig.8, the modified $\ln(I_0/T^2) - q^2\sigma_o^2/2k^2T^2$ versus q/kT plot gives $\overline{\Phi}_{Bo}$(T = 0) and A^* as 0,17 eV and 3,2x10^{-7} A cm^{-2} K^{-2}, respectively.

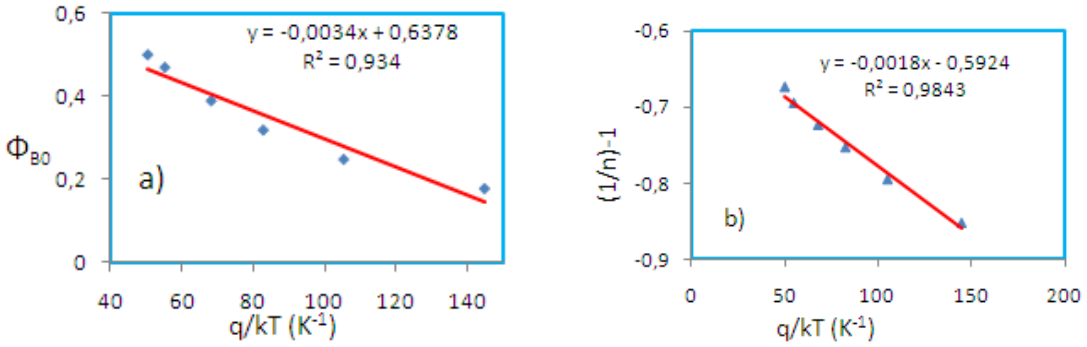

Fig. 7. Temperature dependence of barrier height (Φ_{B0}) (a) and ideality factor ((1/n)-1) (b) for Au/p-GaAs(100).

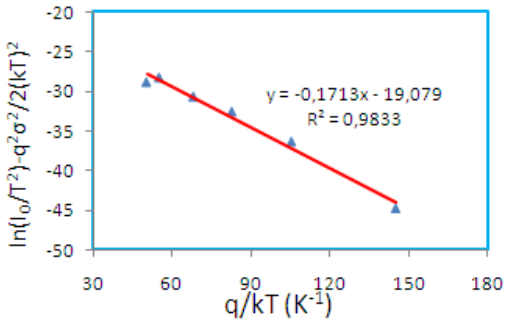

Fig. 8. Modified Richardson $\ln(I_0/T^2) - q^2\sigma_o^2/2k^2T^2$ vs q/k*T* plot for the Au/p-GaAs Schottky diode according to Gaussian distribution of the barrier height

4. CONCLUSİON

The current conduction mechanism across Au/p-GaAs Schottky diode was carried out using (I-V) measurements in the height temperature range of 80–230K. While the zero-bias SBH (Φ_B) increases with the increasing temperature, the ideality factor n decreases with increasing temperature. This observation has been attributed to barrier inhomogeneities explained by assuming a Gaussian distribution of SBHs due to barrier in homogeneities that prevail at interface. In order to obtain evidence of a Gaussian distribution of BHs, we have plotted Φ_B vs. 1/2kT graphs, and from which the values of $\overline{\Phi}_{Bo}$ (T=0) = 0,64 eV and σ_0 = 0,042 eV for mean SBH. The behavior of the flat-band BH was calculated from the I-V characteristics in the range of 80–230 K. The flat-band BH, Φ_{bf}, a fundamental measure of the Schottky barrier which eliminates the effects of image force lowering, is calculated from I-V-T data to be Φ_{bf}=0,84 eV with a negative temperature coefficient, α=3 meVK^{-1}.

[1] *S.M. Sze*, Physics of Semiconductor Devices, second ed., Wiley, New York, 1981.

[2] *E.H. Rhoderick, R.H. Williams*, Metal–Semiconductor Contacts, 2nd ed., Clarendon Press, Oxford, 1988. Crowell CR. Solid-State Electron 1977;20:171.

[3] *X. Lu, X. Xu, N.Q. Wang, Q. Zhang, M.C. Lin*., J. Phys. Chem. B 105 (2001) 10069.

[4] *M. Biber, M. Çakar, A. Türüt*, J. Mater. Sci. Mater. Elect. 12 (2001) 575.

[5] *M. Okutan, E.N. Başaran, F. Yakuphanoglu*, Appl. Surf. Sci. (2005) in press.

[6] *E.H. Rhoderick*, Metal–Semiconductor Contacts, Oxford University Press, 1978, p.121.

[7] *Akkal B, Benemara Z, Boudissa A, Bouiadjra NB, Amrani M, Bideux L, et al.* Mater Sci Eng B 1998;55:162.

[8] *Ş. Altındal, S.Karadeniz, N.Tuğluoğlu, A. Tataroğlu.* Solid-State Electron 2003;47:1847.

[9] *Ş. Karataş , Ş. Altındal , M. Cakar* . Physica B 2005;357:386. Maeda K. Surf Sci 2001;493:644.

[10] *F.A. Padovani, R. Stratton.* Solid State Electron 1966;9:695.

[11] *B.H. Lee, L. Kung, R. Nieh , W.J. Qi , J.C.Lee*. Appl Phys Lett 2000;77:1926.

[12] *Chand S, Kumar* J. Semicond Sci Technol 1996;11:1203.

[13] *M.K. Hudait , S.P. Venkateswarlu , S.B. Krupanidhi*. Solid State Electron 2001;45:133.

[14] *Chand S, Kumar* J. Appl Phys A 1997;65:497.

[15] *J.H. Werner, H.H. Güttler*. Physica Scripta 1991;T39:258.

[16] *O. Güllü , O. Barış , M. Biber , A. Türüt* . Appl Surf Sci 2008;254:3039.

[17] *U.P. Singh, P.C. Srivastava* 'Hydrogenation studies in p-GaAs ' İndia 1222(1998).

[18] *S. Ashok, J.M. Borrego, R.J. Gutmann*, Solid State Electron. 22 (1979) 621.

Received: 20.11.2012

THE LATTICE LONG-WAVE OSCILLATIONS OF GeS NANOCRYSTALS

F.M. HASHIMZADE, D.A. HUSEYNOVA
Institute of Physics of Azerbaijan National Academy of Sciences, Baku, Azerbaijan
M.A.Nizametdinova
Azerbaijan University of Architecture and Construction, Baku, Azerbaijan

The long-wave lattice oscillation frequencies of GeS crystal with layered structure are calculated in the limit of linear chain model. The significant smoothing (30-40%) of low-frequency CS-active modes with crystal thickness decrease up to two layers is predicted.

Keywords: layered crystals, nanocrystals, phonons
PACS: 63.20.-e

1. INTRODUCTION

In work of Wieting [1] it is shown that lattice long-wave lattice oscillations (LLO) of layered crystals MoS_2 and GaSe can be described within framework of chain model. The main point of Wieting model is that crystal is modeled by chain of atomic plane posited along the direction perpendicular to layers. Each plane contains only one of atoms of crystal unit cell. Each plane consists in only one of atoms of crystal unit cell. The interplane force constants of two types (compression and shift) which are defined from comparison of some calculated frequencies and experimental ones (by parameter number), are model parameters. In GeS case it is necessary to change Wieting model introducing 3 types of force constants, 2 types for atom shift parallel to layers (shift ones) and 1 type for shifts perpendicular to layers (compression ones) correspondingly. Besides, we introduce the additional force constant of each type, the necessity of which is caused by bond structure peculiarity in GeS. It is known that in this crystal the metal atom connects with two chalcogen atoms of neighbor atomic plane with both lengths 2.448Å and at the same time one connects with chalcogen atom positing after neighbor plane with bond length 2.438 Å. [2]. (see fig.1). The supposed model is the some modification of known Wieting model. There is one more insignificant difference from Viking model which is in the fat that in GeS the interlayer bond is carried out by cations but not anions as it takes place in Wieting model.

2. THE DESCRIPTIONS OF STRUCTURE AND MODEL.

The crystal structure GeS contains 4 formula units in crystal elementary cell. The symmetry space group is D_{2h}^{16} .

The crystal elementary cell has two layers which transform into each other by inversion operation. The unique choice of designations of crystallographic axis direction for crystals with the given symmetry space group doesn't exist in literature. Here we introduce the following designations: "y" corresponds to direction of the least lattice parameter length, "z" is the most length of crystal lattice period (direction perpendicular to layers).

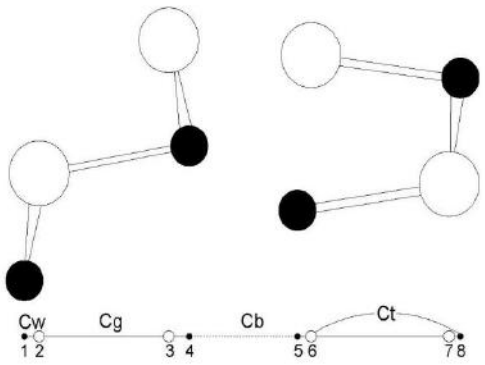

Fig.1. The structure fragment of crystal and chain model of GeS. The black circles are metal atoms, white circles are chalcogen atoms.

For LLO description I within framework of chain model the following force constants for each of shifts of atomic planes ($i \rightarrow x,y,z$) are introduced correspondingly: C_w^i is force constants between neighbor planes of metal and chalcogen, C_t^i is force constants between following (second after neighbor) planes of metal and chalcogen, C_g^i is force constants between neighbor chalcogen planes, C_b^i is force constants between neighbor metal planes (intralayer).

3. CALCULATION

The secular determinant of dynamic matrix by 24 order for GeS in chain model divides on 3 determinants by 8 order. Using the crystal symmetry, each from secular determinants by 8 order can be further reduced on determinants by 2 order, that gives the simple analytical expressions for LLO frequencies. The expansion of GeS oscillation presentation for Brillouin zone center on irreducible representations of D_{2h} point group and corresponding solutions of secular equation of lattice dynamics in chain model are given below:

$$\Gamma_{vib} = 4A_g+2A_u+2B_{1g}+4B_{1u}+4B_{2g}+2B_{2u}+B_{3g}+4B_{3u} \quad (1)$$

From them three ones are acoustic branches (B_{1u}+ B_{2u}+ B_{3u}) and two ones are inactive branches $2A_u$.

$$\omega^2_{\mathrm{B2u,B3u,B1u}} = \frac{(C_w^{y,z,x}+C_t^{y,z,x})(M_A+M_B)}{M_A M_B} \quad (2)$$

$$\omega^2_{\mathrm{B3g,B2g,Ag}} = \frac{1}{2}\left(\frac{2\mathrm{C_b^{y,z,x}}+\mathrm{C_t^{y,z,x}}+\mathrm{C_w^{y,z,x}}}{M_A} + \frac{\mathrm{C_t^{y,z,x}}+\mathrm{C_w^{y,z,x}}}{M_B} \pm \frac{1}{M_A M_B}\left(\sqrt{(-8(2\mathrm{C_b^{y,z,x}}(\mathrm{C_t^{y,z,x}} + \mathrm{C_w^{y,z,x}}))\, M_A M_B + (2\mathrm{C_b^{y,z,x}}M_B + (\mathrm{C_t^{y,z,x}} + \mathrm{C_w^{y,z,x}})(M_A + M_B))^2}\right)\right) \quad (3)$$

$$\omega^2_{\mathrm{B1g,Ag,B2g}} = \frac{1}{2}\left(\frac{2\mathrm{C_b^{y,z,x}}+\mathrm{C_t^{y,z,x}}+\mathrm{C_w^{y,z,x}}}{M_A} + \frac{2\mathrm{C_g^{y,z,x}}+\mathrm{C_t^{y,z,x}}+\mathrm{C_w^{y,z,x}}}{M_B} \pm \frac{1}{M_A M_B}\left(\sqrt{(-8(2\mathrm{C_t^{y,z,x}}\mathrm{C_w^{y,z,x}} + \mathrm{C_g^{y,z,x}}(\mathrm{C_t^{y,z,x}} + \mathrm{C_w^{y,z,x}}) + \mathrm{C_b^{y,z,x}}(2\mathrm{C_g^{y,z,x}} + \mathrm{C_t^{y,z,x}} + \mathrm{C_w^{y,z,x}}))M_A M_B + (2\mathrm{C_g^{y,z,x}}M_A + 2\mathrm{C_b^{y,z,x}}M_B + (\mathrm{C_t^{y,z,x}} + \mathrm{C_w^{y,z,x}})(M_A + M_B))^2}\right)\right) \quad (4)$$

$$\omega^2_{\mathrm{Au,B1u,B3u}} = \frac{1}{2M_A M_B}\left(2\mathrm{C_g^{y,z,x}}M_A + (\mathrm{C_t^{y,z,x}} + \mathrm{C_w^{y,z,x}})(M_A + M_B) \pm \sqrt{(-8(2\mathrm{C_t^{y,z,x}}\mathrm{C_w^{y,z,x}} + \mathrm{C_g^{y,z,x}}(\mathrm{C_t^{y,z,x}} + \mathrm{C_w^{y,z,x}}))M_A M_B + (2\mathrm{C_g^{y,z,x}}M_A + (\mathrm{C_t^{y,z,x}} + \mathrm{C_w^{y,z,x}})(M_A + M_B))^2}\right) \quad (5)$$

The fitting of calculated frequencies with the aim of force constant finding is carried out on more reliable data on CS.

Table 1.

The calculated and experimental frequencies LLO GeS

Symmetry	Experiment	Calculation
A_g	48, 112, 238, 269 [3,4,5]	48, 112, 238, 269
A_u	isn't active	70, 243
B_{1g}	94, 245 [3,5]	94, 245
B_{1u}	117, - , 257 [6]	81, 236, 264
B_{2g}	75, 130, 281, 329 [3,4,5]	75, 130, 281, 329
B_{2u}	201[6]	208
B_{3g}	56, 212 [3,5]	56, 212
B_{3u}	105, 237, 280 [6]	117, 276, 329

The given below model force constants in 10^4 dyn/cm units are obtained by the fitting way to CS frequencies which are lattice active oscillations.

$$\{C_b^y = 1.0, C_t^y = 0.057, C_w^y = 5.64, C_g^y = 1.96\}$$
$$\{C_b^z = 1.8, C_t^z = 1.02, C_w^z = 8.97, C_g^z = 0.03\}$$
$$\{C_b^x = 0.725, C_t^x = 1.14, C_w^x = 6.14, C_g^x = 6.26\}$$

The calculated frequencies of IR-active modes not essentially satisfactory agreed with experiment. At an average the declination is 16%. As it is known this situation is characteristic for the force constant model and is explained by the not taking under consideration of long-range electrostatic forces between atoms [1].

4. THE MODEL USE TO LLO FREQUENCY CALCULATIONOF GES CRYSTALS

Let's consider the dependence of LLO frequencies of GeS layered crystals in the dependence on layer number consisting in nano-crystal. The nano-crystals of limited thickness we will imitate by the lattice super-cells with corresponding layer number. For example, the nano-crystal by thickness of 8 layers is modeled by the chain, elementary cell of which consists 8 layers. The lattice period is taken big enough, practically endless. In the result of this we obtain the phonon spectrum of limited crystal.

Table 2.

The comparison of LLO calculated frequencies of GeS volume crystal with nano-crystal by thickness in 2 layers and one layer.

Symmetry	Nanocrystal		Volume crystal
	1 layer thickness	2 layer thickness	
A_g	0, 81, 236, 264	32, 103, 237, 266	48, 112, 238, 269
B_{1g}	70, 243	86, 244	94, 245
B_{2g}	0, 117, 276, 329	42, 124, 279, 329	75, 130, 281, 329
B_{3g}	0, 208	32, 211	56, 212

The zero frequencies appear as a result of disappearance of oscillation modes of hard layers. The frequency dependencies of CS -active modes on layer number defining the nano-crystal thickness are shown on the fig.2.

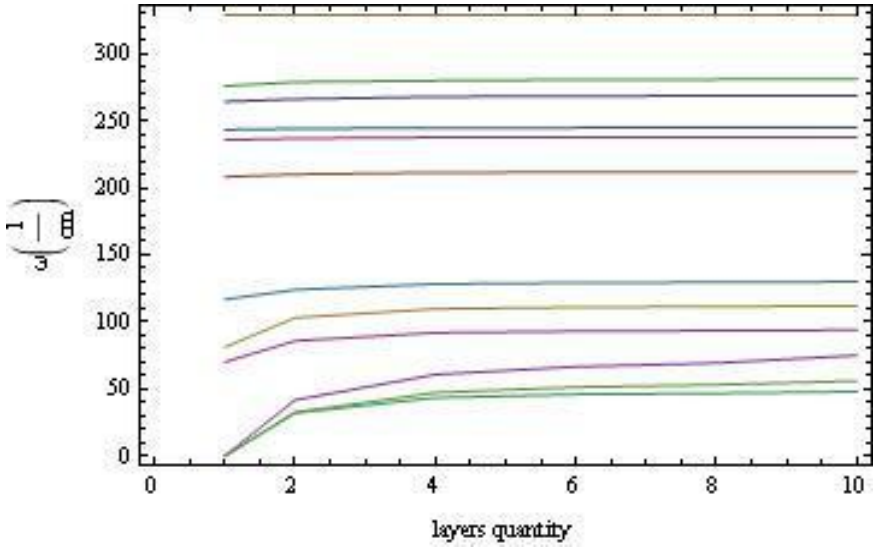

Fig.2. The frequency dependence of **CS**-active phonons on layer number defining GeS nano-crystal thickness.

The frequencies of IR-active and inactive modes don't shift with crystal thickness decrease as it is seen from formula (5) these frequencies don't depend on intralayer force constant. At thickness in one layer, the frequencies of CS-active oscillations coincide with frequencies of IR-active lattice oscillations of volume crystal. The frequencies of intralayer CS-active modes also weakly change. The low-frequency CS-active modes of LLO significantly smooth.

CONCLUSION

The linear chain model predicts the smoothing of low-frequency CS-active modes with crystal thickness decrease. The frequencies of IR-active and inactive reflections in one-phonon optical spectra and light dispersions don't change at all with crystal thickness change. The real observation of size effects on phonon spectra is possible at thicknesses not more than 4nm that corresponds to thickness in 8 layers.

[1] *T.J. Wieting*, Sol.St.Commun.,12, 931, 1973.
[2] *H. Wiedemeier and H.G.v.Schnering*, Z.Kristallogr.,148, 295, 1978.
[3] *H.C. Hsueh, M.C. Warren, H. Vass, G.J. Ackland, S.J. Clark, and J. Crain,* Phys. Rev.B 53,14806, 1996. 1996.
[4] *V. Vorliċek, I. Gregora, and D. Chvostová,* Phys Stat Sol (b), 116, 639, 1983
[5] *H.R. Chandrasekhar, R.G. Humphreys, and M. Cardona*, Phys. Rev. B16, 2981, 1977.
[6] *P. Mihajlovič, P.M. Nikolič and O.H. Hughes*, J. Phys. C: Solid State Phys. 9, L599, 1976.

Received:23.10.2012

INFLUENCE OF HYDROSTATIC PRESSURE ON ELASTIC WAVE PROPAGATION IN LAYERED COMPOUND GaS

G.S. ORUDZHEV*, E.K. KASUMOVA
Azerbaijan Technical University
AZ-1073, H.Javid ave.,25, Baku, Azerbaijan
**horucov@physics.ab.az*

The pressure dependence of velocities of propagation of the elastic waves in gallium sulfide in crystallographic directions [001], [100], [101], [110] and [111] are calculated in pressure range 0-20GPa from Christoffel equations which are solved on values of elastic constants calculated from *ab-initio* principles, considering the phase transition at 3GPa. It was established that in this interval the wave's velocities in all directions increases with increasing pressure, excepting the velocity of transverse wave propagating in direction [100] and polarized perpendicularly to the hexagonal axis, which slightly decreases.

Keywords: GaS, layered crystal, longitudinal and transverse elastic waves, elastic constants, phase transition, Christoffel tensor
PACS: 05.70. Fh, 61.82. Fk, 62.20. Dc

It is known that for each direction in the crystal there are three independent waves with different phase velocities and mutual perpendicular displacement vectors. Christoffel equation is the main equation for whole propagation theory of elastic waves:

$$(\rho\upsilon^2\delta_{ij} - \Gamma_{il})\, u_l = 0, \qquad (1)$$

where δ_{ij} is the Kronecker symbol, Γ_{il} is the Christoffel tensor.

The velocities of the elastic waves can be defined by different ways. In [1] we have used the modified phase-impulse method [2]. The velocities of ultrasound waves are measured in [3] on three samples of gallium sulfide by impulse echo-method. The measurements are carried out parallel and perpendicular to the hexagonal C axis at room temperature and pressure. The authors of [4] have calculated the phase velocity by measuring Brillouin frequencies shifts.

Theoretically the velocities of the elastic waves in GaS at 0GPA have been determined from phonon spectrum [5].

In the present paper for definition of dependence of the elastic waves velocities on pressure in GaS layered crystal from first principles the crystal's elastic constants at hydrostatic pressure values 0, 1, 2, 3, 4, 5, 10, 12, 15 and 20 GPa are calculated. Earlier from *ab-initio* calculations we established that at hydrostatic pressure ~3.166 GPa the reversible structural phase transition without change of symmetry space group takes place in GaS. Before phase transition (phase P1) the gallium atoms occupy the positions 4(f) (2/3, 1/3, z) and after one (phase P2) they occupy the positions 4 (e) (0, 0, z). In present calculations this transition was taken into account.

The calculations are carried out with density functional theory (DFT) [6] in plane wave basis realized in ABINIT code [7]. The calculations were performed using the parallel version of program on 36 computers at Azerbaijan National GRID-segment [8].

For exchange-correlation the local density approximation (LDA) [9] was used. The plane wave energy cutoff was taken 80 Ry. For description of electron-ion interaction the norm-conserving ion pseudopotentials Hartwigsen–Goedecker-Hutter were chosen: 31ga.3.hgh and 16s.6.hgh [10]. The electron configuration $[Ar]3d^{10}+4s^24p^1$ and $[Ne]+3s^23p^4$ are correspondently used for gallium and sulfur atoms. For integration on Brillouin zone we used the grid of k-points with density 8x8x1 generated by Monkhorst-Pack method [11].

To simplify the calculations the crystal's elementary cell was chosen in rectangular parallelepiped form and consists of 16 atoms: 8 Ga atoms and 8 S atoms. The benefit of using such supercell is that we can easily apply specific strains on this.

The elastic constants are calculated in 3 steps. On the first step the self-consistent calculation were made and wave functions of crystal ground state at some initial structure parameters are calculated.

The relaxation and optimization of atom structure geometry up to obtaining the given pressure value (pressure tensor) is carried out on the second stage. While optimization the atom and lattice configuration parameters are iteratively changed until the forces acted on atoms in the cell not become below the given threshold value $5\cdot10^{-7}$ Ry/Å and the established pressure accurateness doesn't exceed $5\cdot10^{-5}$ GPa.

The density values of GaS in 0-20GPa pressure interval are calculated on obtained values of elementary cell volume and given in the table 1.

Table 1.

GaS density

P, GPa	V, 10^{-30} m^3	ρ, kq/m^3
phase P1		
0	318.23	4248.5
1	309.678	4365.83
2	303.23	4458.66
3	297.89	4538.59
phase P2		
3	295.62	4573.47
4	290.79	4649.45
5	286.52	4718.73
10	269.96	5008.24
12	264.73	5107.05
15	257.83	5243.77
20	248.11	5449.22

On the third step the strains were applied to obtain elastic constants. To ensure that elastic constants are within the linear theory of elasticity small strains are needed (in our case ε=0.001).

As elastic constants are defined in an orthogonal coordinate system, we relate cell parameters to Cartesian system XYZ in the following way: the cell parameter *a* is parallel to X axis, the cell parameter *b* is parallel to Y axis and the cell parameter *c* is parallel to Z axis (exactly to hexagonal C axis). Thus for definition of elastic constants C_{11}, C_{12} and C_{13} the strain was applied along X (Y) axis, for C_{33} – along C axis, and for calculation of elastic constant C_{44} the shear deformation between X (Y) and Z axis is given. Using the difference of stress tensors obtained on third and second stages from generalized Hooke's law, the elastic constants of GaS crystal are calculated.

The calculated values of elastic constants under pressure are given in table 2.

Table 2.

GaS elastic constants

P, GPa	C_{ij}, 10^{10} Pa					
	C_{11}	C_{33}	C_{44}	C_{12}	C_{13}	C_{66}
phase P1						
0	13.16	3.69	1.18	3.22	1.06	4.97
1	13.82	5.77	1.65	3.64	1.62	5.09
2	14.50	7.50	2.01	4.03	2.16	5.23
3	14.96	9.04	2.35	4.41	2.64	5.27
phase P2						
3	15.18	7.19	2.92	4.85	3.11	5.17
4	15.67	8.23	3.37	5.25	3.61	5.21
5	16.26	9.24	3.79	5.69	4.15	5.28
10	18.56	13.22	5.29	7.65	6.35	5.46
12	19.41	14.64	5.67	8.38	7.17	5.52
15	20.50	16.58	6.18	9.44	8.37	5.53
20	22.31	19.37	6.62	11.15	10.18	5.58

Then the Christoffel equations (1) are solved with Wolfram Mathematica program and velocities of propagation of the elastic waves in crystallographic directions [001], [100], [101], [110] and [111] are calculated. The Christoffel tensor components for hexagonal crystals are given in table 3.

The dependences of velocities of propagation longitudinal and transverse elastic waves on pressure in different crystallographic directions for both phases of gallium sulfide are given on fig.1.

It is established that the waves velocities in all directions increase versus pressure rise. Only the velocity of transverse mode propagating in the direction [100] and polarized perpendicularly to the hexagonal axis slightly decreases.

In direction [001] the velocities of transverse waves are equal to each other. In [100], [010] and [110] directions longitudinal and corresponding transverse waves propagate with equal velocities. That's why only dependence for the direction [100] is given on the figure.

It's seen from fig.1 that in the first phase the changing under pressure of the wave's velocities calculated from elastic constants C_{33} and C_{44} characterizing the interlayer interaction is stronger than the changing of other velocities, i.e. the anharmonicity of bond forces between layers is essentially bigger than one of intralayer forces [12]. After phase transition the sharp decrease of elastic constants C_{33} and C_{66} and corresponding wave's velocities is observed.

The comparison of known velocity values at 0 GPa is given in table 4. The table shows that theoretical and experimental values of velocities in directions [001], [100] and [101] well agree between each other. The small difference of experimental data can be explained by the difference in density values (in [1] ρ=3750 kg/m^3, in [3] ρ=3913±10 kg/m^3).

We are thankful to Dr N.A.Abdullayev for useful advises.

Table 3.

Christoffel tensor components for hexagonal crystals

Γ_{ik}	[001]	[100]	[101]	[110]	[111]
$\Gamma_{11}=C_{11}n_1^2+C_{66}n_2^2+C_{44}n_3^2$	C_{44}	C_{11}	$\frac{1}{2}(C_{11}+C_{44})$	$\frac{1}{2}(C_{11}+C_{66})$	$\frac{1}{3}(C_{11}+C_{66}+C_{44})$
$\Gamma_{22}=C_{66}n_1^2+C_{11}n_2^2+C_{44}n_3^2$	C_{44}	C_{66}	$\frac{1}{2}(C_{66}+C_{44})$	$\frac{1}{2}(C_{66}+C_{11})$	$\frac{1}{3}(C_{66}+C_{11}+C_{44})$
$\Gamma_{33}=C_{44}n_1^2+C_{44}n_2^2+C_{33}n_3^2$	C_{33}	C_{44}	$\frac{1}{2}(C_{44}+C_{33})$	C_{44}	$\frac{1}{3}(2C_{44}+C_{33})$
$\Gamma_{23}=\Gamma_{32}=(C_{11}+C_{13})n_2n_3$	0	0	0	0	$\frac{1}{3}(C_{11}+C_{13})$
$\Gamma_{13}=\Gamma_{31}=(C_{13}+C_{44})n_1n_3$	0	0	0	0	$\frac{1}{3}(C_{13}+C_{44})$
$\Gamma_{12}=\Gamma_{21}=(C_{11}-C_{66})n_1n_2$	0	0	0	$\frac{1}{2}(C_{11}-C_{66})$	$\frac{1}{3}(C_{11}-C_{66})$

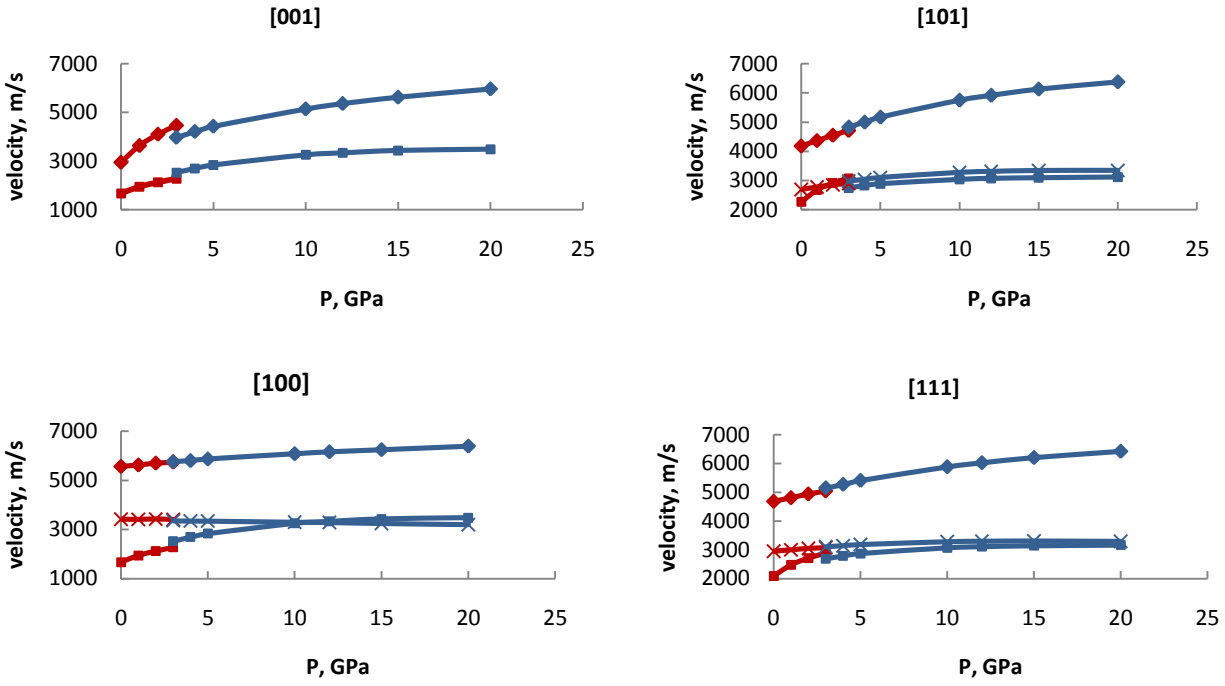

Fig. 1. The pressure dependence the velocities of propagation of longitudinal and transverse elastic waves in directions [001], [100], [111] and [101] (red line – the first phase; blue line – the second phase; rhombs – the longitudinal wave; squares – the transverse waves polarized along C axis, crosses – the transverse waves polarized perpendicular to C axis).

Table 4.

The elastic waves velocities in GaS at 0 GPa

	Propagation direction					
	$\|\|C$		$\perp C$			[101]
Elastic waves velocities, m/s	$\upsilon_{\|\|L}$	$\upsilon_{\perp T}$	$\upsilon_{\perp L}$	$\upsilon_{\|\|T}$	$\upsilon_{\perp T}$	υ_{L}
[1]	3210	1710	6470	1710	4050	–
[3]						
Sample 1	3136	1595	5612	–	3366	–
Sample 2	3170	–	5623	–	3379	–
Sample 3	–	–	–	–	–	4212
[4]	3140*	1610**	5620	1590	3350	–
[5]	3016	1555	5755	1555	3487	–
This work	2948	1667	5566	1667	3420	4180

(*, ** data obtained from Brillouin spectrum: *direction of wave propagation has angle 2.9° with C axis; **propagation direction has angle 5.1° with C axis).

[1] *V. Farajov, R. Akdeniz, E. Kasumova.* International scientific conference UNITECH'03 – Gabrovo proceedings. Technical University of Gabrovo, Bulgaria (20-21 November 2003) II, 333 (2003).
[2] *A.I. Aqaev, Z.A. Iskenderzade, V.D. Faradjev.* Akusticheskiy jurnal, 20, 121 (1974). (In Russian)
[3] *M. Gatulle, M. Fischer, A. Chevy,* Phys. Stat. Sol. B119, 327 (1983)
[4] *Y. Honma, M. Yamada, K. Yamamoto, K. Abe,* J. of the Phys. Soc. of Jap. 52, 2777 (1983)
[5] *Z. Cahangirli,* FTT 54, 1024 (2012). (In Russian)
[6] *P. Hohenberg, W. Kohn,* Phys. Rev. 136, B864 (1964)
[7] *X. Gonze, J. M. Beuken, R. Caracas et al.* Comput. Mater. Sci. 25, 478 (2002)
[8] www.azgrid.org
[9] *W. Kohn, L. Sham,* Phys. Rev. 140, A1133 (1965)
[10] *C. Hartwigsen, S. Goedecker, J. Hutter,* Phys. Rev. B58, 3641 (1998)
[11] *H. Monkhorst, J. Pack,* Phys. Rev. B13, 5188 (1976)
[12] *N. Abdullaev,* FTT 48, 623 (2006). (In Russian)

Received: 08.11.2012

PREPARATION AND OPTICAL PROPERTIES OF $SrAl_2O_4:Eu^{2+}$ NANOPHOSPHOR

S. MAMMADOVA [1], H. STREIT[2], T. ORUCOV[3], Ch. SULTANOV[3]

1. G.M. Abdullayev Institute of Physics, Azerbaijan NAS, Baku, Azerbaijan

2. Anorganische Chemie II Universität Siegen, Adolf-Reichwein-Straße 2 57068 Siegen

3. Research and Devolopment Center for High Technologies, Ministry of Communications and İnformation Technologies

In the present work we report preparation oxide nanophosphors for white LEDs. Their emission and excitation spectra before and after sintering were measured. The mean phonon energy for $SrAl_2O_4$ was evaluated by Raman method and Huang-Rhys parameter S=9 correspond to strong electron phonon coupling regime.

Keywords: nanophosphor, light emitting diode structure, luminescence
PACS: 33.50.-j, 33.50.D

1. INTRODUCTION

Light emitting diode (LED) devices are promising solid state lighting (SSL) devices, with great potential to save electrical energy in lighting applications. There are many LEDs that emit different colors of light. UV LEDs emit near UV light from 380 to 410 nm. Blue LEDs emit blue light from 440 to 480 nm (GaN). Green LEDs emit green light from 520 to 560 nm (GaInN), and red LEDs emit red light from 590 to 630nm (AlGaInP). But for lighting applications, white light is preferred. For LEDs, there are several ways to generate white light. For example, using red, blue, and green LEDs together can generate white light. Using red, blue, and green phosphors to down-convert UV LED emission can also generate white light. The best method is to use yellow/green phosphors to convert part of the blue LED emission to generate white light. This method is also called the binary complementary method [1]. To make white light LEDs, phosphors are often required for light down-conversion. These phosphors are then called LED phosphors. Energy loss during light down-conversion would reduce overall efficiency of the LED device. For this reason, many efforts have been made to search for novel, highly efficient phosphors and to improve the efficiency of the current white light LEDs. LED phosphors normally absorb strongly in the near UV or blue region to down-convert the light emitted by LEDs. Most LED phosphors are from lamp phosphors, TV phosphors, or scintillators. In general, these phosphors work better for LEDs than for fluorescent lamps because LED phosphors are exposed to low energy light (380–470 nm). LED phosphors usually have broad band transitions for absorption and color rendering. Therefore, phosphors with $4f \rightarrow 5d$ transitions are good candidates. Their absorption must be at the LED emission and their emission should meet the requirement for color rendering.

Nanophosphors have drawn considerable attention from scientists working on LEDs. Nanophosphor is a novel concept that was developed in early 1990s. For nanophosphors, the physics and engineering are down to a scale of 1–100 nm. Many new physics phenomena were developed for nanophosphors. One of the advantages of nanophosphors is that the internal scattering within the materials is reduced when the size of the nanophosphors is much smaller than the wavelength of the visible light [2]. Also, the refractive index of materials can be modified by mixing materials with different refractive indexes. A better matching of refractive index between LED and phosphor can enhance light extraction. Luminescent intensity is also reported gain in nanocrystalline materials [3]. When materials are in nanoscale, their surface-to-volume ratio is orders larger than that of fine powders (with a size of about 10 *m*m). Mixing and doping uniformity are also much better for nanophosphors than that for bulk materials during synthesis. Therefore, quality of materials, especially in term of doping uniformity and phase purity, is better and is easier to achieve [4]. As the dopants are well separated and located in each nanoparticle, the energy transfer between identical or nonequivalent emission centers, which can cause concentration quenching, is reduced due to the high surface/volume ratio [5, 6, 7, 8]. By their reduced size, nanophosphors can double the doping concentration without quenching effect. As a result, both absorption and emission intensities of the nanophosphors can reach much higher values. With these advantages, nanophosphors are gradually replacing traditional phosphors in many places for display, indicator, lamp, and LED applications.

In order to achieve sufficient color homogeneity, a significant fraction of small particles is required, which scatter the blue and yellow/green radiation effectively. On the other hand, the stronger the scattering the more blue or yellow/green rays will be reflected back onto the chip or onto the walls of the package before they are finally emitted by the LED.

2. EXPERIMENTS AND RESULTS

Quality of nanophosphors has been greatly improved. Methods for preparation of nanophosphors are usually wet chemical methods, including sol-gel, precipitation, coprecipitation, emulsion, combustion, and spray pyrolysis.

$SrAl_2O_4$ nanoparticles were prepared alternatively by the combustion method. For this purpose, aqueous solution of $Al(NO_3)_3$, $Sr(NO_3)_2$, $Eu(NO_3)_3$ and an organic fuel were heated to 500°C. At this step, the water evaporates, the nitrated are decomposed and it results in

the ignition of the organic fuel, which yields in the formation of a voluminous $SrAl_2O_4$ precursor. Nanoparticles are obtained by annealing the precursor material to 1100°C under argon and hydrogen flow.

As suggested by the original article[1], glycine was applied as organic fuel resulting in carbonized dark products (Fig.1).

Fig.1. Carbonized dark product of combustion synthesis applying glycine as organic fuel.

The wished $SrAl_2O_4$ precursor was first successfully synthesized after changing the glycine against urea (Fig.2).

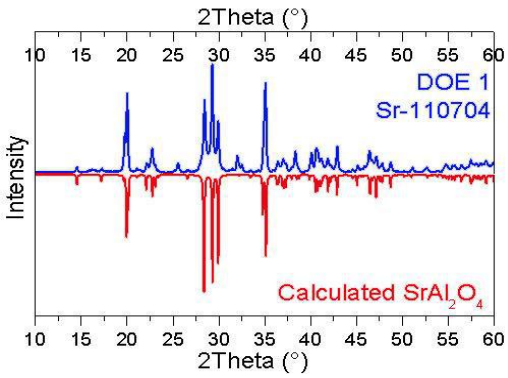

Fig.2. X-ray diffraction analysis of $SrAl_2O_4$ precursor produced applying urea as organic fuel for the combustion synthesis (Sr-110704).

Further experiments were carried out to test thiourea as organic fuel. However it did not result in a voluminous precursor (Fig.3) and its XRD measurement differs from the calculated $SrAl_2O_4$ structure (Fig.4).

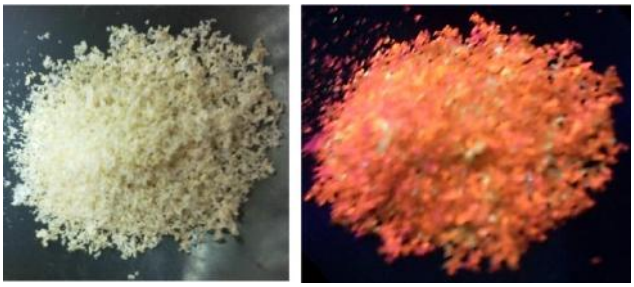

Fig.3. Product of combustion synthesis applying thiourea as organic fuel under day light (left) and UV light (right).

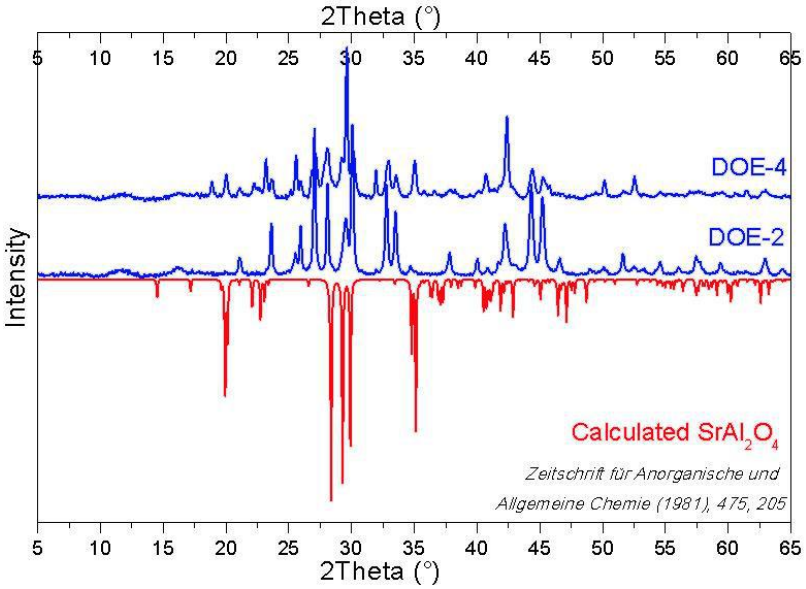

Fig.4. X-ray diffraction analysis of combustion synthesis product applying thiourea (top) compared to calculated $SrAl_2O_4$pattern (bottom).

Precursor produced applying urea in the combustion synthesis formed a voluminous, white mass, which emits light with red, yellow and blue-green colors under UV-light (Fig.5).

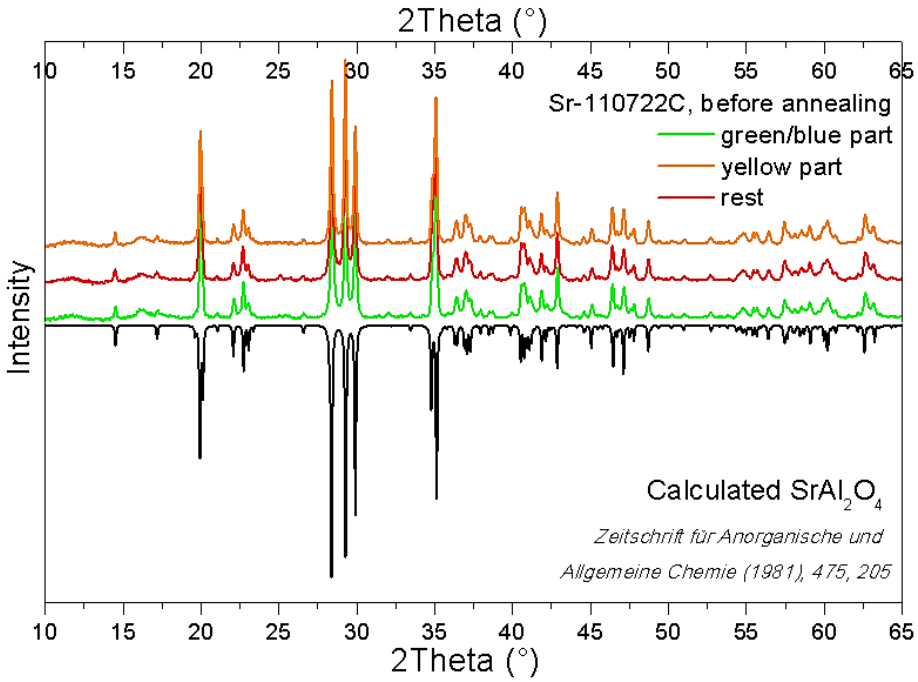

Fig.5. X-ray diffraction analysis of green, yellow and red emitting parts of $SrAl_2O_4$ precursor.

As shown in the Fig.6, all the three parts were characterized as pure $SrAl_2O_4$. Green emission must be caused by Eu^{2+} ions, which occupy the Sr^{2+} position in the $SrAl_2O_4$ lattice.

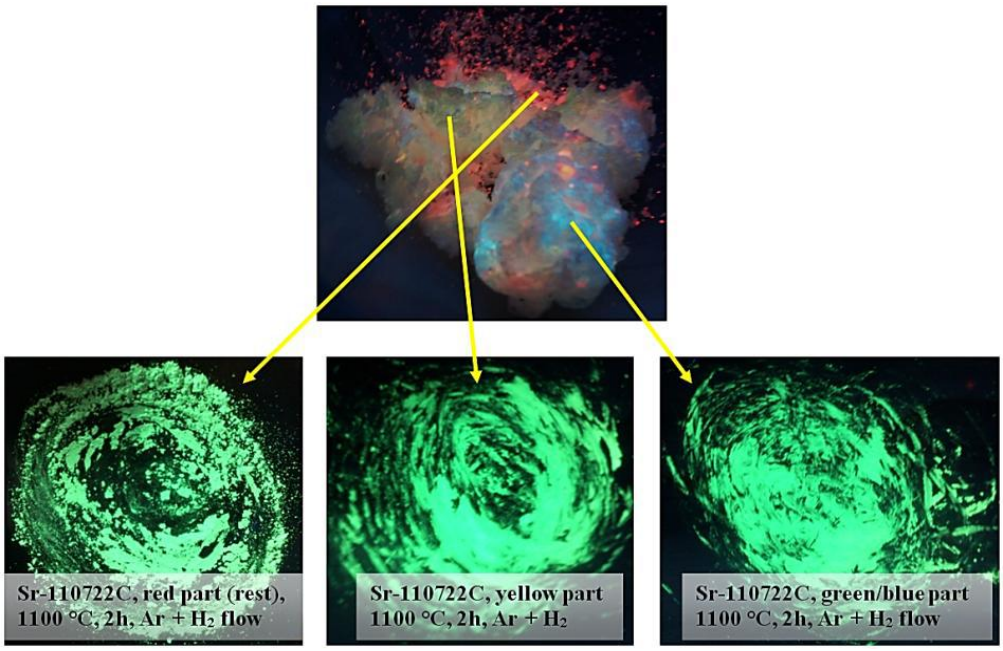

Fig.6. $SrAl_2O_4$ under UV light before (top) and after (bottom) sintering.

Similarly, the red emission is assigned to Eu^{3+} luminescence, reduced to Eu^{2+} after sintering under argon and hydrogen flow. Yellow emission can be caused by lattice defects, which also disappears after sintering at 900°C. This way, the sintering step demonstrated to be important not only to complete the crystallization process but to reduce the remaining Eu^{3+} ions and consequently to obtain the aimed homogeneous green Eu^{2+} luminescence. Fig. 7 shows the emission and excitation spectra of $SrAl_2O_4$ before sintering.

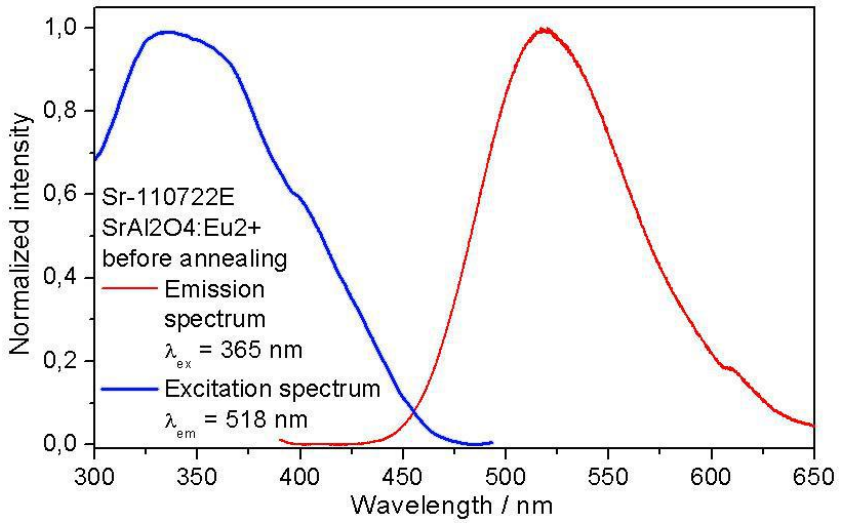

Fig.7. Emission and excitation spectra of $SrAl_2O_4$ before sintering.

In this figure we can see the presence of remaining Eu^{3+} transitions. This transition (~615 nm) is still observed in the emission spectrum of the phosphor sintered for two hours (Fig. 8) and completely disappears after increasing the sintering time to three hours (Fig. 9).

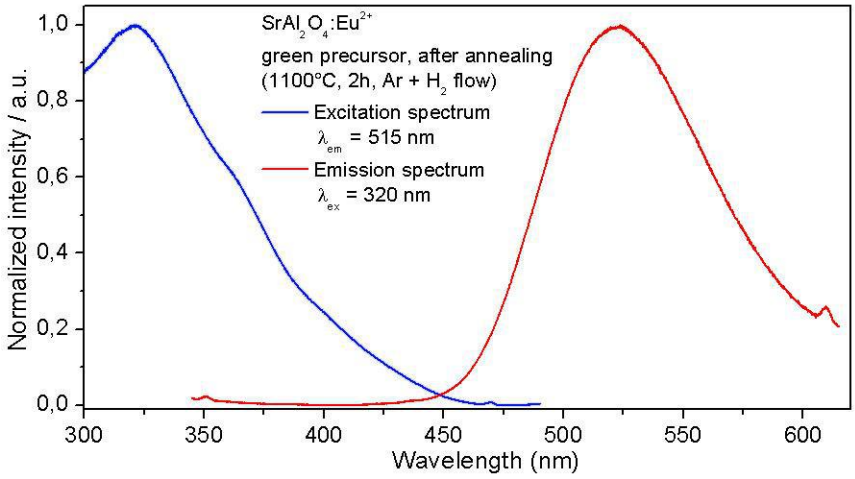

Fig.8. Emission and excitation spectra of $SrAl_2O_4$after sintering for two hours.

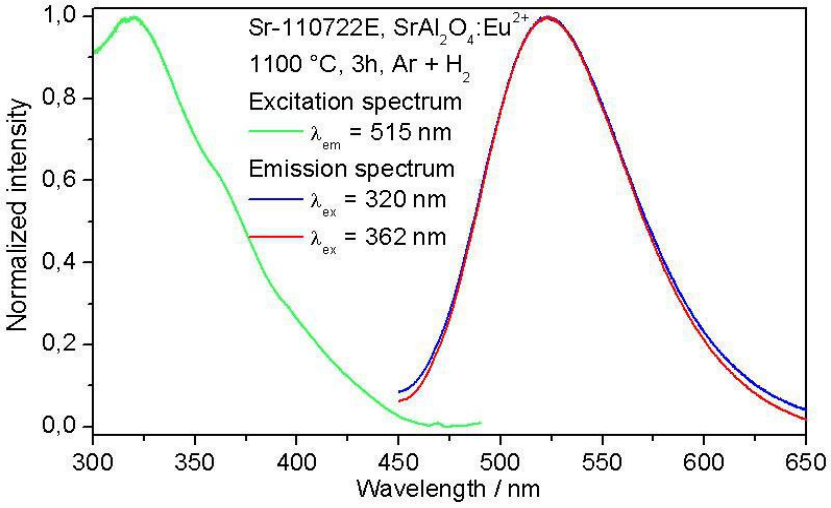

Fig.9. Emission and excitation spectra of $SrAl_2O_4$ after sintering for three hours.

We made this experiment for different concentration of Eu^{2+}

Sample	Before sintering	After sintering	Emission (a) and excitation (b) spectra of $SrAl_2O_4$ with 2%, 4%, 8% of Eu concentrations after sintering.
Sr-111018A (2% Eu)	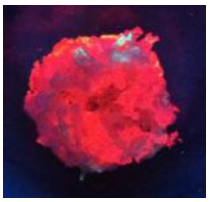	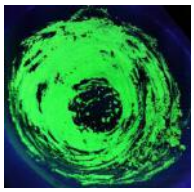	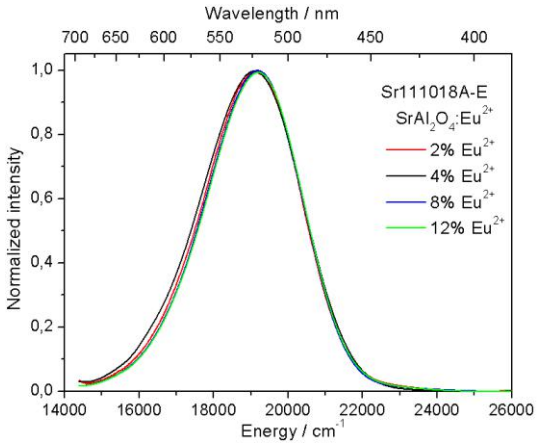 a)
Sr-111018B (4% Eu)	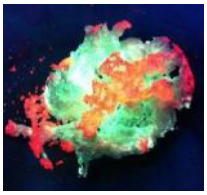	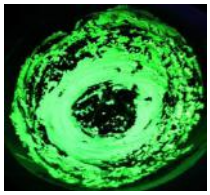	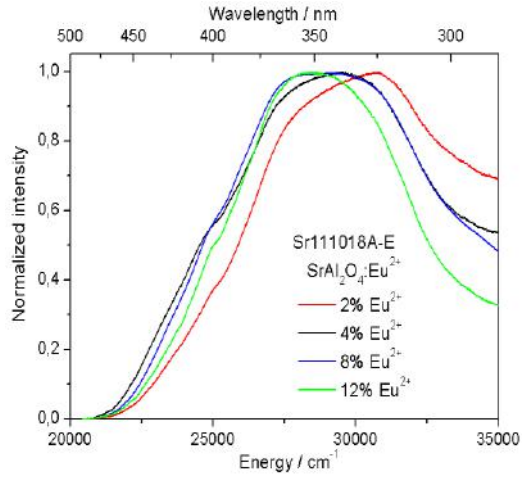 b)
Sr-111018C (8% Eu)	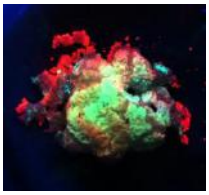	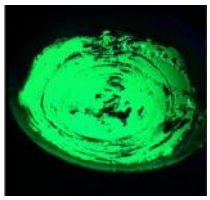	

We will measure particle size of $SrAl_2O_4$: Eu^{2+}, from XRD (fig.10) measurement and particle size distribution from photon correlation specroscopy (PCS) (fig.11) and it is incompatible with size estimated from XRD measurement.

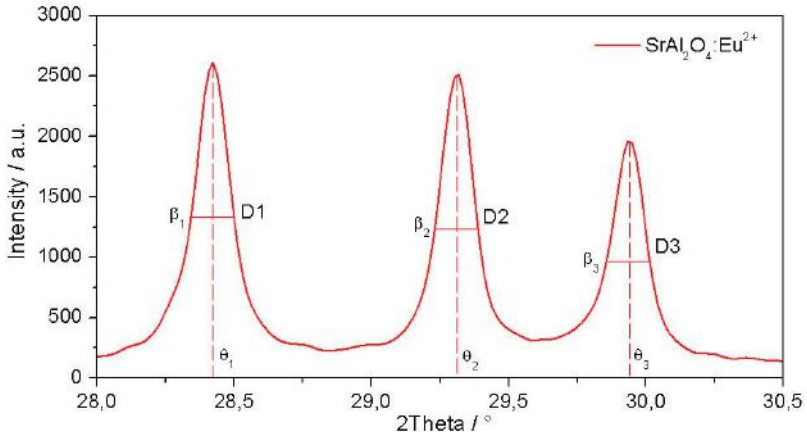

Fig.10. Particle size of $SrAl_2O_4:Eu^{2+}$ estimated in 50 nm from XRD measurement.

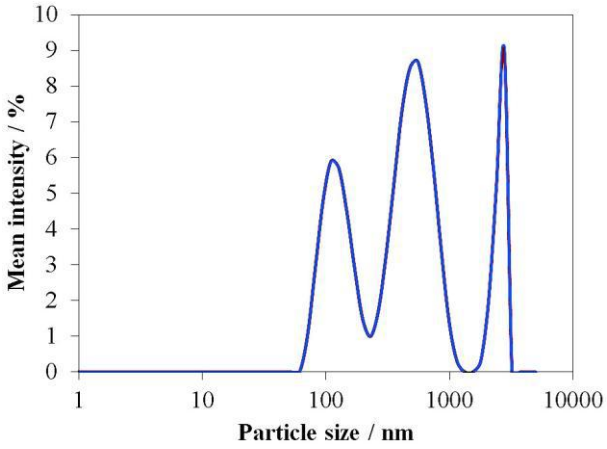

Fig.11. Particle size distribution of $SrAl_2O_4:Eu^{2+}$ measured by photon correlation spectroscopy.

PCS method is good, but the size can be larger than the obtained by electron microscopy, for example, where the particle is removed from its native environment. Because the PCS is only valid for light being scattered once. Any contribution of multiple scattered light leads to erroneous PCS results and misinterpretations. As a consequence, PCS requires highly diluted suspensions in order to avoid multiple scattering.

$$D_1 = \frac{0{,}89 \cdot \lambda}{\beta_1 \cdot \cos\theta_1} = \frac{0{,}89 \cdot 0{,}15405nm}{\left(\frac{0{,}162 \cdot \pi}{180}\right) \cdot \cos(14{,}212)} = 50{,}02_nm$$

$$D_2 = \frac{0{,}89 \cdot \lambda}{\beta_2 \cdot \cos\theta_2} = \frac{0{,}89 \cdot 0{,}15405nm}{\left(\frac{0{,}153 \cdot \pi}{180}\right) \cdot \cos(14{,}659)} = 53{,}07_nm$$

$$D_3 = \frac{0{,}89 \cdot \lambda}{\beta_3 \cdot \cos\theta_3} = \frac{0{,}89 \cdot 0{,}15405nm}{\left(\frac{0{,}159 \cdot \pi}{180}\right) \cdot \cos(14{,}967)} = 51{,}14_nm$$

2.1 SEM experiment

The object of study was investigated scanning electron microscope (SEM) series SIGMA from the company CORLE ZEISS in different detectors. Detector SECONDARY ELEKTRONS (SE) at WD = 3-20mm voltage not more than 5 kV on the gun The morphology of the sample. Detector Inlines also studied the morphology, but the permissions on a few orders of magnitude greater stress on the gun over 5kV and the working distance WD = 2,5 mm can be

observed object the size of 2 nm. On BACKSCATHERING DETEKTOR (BSD) to explore the phase difference across the sample at WD = 9-10mm, the voltage on the gun over 5kV. As you know research is conducted at high vacuum of 5 x 10^{-9} mbar.

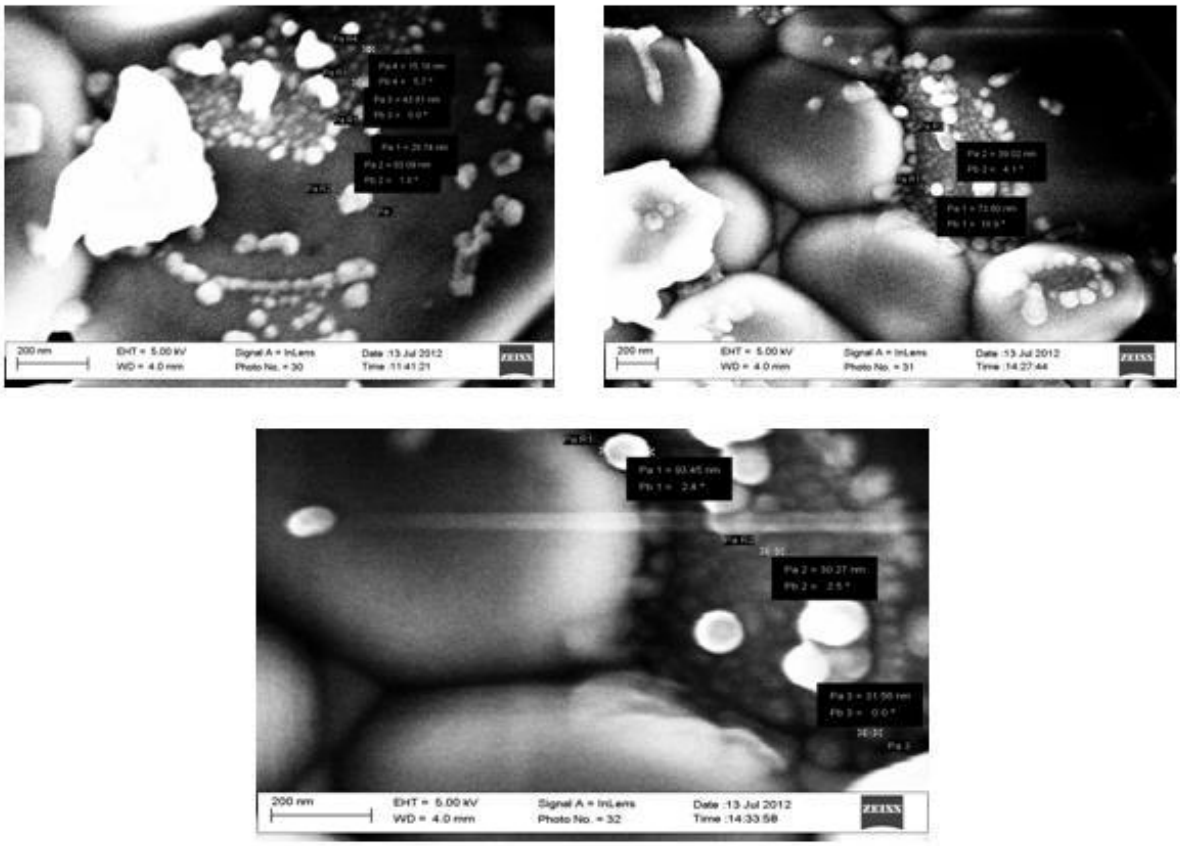

Fig. 12. SEM images of $SrAl_2O_4:Eu^{2+}$

Raman scattering spectra (fig.13) of $SrAl_2O_4$ and $SrAl_2O_4:Eu^{2+}$ were measured by Jobin-Yvon 1000 double monochromator with a S20 photomultiplier at room temperature.

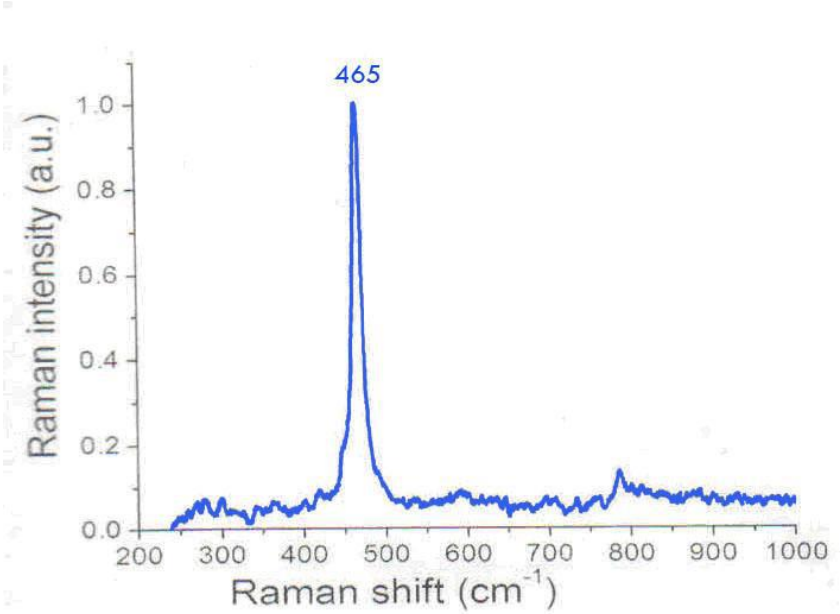

Fig. 13. Raman scattering spectra of $SrAl_2O_4$

3. DISSCUSION

Figure 7 presents the excitation and emission spectra of the samples $SrAl_2O_4:Eu^{2+}$ nanophosphor. This emission is ascribed to the dipol- allowed transtion from the lower $4f^65d(^7F)$ state to the $4f^7(\ ^8S_{2/7})$ fundamental state of the Eu^{2+} ions [8]. Although 4f electrons are not sensitive to lattice environment, the 5d electron may couple strongly to the lattice. Consequently, mixed states of $4f^65d$ will be split by the crystal field and will couple strongly to the lattice phonons, resulting in broad-band absorption and emission. In $SrAl_2O_4$ the Sr^{2+} ions are in the channels, which are formed by [AlO4] tetrahedra, and from chains in the structure. The Sr^{2+} ions are coordinated by nine oxygen ions, one site more regularly than the other. In $SrAl_2O_4$, the Sr^{2+} chains are along the ***a*** axis, and the chains in $SrAl_2O_4$ consist of two different Sr^{2+} sites. These chains are not perfectly linear. The distance between two successive Sr^{2+} ions is alternately 3.9 and 4.6A°. However, the distances between the Sr^{2+} ion and it is neighboring oxygen ions are different for the two Sr^{2+} sites. Looking along the ***a*** axis, the oxygen ions are rather close to one Sr^{2+} site, whereas the oxygen ions are at a much large distance from the other Sr^{2+} site. Thus, on the former Sr^{2+} site, no preferential orientation of a d orbital is possible due to the fact that the negative charge is a large distance. In general when the grain size reaches nanometer scale, the 5d energy level in rare earth ions varies with the change of the energy gap in host materials. As is well known, the luminescent spectra of lanthanide ions in crystals arise mainly from two types of electronic transitions: $4f \rightarrow 4f$ and $4f \rightarrow 5d$ transition. The former generally shows sharp line emission while the latter have a broad band character, and the crystalline environment has greater effect on interconfigurational transitions of rare earth than on intraconfigurational transitions within the shielded 4f. This is because the excited states such as 5d are not shielded from the surrounding electronic shell, and the 5d electron has a strong interaction with the neighboring anion ligands in the compound. In addition, the 5d energy level has close relation to the conduction band of the compound. When the grain size becomes small, the band gap may become wide or narrow, and then the 5d energy level also changes correspondingly. The change 5d energy level is related to the following factors: the energy centroid of the 5d orbit, crystal field splitting, Coulomb interaction between 4f and 5d electrons, spin-orbit interaction of 4f electron and spin-orbit interaction of 5d electron. Therefore it is interesting to study the Eu^{2+} luminescence in $SrAl_2O_4$ nano-size compound, in order to get a better understanding of the influence of the surroundings in the lattice on the Eu^{2+} luminescence.

The excitation spectrum of $SrAl_2O_4:Eu^{2+}$ at 300 K for the emission at 518 nm is presented in Fig. 9. The Stokes shift ΔS can be evaluated from excitation and emission spectra by using an almost mirror-image relationship. We have to consider the maxima of the excitation and the emission spectra corresponding to the lowest excited level. We have used the mirror-image relationship where the maximum of the emission band is calculated to obtain the same mirror shape for the higher energy edge of the emission band and the lower energy edge of the excitation band . The obtained parameters is: Stokes shift – 6205 cm^{-1}, FWHM-3056cm^{-1}, mean phonon energy-365cm^{-1}, Huang-Rhys factor *S* -9. This value $S = 9$ corresponds to ***strong*** electron phonon coupling regime. [9, 10]

Electronic property is fundamentally critical for the luminescent properties of solids. The electronic structure of host lattice could give rise to the fundamental absorption of excitation energy which may then be transferred to the luminescent centers resulting in effective luminescence. Furthermore, lattice vibration can also severely affect the luminescent quantum efficiency through the nonradiative transitions of multiphonon orbit-lattice relaxation of excited states in rare-earth ions doped crystals. Raman scattering spectra (fig.13) of $SrAl_2O_4$ and $SrAl_2O_4:Eu^{2+}$ were measured by Jobin-Yvon 1000 double monochromator with a S20 photomultiplier at room temperature. The 514 nm line of Kr spectra Physics laser was used as excitation source. One intense vibration line dominates the spectra respectively for $SrAl_2O_4$ at 465sm^{-1}.

CONCLUSION

The $SrAl_2O_4:Eu^{2+}$ nanoparticle phosphor could be obtain by combustion method . We obtain X-ray diffraction analysis of green, yellow and red emitting parts of $SrAl_2O_4$ precursor and saw that all the three parts were characterized as pure $SrAl_2O_4$. We obtain emission and excitation spectra of $SrAl_2O_4$ before and after sintering and saw that remaining Eu^{3+} transitions on the emission spectrum of $SrAl_2O_4$ completely disappears after increasing the sintering time of three hours. As a consequence, PCS requires highly diluted suspensions in order to avoid multiple scattering. We have evaluated the Stokes shift (6205 cm^{-1}) and we assume that theSrAl2O4:Eu^{2+} compound has a wider bandgap material and a weaker thermal quenching effect is obtained. The Huang-Rhys parameters S and the phonon energy were determined. This value S = 9 corresponds to strong electron phonon coupling regime.

Acknowledgments

The autors would like to express their sincere thanks to Dr. Rasim Jabbarov for scientific support.

[1] *D.A. Steigerwald, J.C. Bhat , D. Collins, R.M. Fletcher, M.O. Holcomb, M.J. Ludowise, P.S. Martin, and S.L. Rudaz,* Illumination with solid state lighting technology, IEEE, J. Sel. Top. Quantum Electron., 8, 310. (2002)

[2] *K.C. Mishra, M. Raukas, G. Marking, P. Chen, and P. Boolchand.* Investigation of fluorescence degradation mechanism of hydrated $BaMgAl_{10}O_{17}:Eu^{2+}$ Phosphor, J. Electrochem. Soc., 152, H183. (2005).

[3] *J.Y. Tsao*. Light Emitting Diode (LEDs) for General Illumination, 81, Optoelectronics Industry Development Association, Washingtons, D.C. (2002).

[4] *R.S.Meltzer, S.P. Feofilov, R. Tissue, and H.B. Yuan.* Dependence of fluorescence lifetimes of $Y_2O_3:Eu^{3+}$ nanoparticles on the surrounding medium, Phys. Rev. B., 60, R14012. (1999).

[5] *D.D. Jia, Y. Wang, X. Guo, K. Li, K. Zou and Jia,* WSynthesize and Characterize YAG:Ce^{3+} LED Nanophosphor, J. Electrochem. Soc., 154, J1. (2006b).

[6] *T. Ye, Z. Guiwen, Z. Weiping and X. Shangda,* Combustion synthesis and photoluminescence of nanocrystalline Y_2O_3:Eu phosphors, Mater. Res. Bull., 32, 501. (1997).

[7] *R.B. Jabbarov, S.H. Abdullayeva, N.N. Musayeva, C.A. Sultanov, S. Ozcelik.* Phosphor converted white LED street lamp. LED &LED lighting conference, 27-30 September-2012, Turkey, Istanbul, p. 31.

[8] *D.D. Jia,* Sr4Al14O25:Eu2+ nanophosphor synthesized with salted sol-gel method, Electrochem. Solid State Lett., 9, H93. (2006).

[9] *R. Jabbarov, N. Musayeva, F. Scholz, T. Wunderer, A.N. Turkin, S.S. Shirokov, and A.E. Yunovic.* Preparation and optical properties of Eu $^{2+}$ doped CaGa $_2S_4$ -GaS composite bicolor phosphor for white LED . Phys. Status Solidi A 206, No. 2, 287-292(2009).

[10] *C. Barthou, R.B. Jabbarov, P. Benalloul, C. Chartier, N.N. Musayeva, B.G. Tagiev, and O.B. Tagiev.* Radiative Properties of the Blue BaAl $_2$ S_4 : Eu $^{2+}$ Phosphor. Journal of The Electrochemical Society, 153(3) G 253-G258 (2006).

Received: 12.11.2012

ISSN 1028-8546

2012, Vol. XVIII, 4
Section: En

CONTENTS

1. Effects of randomness on the critical temperature in quasi-two-dimensional organic superconductors 3
E. Nakhmedov, O. Alekperov and S. Mammadova
2. Nonequilibrium electronic processes in single crystals GaS activated by rare-earth elements (REE) 8
B.G. Tagiyev, O.B. Tagiyev, S.A. Abushov, G.U. Eyubov
3. Effect of desmosterol on DPPC model membrane: an FTIR study 19
Ipek Sahin, Cisem Altunayar and Nadide Kazanci
4. Deposition of al-doped ZnO films by dc magnetron sputtering: effects of damp exposure and annealing on their properties 26
E.P. Zaretskaya, I.A. Victorov, O.V. Goncharova, T. R. Leonova, M. Gartner, N.N. Mursakulov, N.N. Abdulzade, Ch.E. Sabzaliyeva
5. The thermal expansion coefficient determination for magnetic semiconductor of $CuFeSe_2$ crystals by high temperature X-ray diffraction 31
G.G. Guseinov, Y.I. Aliyev, S.K. Orudjov, A.S. Amirov, B.A. Tahirov
6. Temperature dependence of barrier heights of Au/p-GaAs Schottky structures 35
Ahmet Asimov, Kemal Akay, Elchin Huseynov
7. The lattice long-wave oscillations of GeS nanocrystals 40
F.M. Hashimzade, D.A. Huseynova
8. Influence of hydrostatic pressure on elastic wave propagation in layered compound GaS
G.S. Orudzhev, E.K. Kasumova 43
9. Preparation and optical properties of $SrAl_2O_4:Eu^{2+}$ nanophosphor
S.Mammadova, H. Streit, T. Orucov, Ch. Sultanov 46